Synthesis of Novel TiN-based Hard Films by Thermal CVD for Metal Cutting Applications

Anongsack PASEUTH

Graduate School of Chemical Sciences and Engineering

Hokkaido University

北海道大学大学院　総合化学院

2018

Contents

Chapter 1. Introduction

1.1. Market trend and technical issues in the cutting tools industry

Cutting operations are one of the most popular methods for the mass-production of high-precision and low-cost machine parts. The production cost is considerably affected by the performance of the cutting tool material [1]. Typically, the cutting tool is exposed to abnormally high temperatures (~1000°C) and high pressures (~2 GPa) during the metal cutting operation [2]. Therefore, it is necessary for cutting tools to possess good properties, such as high hot hardness, high chemical stability and considerable toughness, in order to suppress wear and mechanical fatigue.

The history of cutting tool development is influence by the increasing demand for higher-speed and higher-efficiency cutting. Fig. 1.1 displays the representative modern tool materials, included high-speed steel, cemented carbide, ceramics, cermet, coated cemented carbide, cubic boron nitride (CBN), and diamond sintered bodies, which have been developed and commercially available for the metal cutting industry [3].

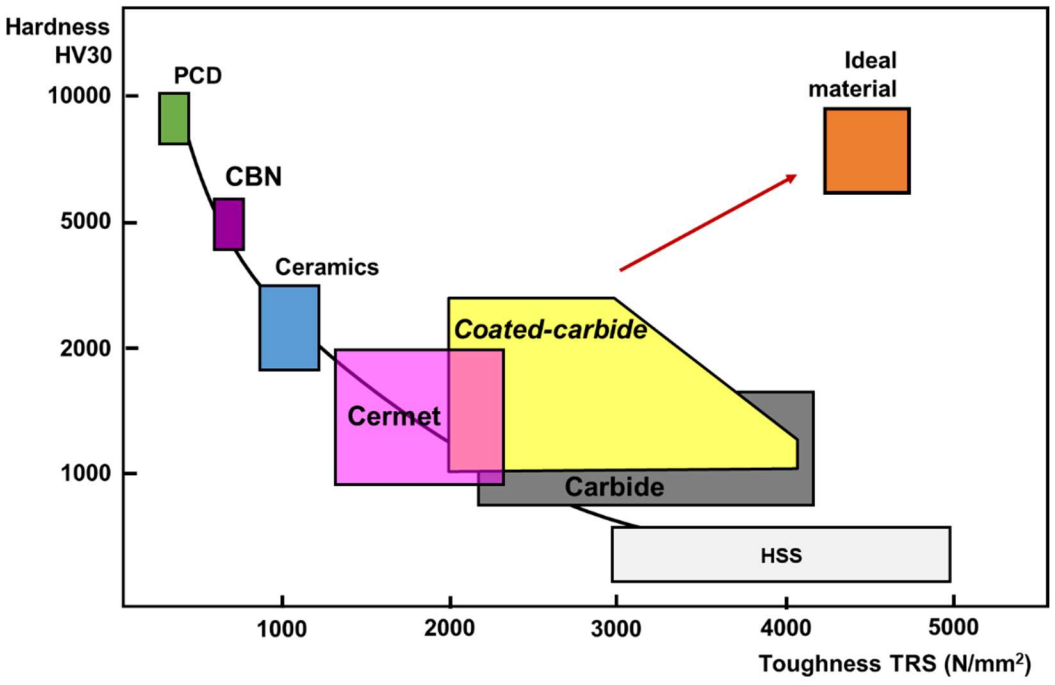

Fig. 1.1 Schematic diagram of the hardness and toughness relation for tool materials [3]

Among these tool materials, coated cemented carbide inserts occupied ca. 52% of the share [4] and are widely applied in metal cutting because of the desirable balance between hardness and toughness; this material has the benefit of being economically manufactured into complicated shapes using the powder metallurgical technique.

Fig. 1.2 shows the products ratio and number of shipments trend for non-coated cemented carbide, coated cemented carbide, cermet, and ceramics cutting inserts in the domestic market of Japan from 1965 to 2016 [5]. Recently, the share of coated cemented carbide inserts increased and accounts for more than 70% of the overall types of insert production, rendering it an indispensable industrial material.

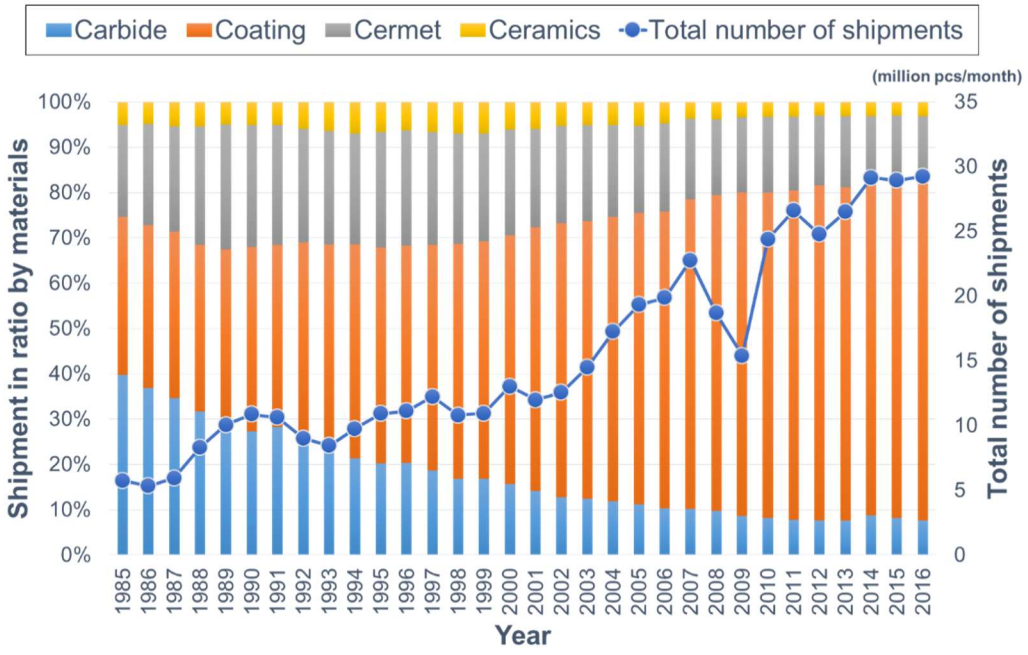

Fig. 1.2 Change in ratio and shipment amount of cutting insert materials in Japan [5]

The reason for the crucial increase in the amounts of coated cemented carbide in manufacturing is the high wear resistance imparted by hard ceramic coatings and the high impact resistance imparted by cemented carbide substrates. However, since there is a paradigm shift in the global market, the development of higher-performance cutting tools is strongly in demand by the industry.

The paradigm shift in the global market could be described as the result of the improved economies in developing countries, which have emerged as competitors in manufacturing

with the increase in the demand for higher productivity and lower production costs in developed countries [6]. Moreover, the increase in demand for lower environmental impact, lower energy consumption, and resource conservation imposes the requirement of further enhancement of the performance of state-of-the-art coated tools used in the metal cutting industry [7]. The technical issues for developing higher-performance tools could be addressed due to the following three major trends.

The first issue is the improvement of tool performance to adapt to the hard-to-cut materials. In considering the reduction of CO_2 emissions, there is increasing demand for the use of lightweight and high-strength materials in the automotive and aircraft industries, which leads to low-fuel consumption and a higher power engine [8]. A typical example is the usage of high-strength materials, such as high alloyed steel, ductile cast iron, super alloys, carbon fibre reinforced ceramics, and metal matrix composites. These materials not only demonstrate good hardness and strength properties at high temperatures, but also have low thermal conductivity, which results in the increase in cutting temperature but intensively decreases of tool's life. The development of new cutting tools capable of a longer service life for machining difficult-to-cut materials, are ardently required.

The second issue is the development of higher-performance tools to promote a dry higher cutting speed. An increase in cutting speed by 20% could result in a reduction of production costs by 15% per machined item [4]. Furthermore, dry cutting without the use of cutting oil, not only results in a reduction of energy consumption of the circulating pump, but also leads to an improvement in the working environment [9]. However, an increase in cutting speed and/or dry cutting results in the increase in cutting temperature, which shortens the tool's life. Thus, the development of new tools with excellent lubricity and heat resistance is in high demand.

The third issue is the manufacturer's responsibility to conserve and effectively use Tungsten (W). W is one of the rare metals which are used as a base material to produce the cemented carbide substrate in the cutting tool industry. Fig.1.3 indicates that approximately 60% of W resources and over 80% of its production is localised in China [10].

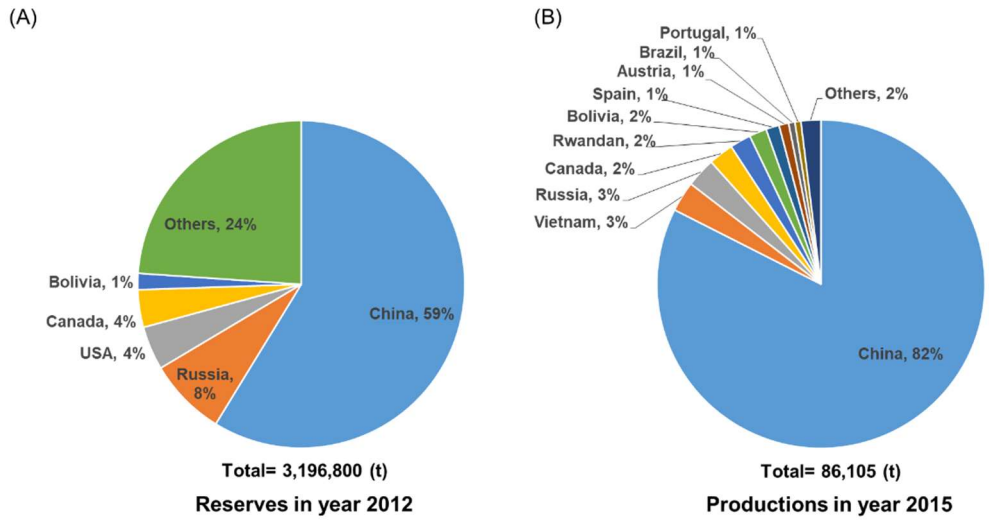

Fig. 1.3 Estimated reserves in the year 2012 of Tungsten Ore (A) and production amounts of Ammonium Paratungstate (APT) in the year 2015 (B) [10]

The market price of W precursor (APT: Ammonium Paratungstate) between the years 1994 and 2017 is shown in Fig. 1.4 (Data Source: London Metal Bulletin). According to export restrictions by the Chinese government, the APT price increased to $464/MTU (Metric Ton Unit) in 2011, which was approximately ten times higher than the price in the year 2000; the continuously soaring price of APT is a major concern for the tool industry. Consequently, there are efforts to develop recycling technologies for the effective usage of cemented carbide inserts [11] and alternative materials development to replace the cemented carbide substrate [12]. Nevertheless, the basic composition of cemented carbide has not been changed in the 90 years since its invention. A cemented carbide substrate has excellent properties, causing it to be well suited for tool manufacturing. This material has many applications in several fields in comparison with other tool materials; development hurdles for alternative materials to cover cemented carbide are extremely high. Therefore, the top priority and practical technical solution is to develop a higher-performance coating which is capable of extending the service life of the cemented carbide tools.

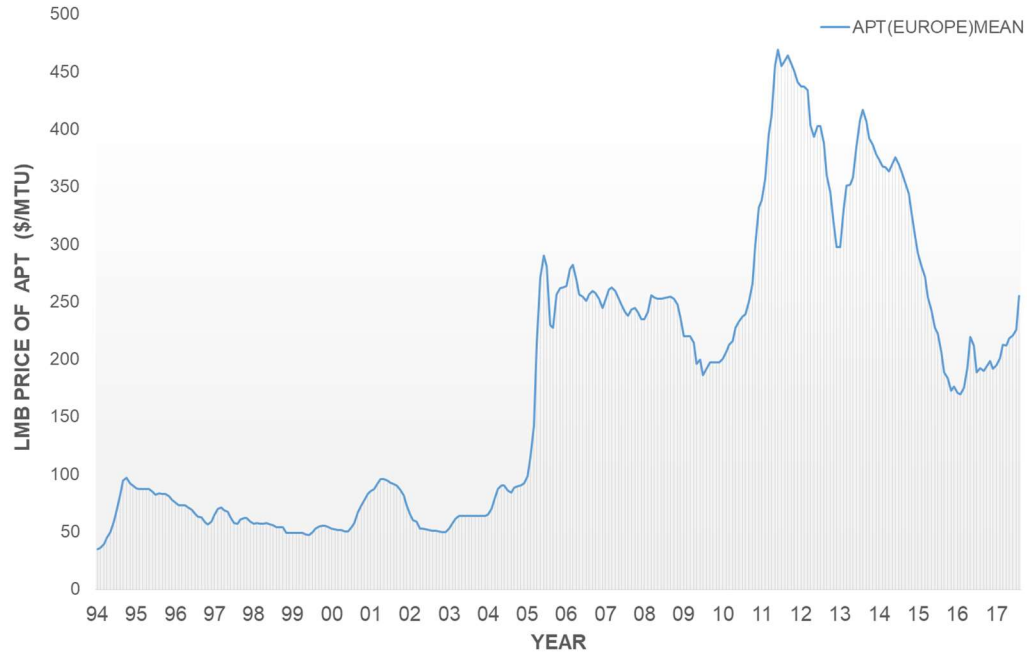

Fig. 1.4 Global market prices of APT (Ammonium Paratungstate) for 1994 through 2017 (Data source: Metal Bulletin)

According to change of the market trend in the cutting industry and owing to resource environment restrictions, as described above, further improvement in the performance of the coated tool is important and highly desired in order to maintain and increase manufacturing competitiveness.

In this work, a considerable improvement in tool life of coated cemented carbide inserts was achieved by introducing newly developed C-rich titanium carbon nitride (TiC_xN_{1-x}) and Al-rich titanium aluminium nitride ($Al_xTi_{1-x}N$) coatings prepared via the chemical vapour deposition (CVD) process [13–15]. The next section will provide a review of the development of hard coatings applied in the cutting tools industry, followed by the aim and outline of the study.

1.2. Coating technology and development trend

Fig. 1.5 represents schematic diagrams of (A) arc physical vapour deposition (PVD) and (B) a state-of-the-art CVD apparatus for mass-production of hard coatings in the tool industry.

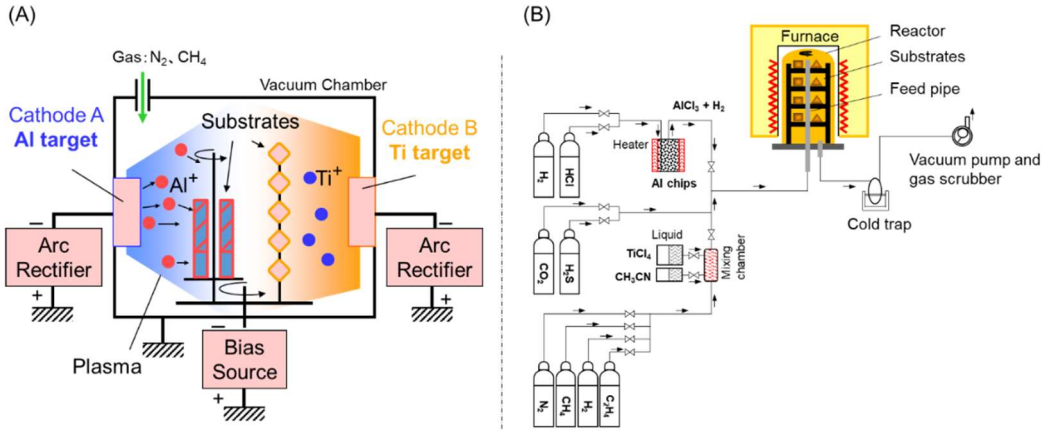

Fig. 1.5 Schematic diagram of (A) cathode arc evaporation PVD [16], and (B) CVD [17] apparatus in the cutting tool industry.

Arc-PVD is a representative production technique for wear-protective coating in addition to sputtering and electron beam evaporation as well as other ion plating methods. The arc-PVD process occurs in vacuum atmosphere (usually smaller than a few pascals) and a high electric current of 10–100 A is applied on the surface of the cathode (known as targets), generating a vacuum arc evaporation and ionization of target materials. The ejected ions are accelerated toward the substrate by inducing a negative bias potential on the substrate. The target materials used in arc-PVD are generally conduction materials such as Ti, Al or Cr and their alloys. The introduction of a chemically reactive gas (e.g. CH_4, and N_2) allows the deposition of thermodynamically non-equilibrium hard coatings including nitrides, such as TiN, Ti-Al-N, and Al-Cr-N, carbides, and those of multi-layer coatings. Hard coatings prepared by arc-PVD indicate a dense microstructure, which is well-adherent to the substrate in comparison with other ion plating techniques; they also have compressive residual stress which is beneficial for sharp edge inserts and interrupted cutting operations, such as milling or drilling [16].

However, CVD is a traditional chemical process used to produce high coating thickness, up to 30 μm, used for wear protection. The most important technical feature is that CVD is the only deposition technique, which economically produces high-quality and thick Al_2O_3 layers as thermal barrier coatings. A typical CVD technique used for the mass-production of hard coatings in the tools industry is low-pressure (LP) CVD. The energy require to activate

the chemical reactions is supplied by heaters located externally to the reactor chamber [17]. Hard nitride, carbide and oxide coatings prepared by CVD demonstrate high crystallinity and excellent adherence to substrates; could be deposited using volatile metal chlorides (e.g. $TiCl_4$, $AlCl_3$) with chemically reactive gas (e.g. N_2, CH_4, CO_2); and use H_2 as a carrier gas. Table 1 [18] summarizes the technical features of the deposited hard coatings via the PVD and CVD processes.

Table 1 Comparison between the CVD and PVD methods [18]

	CVD (Chemical vapor deposition)	PVD (Physical vapor deposition)
Principle	With reactive gas at a high Temperature (thermal CVD)	Ionization of the vaporized metal atoms (Arc, Sputter, Ion beam etc.)
Coverage	Excellent	Failure
Film materials	TiC,TiN,TiCN, Al_2O_3 (equilibrium)	TiN,TiCN,TiAlN,TiSiN,CrN (non-equilibrium)
Coating temperature	800℃ to 1000℃	400℃ to 600℃
Adhesion	Excellent	good
Stress	Tensile (Approx. 1 GPa)	Compressive (-2 to -5 GPa)
Transverse test*2 (fracturing property)	Failure	good
Typical film thickness	< 20 μm	< 5 μm
Applications	Turning insert (continuous cutting, insulation efficiency), Milling insert	Milling insert, Endmill, (interrupted cutting, sharp edge), Drill

Fig. 1.6 represents the evolution of the development of hard coatings using PVD and CVD techniques in the cutting tools industry [19]. During the early 1980s, the first industrially developed PVD hard coatings were based on binary carbides and nitrides of transition metals, such as TiC, TiN and CrN [20]. TiN has been one of the most used hard coatings for high-speed steel drills and turning tools due to its good mechanical, thermal and wear properties as well as the shiny gold colour. During the 1990s, the increasing demand of industry for higher machining speeds and feed rates, in combination with longer service of tool life, led to the development of the Ti-Al-N hard coating; this coating exhibits outstanding thermal stability up to 800°C and high hot hardness increased by the age hardening effect

[21–24]. Today, Ti-Al-N coatings have become the standard choice for many dry cutting applications. Efforts to improve the thermal and mechanical properties of metastable c-$Ti_{1-x}Al_xN$ coatings include increasing the Al content [25], doping with a fourth element such as Cr [26], Si [27], Zr [28], Ta [29], and Y [26, 30], and modulating the multilayer structure (e.g. TiN/AlN [31]). These advances are the latest topics in PVD hard coating development. Moreover, the introduction of new PVD process techniques, such as high power impulse magnetron sputtering could result in a smoother surface in comparison with conventional arc-PVD. Furthermore, as mentioned previously, there is a constantly increasing demand for high-speed and high-feed-rate cutting in industry leading to cutting temperatures exceeding 1000°C. Accordingly, development of oxide coatings (e.g. Al_2O_3 [32,33], Al-Cr-O [34,35]) via PVD has received increased attention. However, these oxide coatings are typically insulating which causes an unstable and discontinuous coating process, with a considerable low deposition rate. Further improvement in process techniques and deposition of thermally stable corundum type Al_2O_3 is a challenging topic for the future development of PVD hard coatings.

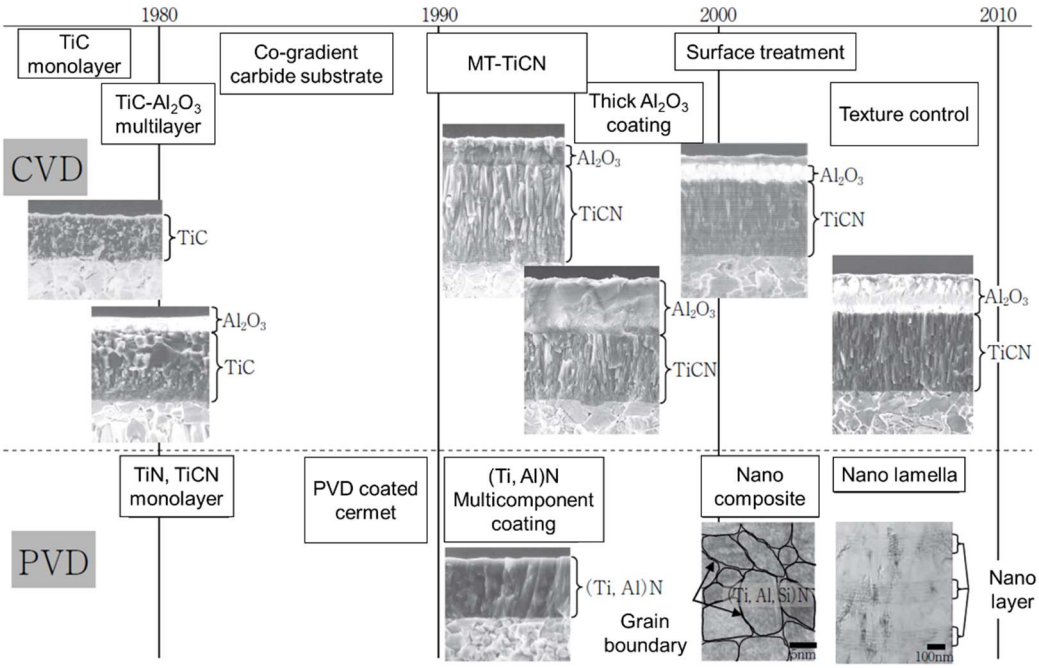

Fig. 1.6 Evolution of hard coatings for cutting tools [19]

In the CVD hard coating field, the first TiC coated cemented carbide inserts via CVD were introduced into the tool market in the year 1968/69 by Sandvik in Sweden and Krupp-Widia in Germany. TiC coated carbide inserts demonstrated a significant increase in tool life in the applied field of carbon steel turning [36]. However, the TiC coating had a decisive disadvantage for interrupted cutting and milling operations. TiC prepared by the CVD method is generally performed at 950 to 1100°C, using the $TiCl_4$-CH_4-H_2 gas system. The carbon source is supplied not only by CH_4 gas, but also by the diffusion of carbon from the carbide substrate. The chemical reactions involved in the deposition of TiC are summarized by Eq.(1.1) to Eq.(1.4) [17].

$$TiCl_4(g) + 2H_2(g) \rightarrow Ti(s) + 4HCl(g) \quad Eq.(1.1)$$

$$\mathrm{Ti}(s) + CH_4(g) \rightarrow TiC(s) + 2H_2(g) \quad Eq.(1.2)$$

$$2\mathrm{Ti}(s) + 3WC(s) + 3Co(s) \rightarrow 2TiC(s) + Co_3W_3C(s) \quad Eq.(1.3)$$

$$5\mathrm{Ti}(s) + 6WC(s) + 6Co(s) \rightarrow 5TiC(s) + Co_6W_6C(s) \quad Eq.(1.4)$$

According to Eq.(1.3) and Eq.(1.4), the brittle η phases (Co_3W_3C and Co_6W_6C) formed between the interface of the TiC coating and cemented carbide substrate; a particularly thicker η phase formed at the cutting edge where the decarburization occurred faster due to a higher specific surface area.

During the 1970s, efforts to decrease the brittle η phases and improve the thermal properties of a CVD coated insert involved a monolayer TiC coating into TiCN, TiN, and those multilayer structures coupled with Al_2O_3 coatings on top [37–39]. Moreover, during the 1980s, a remarkable improvement in interrupted cutting and milling performance of CVD coated tool inserts was achieved by introducing moderate temperature (MT) CVD coating technology [40]. Bonetti et al. [41,42] introduced acetonitrile (CH_3CN) as a carbon and nitrogen source, replacing CH_4 and N_2 gas, which enabled the deposition of TiCN coatings from 800°C. The CVD reactions for formation of high-temperature (HT) TiCN coatings by the $TiCl_4$-CH_4-N_2-H_2 gas system, and moderate temperature (MT) TiCN coatings by the $TiCl_4$-CH_3CN-H_2 gas system can be presented as follows [43]:

$$TiCl_4(g) + xCH_4(g) + \frac{(1-x)}{2}N_2(g) + 2(1-x)H_2(g) \rightarrow TiC_xN_{1-x}(s) + 4HCl(g) \quad Eq.(1.5)$$

$$2TiCl_4(g) + CH_3CN(g) + 4.5H_2(g) \rightarrow 2TiC_{0.5}N_{0.5}(s) + CH_4(g) + 8HCl(g) \; Eq.(1.6).$$

The MT-CVD process quickly spread to become a standard CVD coating process in the tool industry. The advantage of the MT-CVD coating is contributed by not only the strong reduction of the brittle η phase and lower thermal stress (tensile stress) caused by a difference between the thermal coefficient of the ceramics coatings and cemented carbide, but also by the formation of a fine columnar grain structure resulting in an increase in wear and fracture resistance. Fig. 1.7 (A) and (B) represent the scanning electron microscopy (SEM) cross section of HT-TiCN and MT-TiCN coatings, respectively.

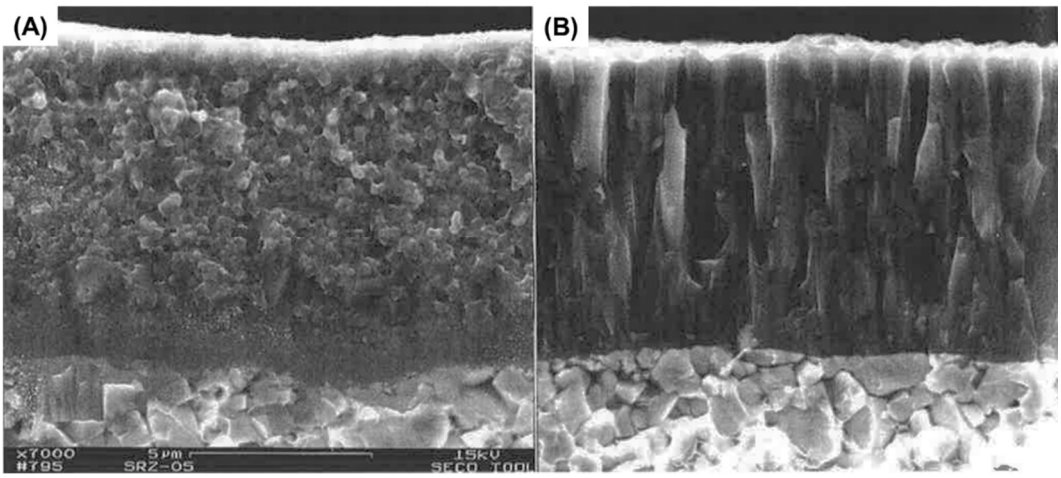

Fig. 1.7 Cross section SEM micrographs of (A) HT-TiCN and (B) MT-TiCN coatings on a cemented carbide substrate [44]

Furthermore, the introduction of H_2S gas as a catalyst during Al_2O_3 deposition is one of the most important innovations, which significantly increases the deposition rate and thickness homogeneity of CVD Al_2O_3 coatings [45].

Today, CVD coatings are estimated to account for ca. 30% of the share in the world market of hard coating materials[4]. Until now, there have been attempts to improve the cutting performance of a CVD coating by increasing adhesion [46] (e.g. TiCN/Al_2O_3), and enhancing performance of the Al_2O_3 top coating by controlling crystal orientation [47]. Fig. 1.8 shows the effect of Al_2O_3 crystal orientation on tool life using a tuning operation of (A) steel

(AISI:1042) and (B) cast iron (AISI:A48-45A). In applications involving relatively high temperatures and shear stresses as in turning of steels, an Al_2O_3 top-coating with (0001) preferred orientation could increase tool life by two-fold in comparison with the random orientation. However, in applications involving high abrasive as in tuning of cast iron, the tool life increment is limited; thus, the development of a new hard coating is crucial to high-speed and dry cutting applications.

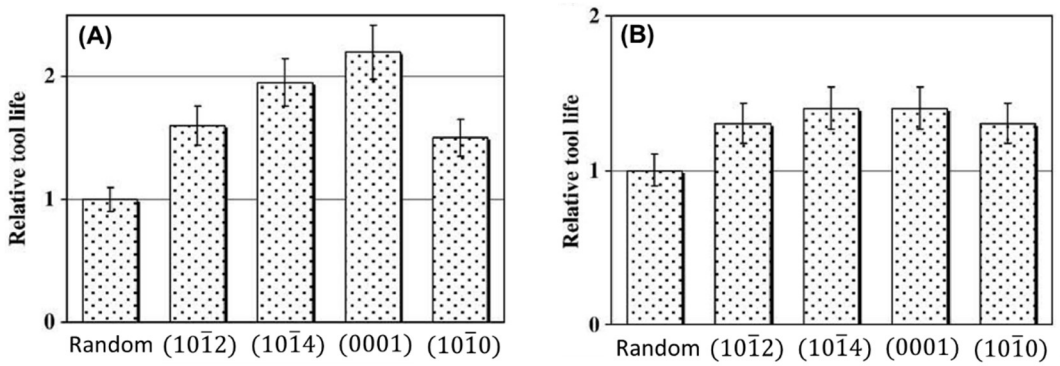

Fig.1.8 Mean tool lives for various Al_2O_3 top coatings with different preferred crystalline orientation when turning: (A) steel (AISI:1042) at 270 m/min and (B) cast iron (AISI:A48-45A) at 300 m/min [47]

Therefore, development of a high-performance coating has received increased attention. Considerable effort has been devoted to the improvement in the cutting performance of MT-TiCN coatings by adding $ZrCl_4$ [48], BCl_3 [49] and CO [50,51] to refine the structure, increase hardness, and improve the surface morphology. However, the improvement in the cutting performance displayed in these basic researches is limited, and most have not been able to attain practical use.

1.3. Aim of the study

Referring to the mentioned technical background, further enhancement of the performance of coated tools is required to meet the demands for lower cost, lower environmental impact and resource conservation. In the case of high-speed and dry cutting applications, CVD hard coatings have a big advantage to those of PVD. The CVD process is to this day the

only deposition technique which could economically produce high-quality coatings of Al_2O_3. Nevertheless, since the invention of MT-TiCN hard coating in the 1980s, a new CVD hard coating, which could be mass-produced and applied for wider applications, has not yet appeared and the tool industry is demanding its development now.

In this dissertation, new hard coatings with superior wear resistance, increased toughness and high thermal stability, capable in industrial scaled thermal CVD, have been discussed and their practical applications for metal cutting industries have been explored. The CVD process, including new gas precursors, such as C_2H_4 and NH_3, has introduced and adapted to prepare Titanium and/or Titanium aluminium based nitride and carbonitride coatings. The effect of deposition parameters on chemical compositions, microstructures and physical properties will be clarified and a wide range of cutting applications has been investigated. Finally, the dissertation could help establish guidelines for developing high-performance tools which could be applied for dry cutting and higher cutting speeds.

1.4. Outline of the study

This dissertation consists of the following seven chapters.

Chapter 1 describes the background and purpose of the study.

Chapter 2 describes the investigation of the effect of the *x* value in MT-TiC_xN_{1-x} coatings on their microstructure, mechanical properties, and cutting performance. Deposition of MT-TiC_xN_{1-x} coatings with different *x* values was conducted using a $TiCl_4$–CH_3CN–C_2H_4–H_2 gas precursor system, allowing the increase in the *x* value at 840°C by varying the C_2H_4/CH_3CN molar ratio. Changes in the microstructure, crystallite size, indentation hardness, and adhesion of the MT-TiC_xN_{1-x} coatings as a function of the x value were investigated.

In chapter 3, the optimised *x* (*x*=0.63) value in MT-TiC_xN_{1-x} fabricated via CVD using the $TiCl_4$–CH_3CN–C_2H_4–H_2 precursor system was conducted in order to increase the adhesion strength between the modified MT-TiC_xN_{1-x} coating and carbide substrate. The detailed report on the grain structure, micro-orientation, and mechanical properties including the friction coefficients of the modified MT-$TiC_{0.63}N_{0.37}$ coating, are compared with those of a conventional MT-TiC_xN_{1-x} (x=0.45) coating. In addition, the cutting performance obtained by longitudinal continuous turning of carbon, alloyed and stainless steels, and by intermittent

turning tests with four-groove alloyed steel on as-deposited modified and conventional MT-TiC_xN_{1-x} coatings was investigated.

In chapter 4, synthesis of Al-rich cubic (c-) AlTiN coatings via LP-CVD in an industrial plant, using an $AlCl_3$–$TiCl_4$–NH_3–Ar–H_2 precursor system were conducted in order to develop a higher-performance hard coating, promote higher cutting speeds and dry cutting applications. The c-$Al_xTi_{1-x}N$ coatings with (100) and (111) preferred orientations and average *x* values of 0.82 and 0.73, respectively, were deposited. The Al-rich c-$Al_xTi_{1-x}N$ coatings comprised of c-Al(Ti)N/c-Ti(Al)N nano-lamellae had average lamellar periods varying from 4.5 to 7.7 nm. High-resolution transmission electron microscopy revealed that the c-Al(Ti)N/c-Ti(Al)N nano-lamellae were modulated along the <100> direction. The hardness measurements indicated high hardness and varied from 33 to 36 GPa, depending on the (100) or (111) preferred orientation. In situ high-temperature X-ray diffraction patterns elementally suggested high thermal stability with a maximum of 1000°C.

In chapter 5, the effects of post-annealing temperatures on the crystal structure, microstructure, hardness and thermal stability of Al-rich c-$Al_xTi_{1-x}N$ (*x*=0.7, 0.8) were investigated and compared with an arc PVD $Al_xTi_{1-x}N$ (*x*=0.6) coating. The Al-rich c-$Al_xTi_{1-x}N$ (*x*=0.7, 0.8), which comprised the self-organised and coherent c-Al(Ti)N/c-Ti(Al)N nano-lamellae, displayed good thermal stability upon heating at 900°C for 1 h; this was an improvement on the phase stability of the single-phase PVD $Al_xTi_{1-x}N$ (*x*=0.6) coating. Furthermore, the aging hardness was shifted up by 100°C for the CVD c-$Al_xTi_{1-x}N$ coatings compared with the PVD $Al_xTi_{1-x}N$ (*x*=0.6) coating. This good thermal stability of the Al-rich c-$Al_xTi_{1-x}N$ coatings prepared by the CVD process assures further enhancement in cutting tool performance for dry and high-speed cutting applications.

In chapter 6, the effect of annealing temperatures and times on phase stability and mechanical properties of CVD c-$Al_xTi_{1-x}N$ (*x*≈0.8) in comparison with PVD c-$Al_xTi_{1-x}N$ (*x*≈0.6) coatings were further investigated. The extinction of the metastable c-AlN phase in c-$Al_xTi_{1-x}N$ (*x*=0.8) was observed after annealing at 1200°C for 1 h, which is approximately 200°C higher than that of the c-$Al_xTi_{1-x}N$ (*x*=0.6) coating. The improved thermal stability and mechanical properties at elevated temperatures resulted in significant improvement in the cutting tool life by factor of 2 and 10 compared with state-of-the-art CVD- and PVD-coated

inserts, respectively.

Chapter 7 summarizes the findings and contributions of the high-performance coating obtained for higher speeds and dry cutting, to meet the strong industry demands for lower cost, lower environmental impact and resource conservation. Furthermore, some challenges and future prospects in the development of new CVD coatings will be outlined.

References in chapter 1

[1] H. Nakamura, J. Jpn. Soc. Mech. Eng. 84 (1981) 268–272.

[2] T. Sugita, K. Ueda,T. Inamura, Basic Theory of Metal Cutting, first ed., Kyoritsu Shuppan,Tokyo, 1984.

[3] L. Prakash, Fundamentals and General Applications of Hardmetals,in: V.K. Sarin, Comprehensive Hard Materials**,** Elsevier., Oxford, 2014, pp. 29–90.

[4] K. Bobzin, CIRP Ann. Manuf. Technol. 18 (2017) 1–9.

[5] Japan Cutting and Wear-resistance Tool Asociation, Production and shipping statistics of inserts. http://www.jta-tool.jp/pdf/new_seisansuii, 2016.

[6] M. Goto, J. Jpn. Soc. Grind. Eng. 56 (2012) 3–6.

[7] A. Kawana, J. Surf. Finish. Soc. Jpn. 58 (2007) 826–826.

[8] S. OkunO, A. Paseuth, Y. Okada, A. Sakamoto, SEI. Tech. Rev. 75 (2012) 8–12.

[9] F. Klocke, G. Eisenblätter, CIRP Ann. 46 (1997) 519–256.

[10] O. Tomoe, JOGMEC Report of metal materials. 44 (2014) 296–301.

[11]. T. Hayashi, F. Sato, K. Sasaya, A. Ikegaya, SEI. Tech. Rev. 82 (2016) 33–38.

[12] T. Ishida, H. Moriguchi, A. Ikegaya, SEI. Tech. Rev. 73 (2011) 52–56.

[13] A. Paseuth, H. Fukui, S. Okuno, H. Kanaoka, Y. Okada, Surf. Coat. Technol. 260 (2014) 139–147.

[14] A. Paseuth, H. Fukui, K. Yamagata, Surf. Coat. Technol. 291 (2016) 54–61.

[15] A. Paseuth, K. Yamagata, A. Miura, M. Higuchi, K. Tadanaga, J. Am. Ceram. Soc. 100 (2017) 343–353.

[16] K. Takahara, H. Fujii, Kobe Steel Tech. Rep. 50 (2000) 53–57.

[17] Y. Doi, J. Jpn. Soc. Powder. Metall. 30 (1983) 297–305.

[18] H. Fukui, SEI. Tech. Rev. 82 (2016) 39–45.

[19] A. Osada, J. Jpn. Soc. Precis. Eng. 76 (2010) 1315–1318.

[20] U. Schleinkofer, C. Czettl, C. Michotte, Coating Applications for Cutting Tools, in: V. K. Sarin, Comprehensive Hard Materials**,** Elsevier, Oxford, 2014, pp. 453–469.

[21] W. D. Münz, J. Vac. Sci. Technol. A 4 (1986) 2717–2725.

[22] O. Knotek, T. Leyendecker, J. Solid State Chem. 70 (1987) 318–322.

[23] T. Leyendecker, O. Lemmer, S. Esser, J. Ebberink, Surf. Coat. Technol. 48 (1991)

175–178.

[24] P. H. Mayrhofer, A. Hörling, L. Karlsson, J. Sjölén, T. Larsson, C. Mitterer,L. Hultman, Appl. Phys. Lett. 83 (2003) 2049–2051.

[25] K. Yamamoto, J.High. Temp. Soc. 33 (2007) 84–89.

[26] W.D. Munz, I. Smith, L. Donohue, Proc. in Society of Vacuum Coaters 40th Annual Technical Conference. November 7, Albuquerque, NM, USA (1997) pp. 89–93.

[27] S. Vepřek, M. Haussmann, S. Reiprich, L. Shizhi, J. Dian, Surf. Coat. Technol. 86–87 (1996) 394–401.

[28] B. Yang, L. Chen, Y. X. Xu, Y. B. Peng, J. C. Fen, Y. Du, M. J. Wu, Int. J. Refract. Met. Hard Mater. 38 (2013) 81–86.

[29] R. Rachbauer, D. Holec, P. H. Mayrhofer, Surf. Coat. Technol. 211 (2012) 98–103.

[30] H. Riedl, D. Holec, R. Rachbauer, P. Polcik, R. Hollerweger, J. Paulitsch, P. H. Mayrhofer, Surf. Coat. Technol. 235 (2013) 174–180.

[31] M. Setoyama, M. Irie, H. Ohara, M. Tsujioka, Y. Takeda, T. Nomura, N. Kitagawa, Thin Solid Films 341 (1999) 126–131.

[32] M. Åstrand, T. I. Selinder, F. Fietzke, H. Klostermann, Surf. Coat. Technol. 188–189 (2004) 186-192.

[33] K. Bobzin, N. Bagcivan, M. Ewering, R. H. Brugnara, S. Basturk, Surf. Coat. Technol. 257 (2014) 58–62.

[34] J. Ramm, M. Ante, T. Bachmann, B. Widrig, H. Brändle, M. Döbeli, Surf. Coat. Technol. 202 (2007) 876-883.

[35] J. Ramm, M. Ante, H. Brändle, A. Neels, A. Dommann, M. Döbeli, Adv. Eng. Mater. 9 (2007) 604–608.

[36] H. M. Ortner, P. Ettmayer, H. Kolaska, Int. J. Refract. Met. Hard Mater. 44 (2014) 148–159.

[37] R. Funk, B. Lux, H. Schachner, C. Triquet, US Patent No. US3836392 (1974).

[38] T. E. Hale, US Patent No. US4018631 (1977).

[39] J. Lindstrom, B. Jonsson, F. Ohlsson, US Patent No. US3837896 (1974).

[40] E. Kübel, Surf. Coat. Technol. 49 (1991) 268–274.

[41] M. Bonetti-Lang, R. Bonetti, H. E. Hintermann, D. Lormann, Prooc. 8th Int. Conf. on

Chemical Vapour Deposition, Pennington, NJ, USA (1981) pp. 606–616.

[42] R. S. Bonetti, H. Wiprächtiger, E. Mohn, Met. Powder. Rep. 45 (1990) 837–840.

[43] J. Garcia, R. Pitonak, R. Weissenbacher, A. Köpf, Surf. Coat. Technol. 205 (2010) 2322–2327.

[44] S. Ruppi, Proc. 13rd European Conference on Chemical Vapour Deposition, J. Phys. IV France **11** (2001) Pr3-847–Pr3-859.

[45] U. K. Smith, J. N. Lindstrom, US Patent No. US4619866 (1986).

[46] J. Garcia, R. Pitonak, R. Weißenbacher, A. Köpf, F. Soldera, S. Suarez, F. Miguel, H. Pinto, A. Kostka,F. Mücklich, Adv. Eng. Mater. 12 (2010) 929–934.

[47] S. Ruppi, Surf. Coat. Technol. 202 (2008) 4275–4269.

[48] S. Kudapa, K. Narasimhan, P. Boppana, W. C. Russell, Surf. Coat. Technol. 120–121 (1999) 259–264.

[49] C. Czettl, C. Mitterer, M. Penoy, C. Michotte, M. Kathrein, Surf. Coat. Technol. 215 (2013) 127–132.

[50] S. Ruppi, A. Larsson, J. Vac. Sci. Technol., A 21(2003) 66–75.

[51] C. Czettl, C. Mitterer, U. Mühle, D. Rafaja, S. Puchner, H. Hutter, M. Penoy, C. Michotte, M. Kathrein, Surf. Coat. Technol. 206 (2011) 1691–1697.

Chapter 2. Microstructure, mechanical properties, and cutting performance of TiC_xN_{1-x} coatings with various *x* values fabricated by moderate temperature chemical vapour deposition

2.1. Introduction

Coated tools used for metal cutting require both high abrasive wear resistance and chemical stability at high temperatures to meet the demands of this application. Titanium carbonitride (TiCN) produced by moderate temperature (700–900°C) chemical vapour deposition (MT-CVD) using a $TiCl_4$–CH_3CN–N_2–H_2 precursor system with alumina (Al_2O_3) as a top layer (MT–TiCN–Al_2O_3) [1–6] was developed for cemented carbide tools because of its high wear resistance and toughness. However, recently, in the machining field, reductions in energy consumption and machining costs have been demanded, leading to higher cutting speeds, which shortens tool life. Thus, coatings with higher wear resistance are strongly required by the industry, and of TiCN-coated tools [7–12]. TiC_xN_{1-x} coatings with an increased carbon content *x* are expected to improve mechanical properties such as hardness [13, 14], Young's modulus [14], and friction coefficient [15]. Recently, Jun Watanabe et al. [16] reported a method for increasing the *x* value in TiC_xN_{1-x} coatings up to 0.9 and improving their wear resistance using a CVD process with a mixture of reactive hydrocarbon gases and CH_3CN gas. However, increasing the value of *x* in TiC_xN_{1-x} coatings results in a loss of adhesion to the substrate [17]. Therefore, a comprehensive study on the controlled adjustment of the microstructure and chemical composition of hard coatings is required to improve their cutting performance.

The aim of this study was to investigate the effect of the *x* value in TiC_xN_{1-x} coatings for carbide tools on their microstructure, mechanical properties, and cutting performance. Deposition of TiC_xN_{1-x} coatings with different *x* values was achieved by feeding C_2H_4 gas into a $TiCl_4$–CH_3CN–H_2 precursor system using the MT-CVD process with varying C_2H_4/CH_3CN molar ratio. Changes in the microstructure, crystallite size, indentation hardness, and adhesion of the coatings as a function of the *x* value were investigated. Finally, a longitude turning operation test using ductile cast iron (AISI: 100-70-03) was performed

using TiC_xN_{1-x} (10 μm)/Al_2O_3 (5 μm)-coated carbide tools for which the *x* value ranged from 0.59 to 0.74.

2.2. Experimental procedures

2.2.1 Coating

The deposition of TiC_xN_{1-x} coatings with various *x* values was performed in a commercially available hot-wall, low-pressure CVD system (Reactor scale: 1450 mm height × 450 mm diameter; full-loaded capacity = 10.000 pieces of CNMG120408 inserts). The depositions were achieved using a $TiCl_4$–CH_3CN–C_2H_4–H_2 precursor system, and the parameters used for production of the investigated coatings are listed in Table 2.1. First, TiC_xN_{1-x} coatings with various *x* values were deposited for the purpose of physical property analysis. WC–5wt%Co substrate (Sumitomo Electric Hardmetal Corp., SNMA120408) with mirror polished surfaces were loaded in the center of the batch on one-half radius of the tray. A 0.3–0.5-μm-thick base layer was deposited, followed by a $TiC_{0.59}N_{0.41}$ 0.7–1.0-μm-thick bonding layer. An approximately 7-μm-thick TiC_xN_{1-x} coating was then deposited. The *x* value in the TiC_xN_{1-x} coating was controlled by changing the C_2H_4/CH_3CN molar ratio. The deposition temperature, pressure, and time were fixed at 840°C, 9 kPa, and 200 min, respectively. The deposition of each TiC_xN_{1-x} coating was repeated twice. Next, TiC_xN_{1-x} coatings with α-Al_2O_3 top layers were deposited on cemented carbide inserts (WC–5wt%Co substrate, CNMG120408-NGZ-type geometry, Sumitomo Electric Hardmetal Corp.) to evaluate the cutting performance of the TiC_xN_{1-x} coatings. The inserts were loaded in the same manner as described above. The thicknesses of the TiC_xN_{1-x} and α-Al_2O_3 coatings were 10 μm and 5 μm, respectively.

Table 2.1 Deposition parameters used for preparation of the investigated coatings

	TiC_xN_{1-x} layer	$TiC_{0.59}N_{0.41}$ bonding layer	TiN base layer	Al_2O_3 top layer
Temperature (°C)	840	840	860	1000
H_2 (vol%)	Balance	Balance	Balance	Balance
N_2 (vol%)	-	30.0	30.0	-
$TiCl_4$ (vol%)	3.0	2.0	1.0	-
CH_3CN (vol%)	0.42-0.33	0.5	-	-
C_2H_4 (vol%)	0.0-10.0	-	-	-
C_2H_4/CH_3CN molar ratio	0-30			
CO_2 (vol%)	-	-	-	4.5
H_2S (vol%)	-	-	-	0.2
$AlCl_3$ (vol%)	-	-	-	1.6
HCl (vol%)	-	-		3.5
Total gas flow (L/min)	80	75	60	50
Deposition time (min)	200	60	90	400
Pressure (kPa)	9.0	6.7	10	7.0

2.2.2 Coating characterization

The chemical composition, microstructure, hardness, and adhesion of the TiC_xN_{1-x} coatings were studied. The chemical compositions and bonding states of the TiC_xN_{1-x} coatings were investigated using X-ray photoelectron spectroscopy (XPS; PHI Quantera SXM spectrometer) using a monochromatic AlKα X-ray source. All the spectra were calibrated to the binding energy for the $Au4f_{7/2}$ and $Cu2p_{3/2}$ levels. The analyses were performed on top of the surface down to a depth of approximately 1 μm after sputtering Ar^+ ions with energy of 4 keV for 100 min. The chemical states of titanium (Ti2p) and carbon (C1s) for the deposited coatings were analyzed. Furthermore, the chemical compositions of the TiC_xN_{1-x} coatings at 20 locations in the depth profiles were evaluated, and the *x* values were determined as the average for the C/(C+N) atomic ratio. The lattice parameters for the TiC_xN_{1-x} coatings were investigated twice by X-ray diffraction (XRD; RIGAKU, Rint Ultima III and SmartLab) with CuKα radiation and a graphite monochromator. The crystallite sizes of the TiC_xN_{1-x} coatings were calculated from the (422) full width at half maximum (FWHM) reflections according to Scherrer's equation:

$$D_{(422)} = \frac{K\lambda}{B\ cos\theta} \quad Eq.(2.1)$$

where D(422) is the mean crystallite size along the (422) orientation, K (0.9) is the shape

factor, λ is the X-ray wavelength = 1.5405 Å for CuKα radiation, B is the FWHM value for the (422) reflection, and θ is the Bragg angle.

Microstructural evaluation of the coatings was performed using scanning electron microscopy (SEM) and optical microscopy observations. The surface and cross-sectional morphologies were observed via a scanning electron microscope (Hitachi High-Tech SU6600), whereas the coating thickness and homogeneity were evaluated using an optical microscope (Leica DMIRM) on mirror-polished and chemically etched (Murakami reagent) cross sections of the TiC_xN_{1-x} coatings. The hardness of the TiC_xN_{1-x} coatings was measured by an indentation technique (Elionix, ENT-1100a) with a Berkovich tip diamond indenter using a load of 0.5 N. The indentation hardness was measured at 10 locations on a mirror-polished cross section, and the average value was considered as the coating hardness. The coating adhesion was determined using a scratch test (CSM REVETEST). A Rockwell C diamond tip with a conical angle of 120° and a tip radius of 200 μm was used as a scratch indenter. The scratch test was conducted at a constant scratching speed of 10 mm/min and a loading rate of 100 N/min with a load from 0 N to 100 N. The critical load was measured three times, and the average value was determined to be the coating adhesion.

2.2.3. Cutting performance

The cutting performance of the TiC_xN_{1-x} coatings with different x values (x = 0.59 to 0.75) was evaluated by a longitudinal turning operation on ductile cast iron (AISI: 100-70-03, 300 mm in diameter and 1000mmin length) for up to 20 min. According to highly cohesive nature of work material, α-Al_2O_3 was deposited on the top of TiC_xN_{1-x} coatings to avoid an abnormal wear of cutting edge. The coatings consisted of a 10-μm-thick TiC_xN_{1-x} layer and 5-μm-thick α-Al_2O_3 layer with no preferred orientation and no additional surface treatment, and were deposited on carbide tools. The cutting performance of these coated tools was compared with that of a commercially available ISO K10-grade tool (Sumitomo Electric Hardmetal Corp. AC410K, $TiC_{0.59}N_{0.41}$(10 μm)/α-Al_2O_3(5 μm)-coated carbide insert, CNMG120408-NGZ). The cutting conditions are listed in Table 2.2. The wear morphology and the average width of the flank wear (Vb) were observed and measured using an optical microscope.

Table 2.2 Longitude turning condition of TiC_xN_{1-x}(10 µm) / Al_2O_3 (5 µm) with various x values on ductile cast iron

Cutting tools	Work material	Cutting speed	Feed rate	Depth of cut	Environment	Maximum cutting time
CNMG120408-NGZ	AISI:100-70-03	120 m/min	0.3 mm/rev	1.5 mm	Wet	20 min

2.3. Results

2.3.1. Microstructure analysis

XPS analysis of the TiC_xN_{1-x} coatings deposited on cemented carbide substrates using various C_2H_4/CH_3CN molar ratios was performed after sputtering each coating with Ar^+ ions from 0 to 100 min. Fig. 2.1 shows the profiles after 20 min of Ar+ sputtering.

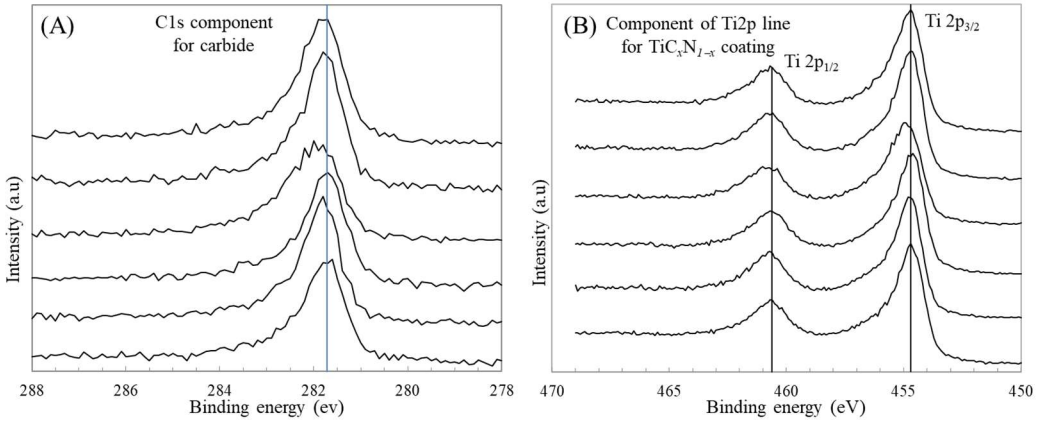

Fig. 2.1 (A) and (B) respectively represent shapes of the C1s and the Ti2p lines obtained via XPS after sputtering Ar^+ ions for t = 20 min on TiC_xN_{1-x} coatings with different C_2H_4/CH_3CN molar ratio: (a) C_2H_4/CH_3CN = 0, (b) C_2H_4/CH_3CN = 7, (c) C_2H_4/CH_3CN = 11, (d) C_2H_4/CH_3CN = 14, (e) C_2H_4/CH_3CN = 19, and (f) C_2H_4/CH_3CN = 30.

The spectra for the C1s and Ti2p levels are presented in Fig. 2.1(A) and (B), respectively. In Fig. 2.1(A), the single peak in each of the spectra for the C1s level at 281.7 eV is typical for carbides. The titanium Ti2p spectra presented in Fig. 2.1(B) with peaks at 455.9 eV and 460.5 eV, which are attributed to the $Ti2p_{3/2}$ and $Ti2p_{1/2}$ spin-orbit couplings of the Ti atoms in Ti(C,N) coatings, are also characteristic of titanium carbides. These combined results for Ti and C indicate that the Ti and C atoms exist in the TiC_xN_{1-x} coatings as titanium carbides, and that all carbon atoms were considered to be incorporated into the coatings.

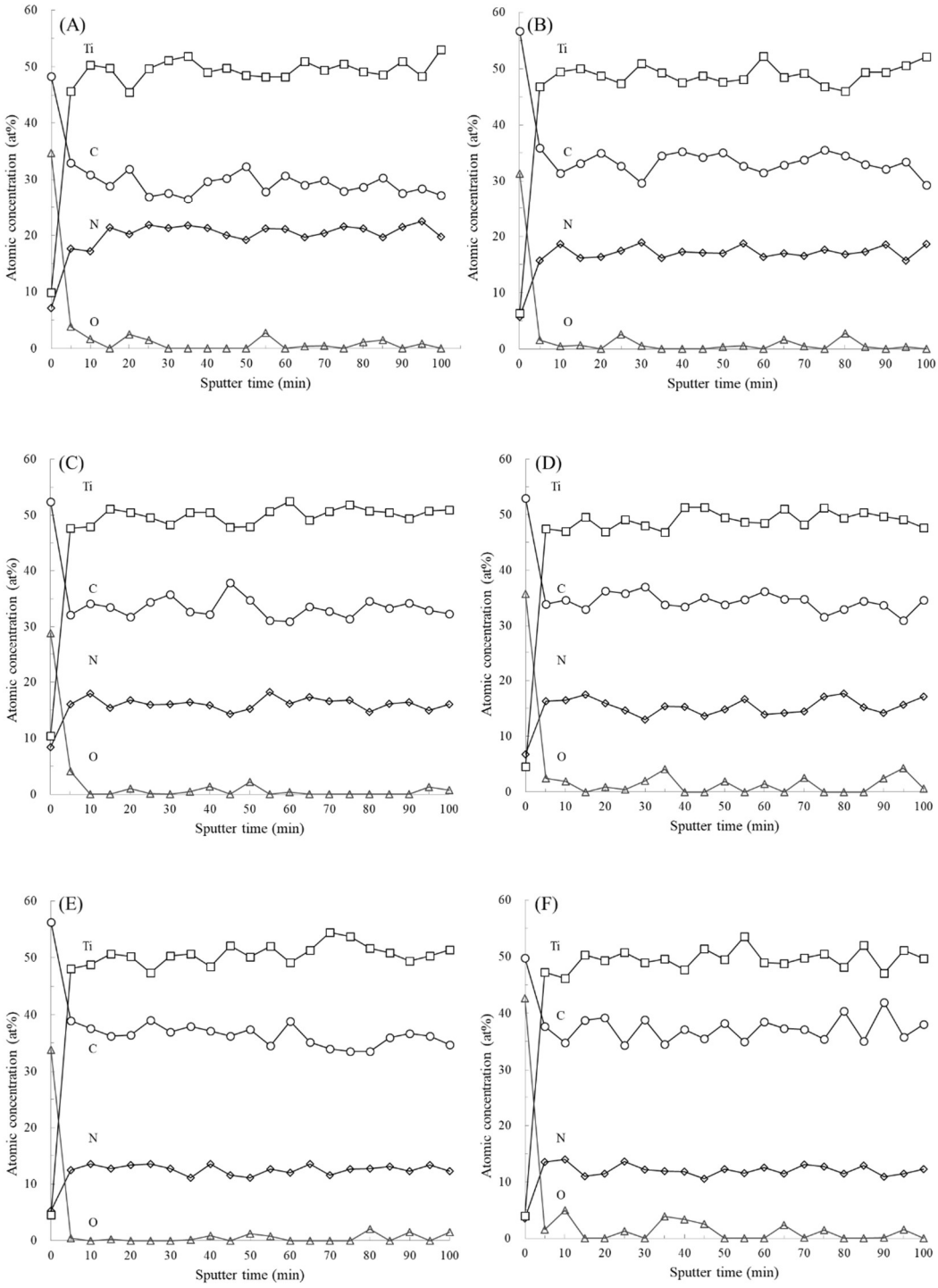

Fig. 2.2 Distributions of the elemental concentrations on the surface regions of TiC_xN_{1-x} coatings with different C_2H_4/CH_3CN molar ratio determined using XPS: (a) C_2H_4/CH_3CN = 0, (b) C_2H_4/CH_3CN = 7, (c) C_2H_4/CH_3CN = 11, (d) C_2H_4/CH_3CN = 14, (e) C_2H_4/CH_3CN = 19, and (f) C_2H_4/CH_3CN = 30.

Fig. 2.2 presents the semi-quantitative analyses of the chemical compositions of the TiC_xN_{1-x} coatings with various C_2H_4/CH_3CN molar ratios at different sputtering times. The high concentration of oxygen and carbon at the surface is considered to be adsorbate.

After Ar^+ sputtering, the concentration of oxygen decreased and the ratios of the concentrations of carbon, nitrogen, and oxygen to titanium were nearly stoichiometric. The concentration of oxygen below the surface of the coating was very low, and in fact, most of the values fell within the analytical error. The average chemical compositions free from surface adsorbates and the corresponding *x* values for the TiC_xN_{1-x} coatings calculated from the average C/(C+N) atomic concentration ratios are listed in Table 2.3.

Table 2.3 Semi-quantitative analysis for chemical composition of TiC_xN_{1-x} coating as a function of C_2H_4/CH_3CN molar ratio by XPS.

C_2H_4/CH_3CN molar ratio	Average chemical composition measured by XPS without adsorbate on surface of TiC_xN_{1-x} coating				
	C at%	N at%	O at%	Ti at%	*x* value in TiC_xN_{1-x}
0	29.3	20.5	0.8	49.4	0.59 ± 0.03
7	33.3	17.2	0.6	48.9	0.66 ± 0.02
11	33.3	16.2	0.6	49.9	0.67 ± 0.02
14	34.3	15.4	1.2	49.1	0.69 ± 0.03
19	36.4	12.6	0.5	50.6	0.74 ± 0.01
30	37.2	12.1	1.2	49.5	0.75 ± 0.02

The *x* values in the TiC_xN_{1-x} coatings increased as the C_2H_4/CH_3CN molar ratio increased, with a maximum *x* of 0.75 achieved at C_2H_4/CH_3CN = 30. Fig. 2.3(A) shows the XRD patterns of the TiC_xN_{1-x} coatings with various C_2H_4/CH_3CN molar ratios deposited on cemented carbide substrates at 840°C and 9 kPa for 200 min. The TiC_xN_{1-x} coatings exhibited a (422) preferred orientation. Enlargement of the (422) diffraction peaks, which shifted to lower values and broadened as the C_2H_4/CH_3CN molar ratio increased, can be seen in the corresponding patterns in Fig. 2.3(B).

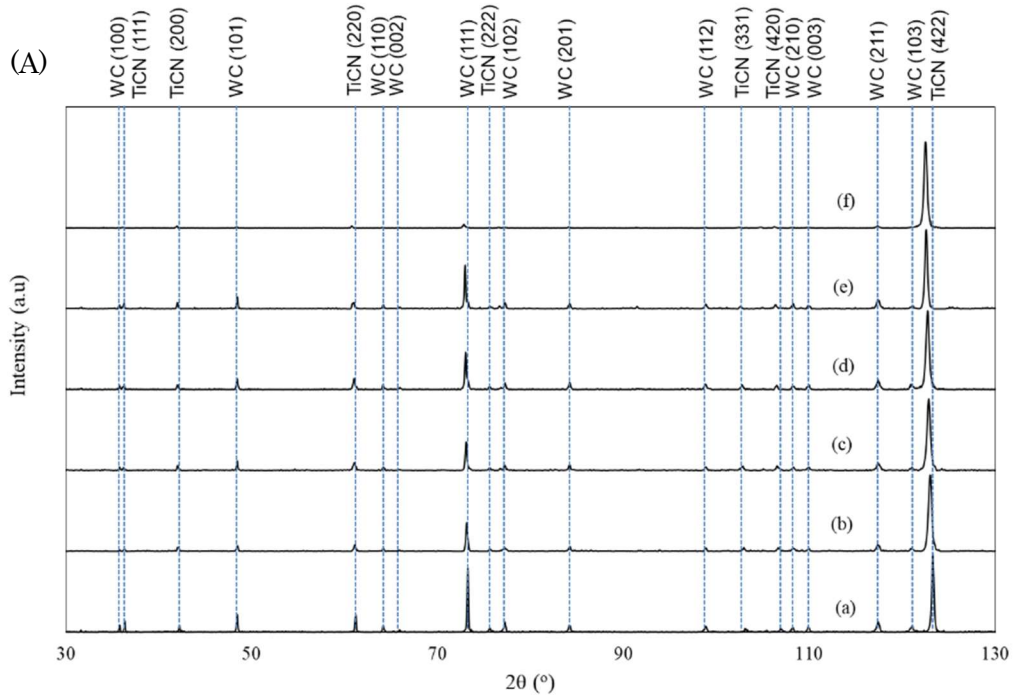

Fig. 2.3(A) XRD patterns for TiC_xN_{1-x} coatings on carbide substrates with different C_2H_4/CH_3CN molar ratio at 840°C and 9 kPa: (a) C_2H_4/CH_3CN = 0, (b) C_2H_4/CH_3CN = 7, (c) C_2H_4/CH_3CN = 11, (d) C_2H_4/CH_3CN = 14, (e) C_2H_4/CH_3CN = 19, and (f) C_2H_4/CH_3CN = 30.

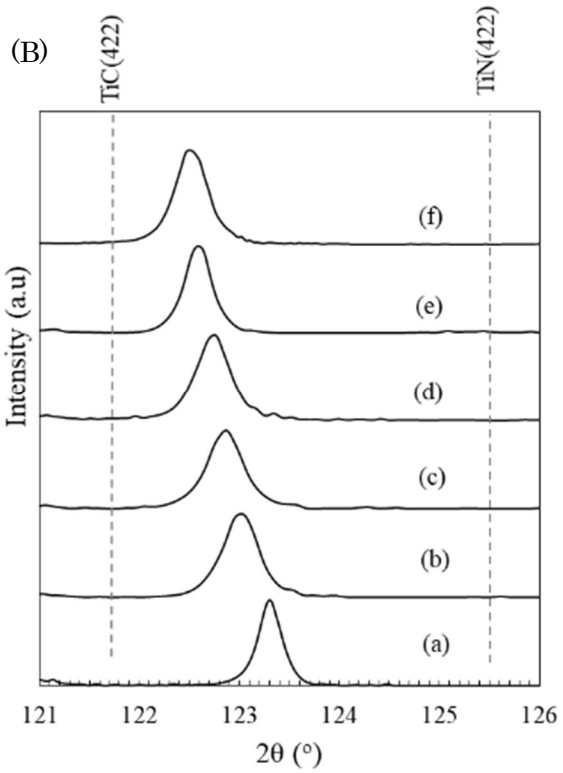

Fig. 2.3(B) Enlarged views of the (422) diffractions of TiC_xN_{1-x} coatings on carbide substrates with different C_2H_4/CH_3CN molar ratio at 840°C and 9 kPa: (a) C_2H_4/CH_3CN = 0, (b) C_2H_4/CH_3CN = 7, (c) C_2H_4/CH_3CN = 11, (d) C_2H_4/CH_3CN = 14, (e) C_2H_4/CH_3CN = 19, and (f) C_2H_4/CH_3CN = 30.

Fig. 2.4 plots the relationships between the lattice parameters and *x* values for the TiC_xN_{1-x} coatings with increasing C_2H_4/CH_3CN molar ratio. It can be seen that the *x* value increased from 0.59 and became saturated at approximately 0.74 as the C_2H_4/CH_3CNmolar ratio increased from 0 to 19. However, a further increase in the C_2H_4/CH_3CN molar ratio did not significantly influence the *x* value (x_{max} = 0.75). A similar trend was observed for the lattice parameters of the TiC_xN_{1-x} coatings as a function of the C_2H_4/CH_3CN molar ratio. Based on these combined results, it was determined that the maximum solubility of carbon in the TiC_xN_{1-x} coatings in the present study was limited to $x = 0.75 \pm 0.02$, and the maximum lattice parameter was 4.036 Å.

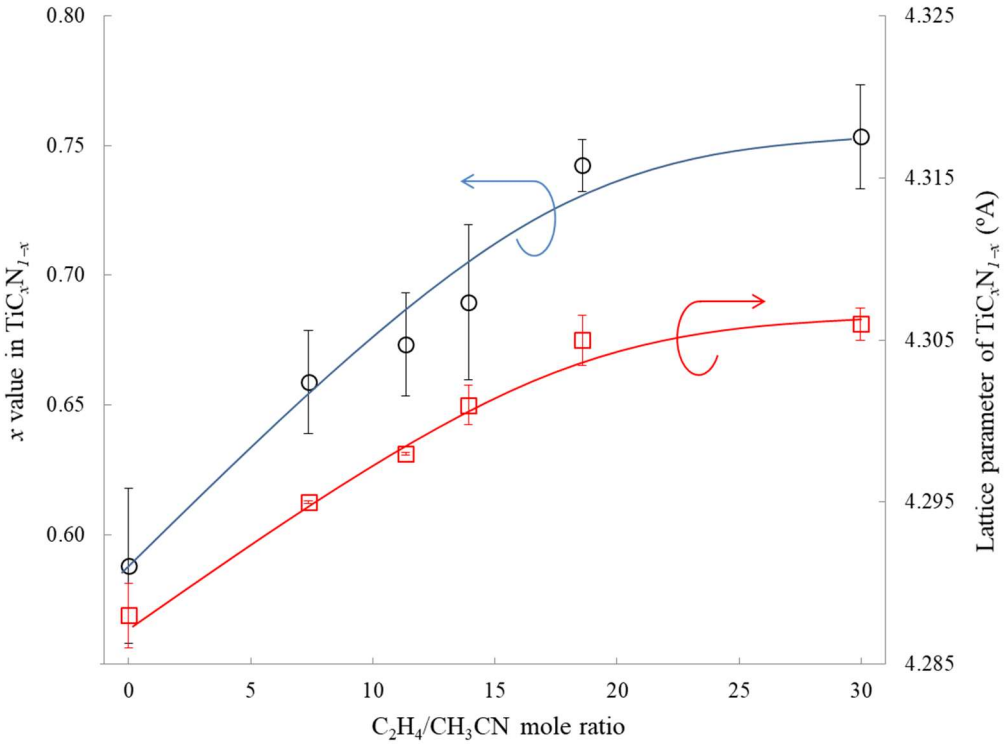

Fig. 2.4 Plot of the x values and lattice parameters of TiC_xN_{1-x} coatings at 840°C and 9 kPa as a function of the C_2H_4/CH_3CN molar ratio

Fig. 2.5 shows the change in the crystallite size in the TiC_xN_{1-x} coatings derived from the FWHM of the (422) diffraction peaks as a function of the *x* value. As can be seen in the figure, the crystallite size initially decreased as the *x* value in the TiC_xN_{1-x} increased to 0.69, but then increased at *x* values > 0.69. At *x* = 0.59, the average crystallite size was 49 nm, and a minimum crystallite size of 39 nm was obtained when *x* varied from 0.67 to 0.69.

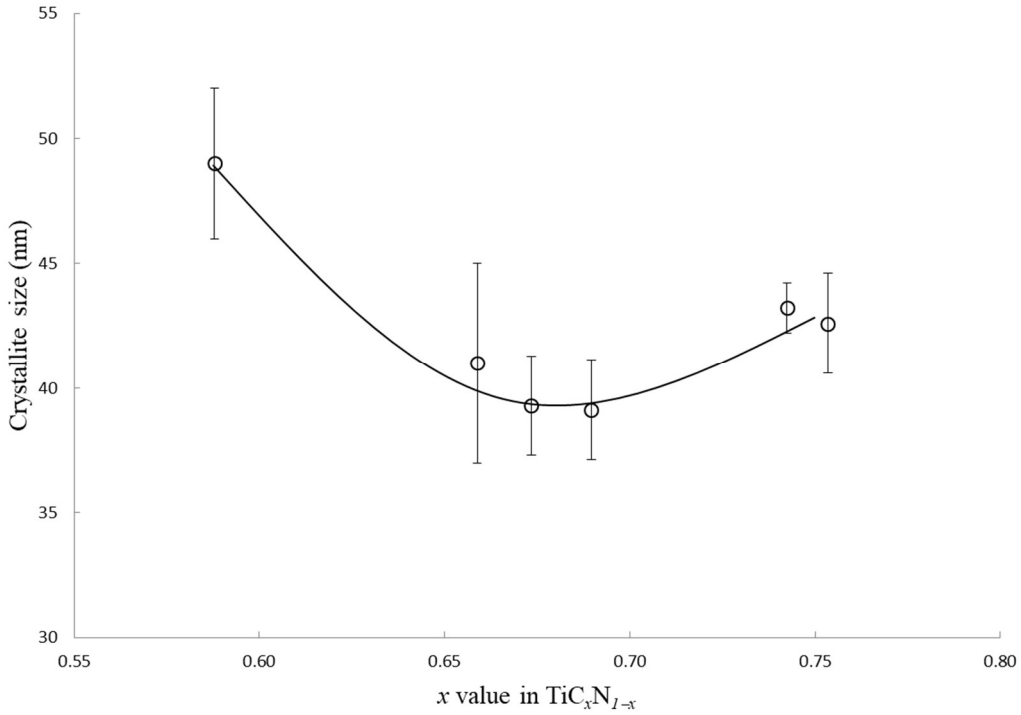

Fig. 2.5 Crystallite size of TiC_xN_{1-x} coatings as a function of the x value.

Fig. 2.6 presents SEM images of the surfaces and cross sections of the TiC_xN_{1-x} coatings with various *x* values. Notably, in the cross sectional images for the TiC_xN_{1-x} coatings with *x* b 0.74, a fine columnar structure (grain size < 0.5 μm) with a lenticular-like morphology was observed on the surfaces (Fig. 2.6(A)–(C)). However, the morphology changed to coarse grains with a rough surface when $x \geq 0.74$ (Fig. 2.6(D)). This tendency is similar to that observed for the (422) crystallite sizes of the TiC_xN_{1-x} coatings (Fig. 2.5).

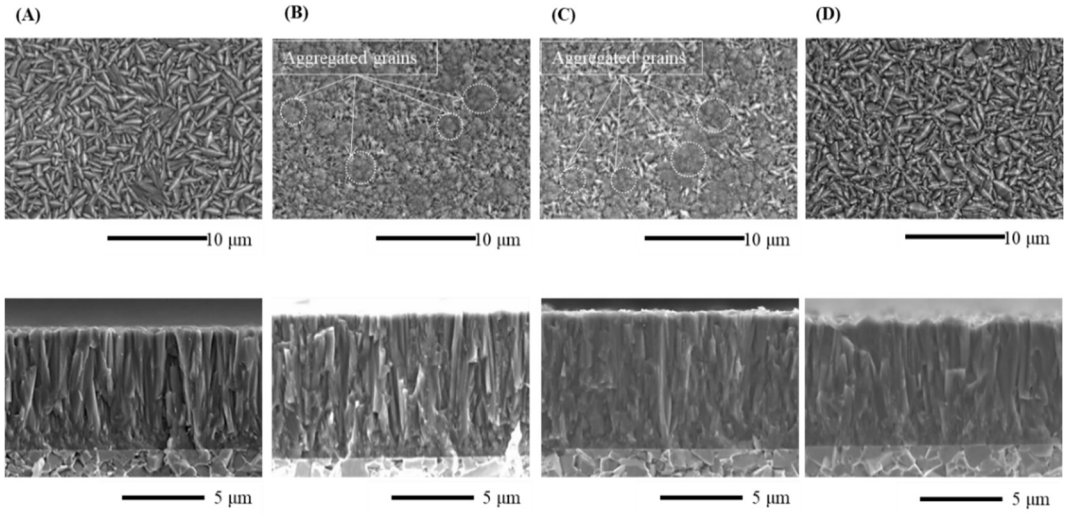

Fig. 2.6 SEM images of the surfaces and cross sections of TiC_xN_{1-x} coatings with various x values: (A) $TiC_{0.59}N_{0.41}$ (x = 0.59), (B) $TiC_{0.67}N_{0.33}$ (x = 0.67), (C) $TiC_{0.69}N_{0.31}$ (x = 0.69), and (D) $TiC_{0.74}N_{0.26}$ (x = 0.74).

Optical micrographs of mirror-polished and chemically etched cross sections of the TiC_xN_{1-x} coatings with different *x* values can be seen in Fig. 2.7. The increase in the thickness of the TiC_xN_{1-x} coatings with the *x* value reflects an increase in the deposition rate. The deposition rates for the TiC_xN_{1-x} coatings were measured for two different batches of each coating and calculated to be 2.2 μm/h at *x* = 0.66 to 0.69 and approximately 1.9 μm/h at *x* = 0.55, 0.74, and 0.75. Furthermore, a greater contrast between the $TiC_{0.59}N_{0.41}$ bonding layer and each TiC_xN_{1-x} coating as the *x* value increased can be clearly observed, and is due to the increasing differences in the chemical compositions of the two layers. The change in microstructure from a columnar to a granular-like structure and the formation of an inhomogeneous interphase between the TiC_xN_{1-x} (*x* = 0.74 to 0.75) coatings and the bonding layer can also be clearly seen. This inhomogeneous interphase is considered to form via diffusion of Co from the WC–5wt%Co substrate because of the characteristics of the chemical etchant.

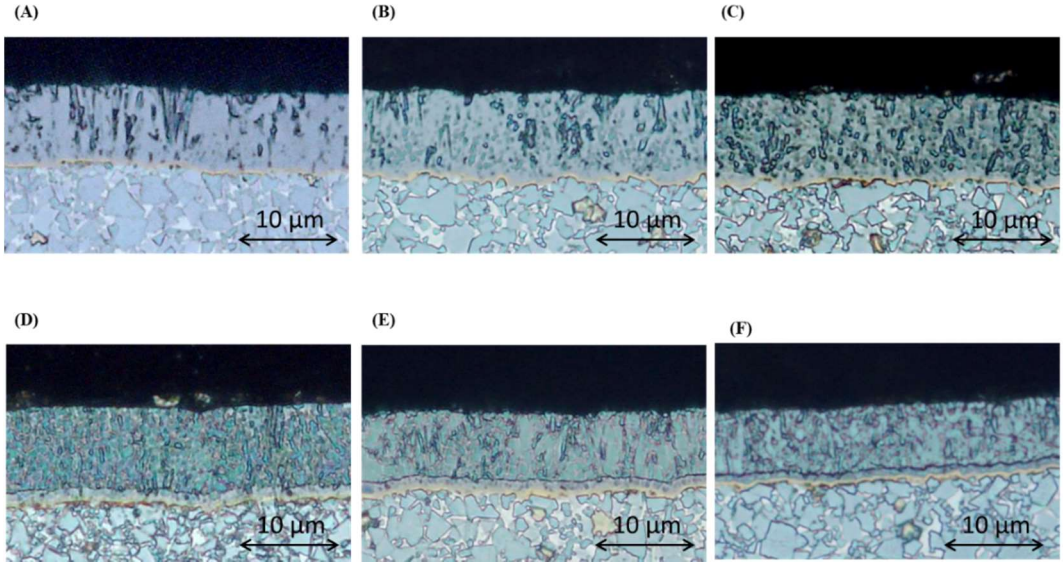

Fig. 2.7 Optical micrograph images of mirror polished and chemical etched cross sections of TiC_xN_{1-x} coatings with various x values: (A) $TiC_{0.59}N_{0.41}$ (x = 0.59), (B) $TiC_{0.66}N_{0.34}$ (x = 0.66), (C) $TiC_{0.67}N_{0.33}$ (x = 0.67), (D) $TiC_{0.69}N_{0.31}$ (x = 0.69), (E) $TiC_{0.74}N_{0.36}$ (x = 0.74), and (F) $TiC_{0.75}N_{0.35}$ (x = 0.75).

2.3.2. Mechanical properties

Fig. 2.8 shows the effect of the *x* value on the indentation hardness of the TiC_xN_{1-x} coatings. The indentation hardness increased with an increase in the *x* value from 26.3 GPa at *x* = 0.59 to 28.5 GPa at *x* values of 0.66 to 0.69, and then decreased to 27.2 GPa when $x \geq 0.74$. The change in the hardness as a function of the crystallite size is shown in Fig. 2.9. It can be seen from the figure that the hardness increased proportionally to the decrease in the crystallite size, possibly because of the grain refinement effect. Fig. 2.10 plots the adhesion of the TiC_xN_{1-x} coatings to the carbide substrate as a function of the *x* value. The coatings with $x \geq 0.74$ exhibited an adhesion value of 31 N, which is 30% lower than that of the coating with *x* = 0.59 (44 N). Thus, the adhesion of the coatings to the carbide substrate exhibited a proportional decrease as the carbon content increased.

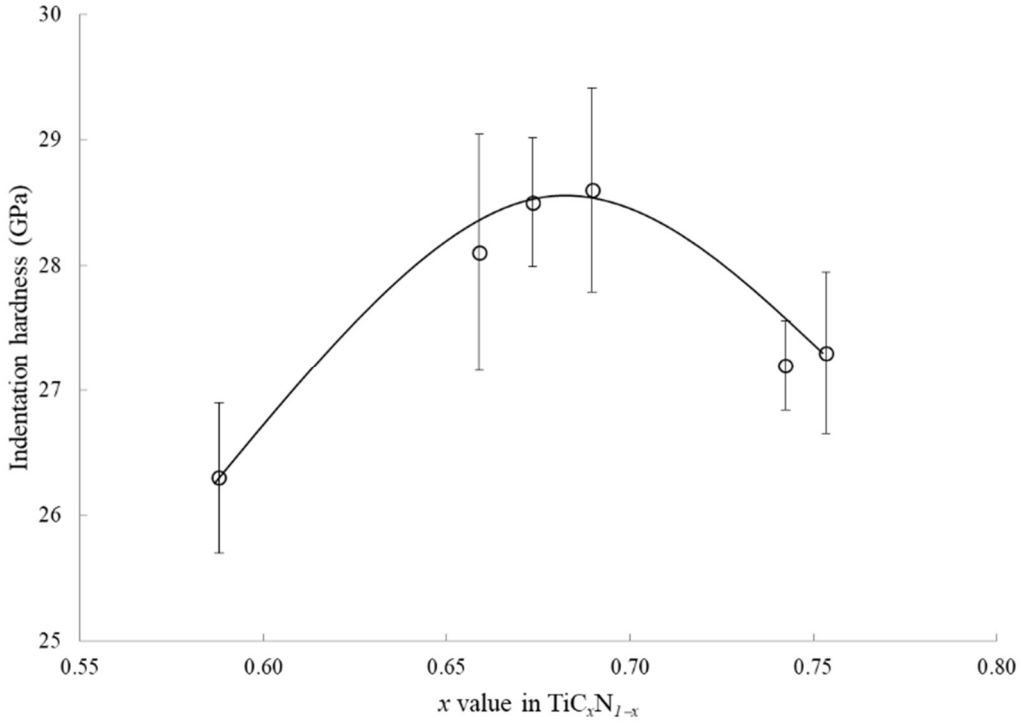

Fig. 2.8 Change in the indentation hardness of TiC_xN_{1-x} coatings as a function of the x value.

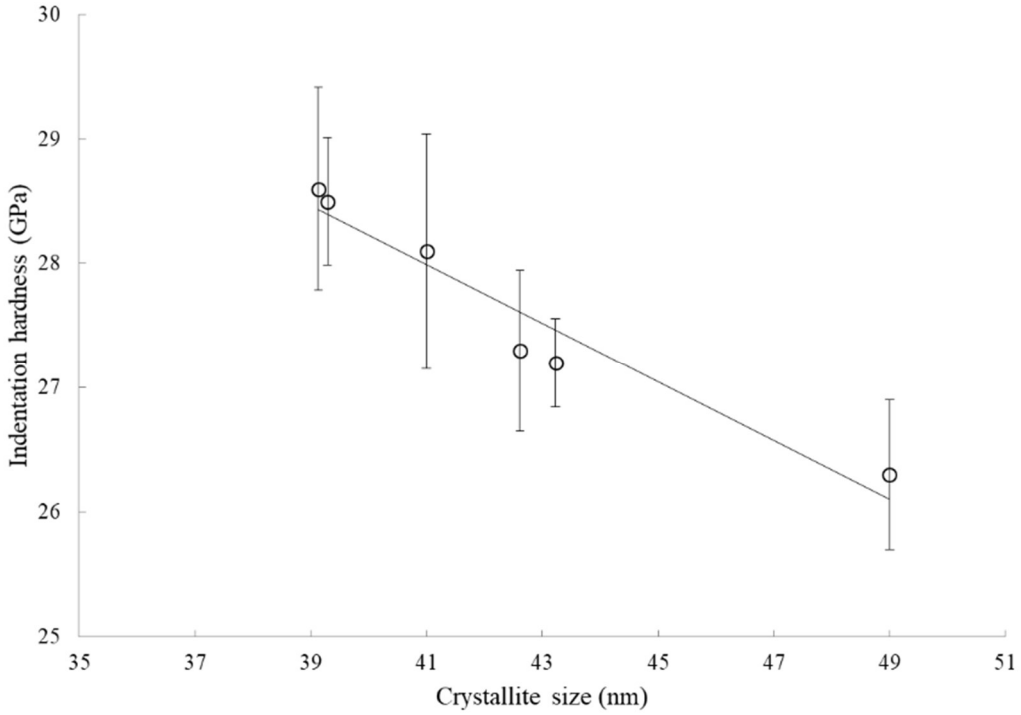

Fig. 2.9 Relationship between the crystallite size and hardness for TiC_xN_{1-x} coatings

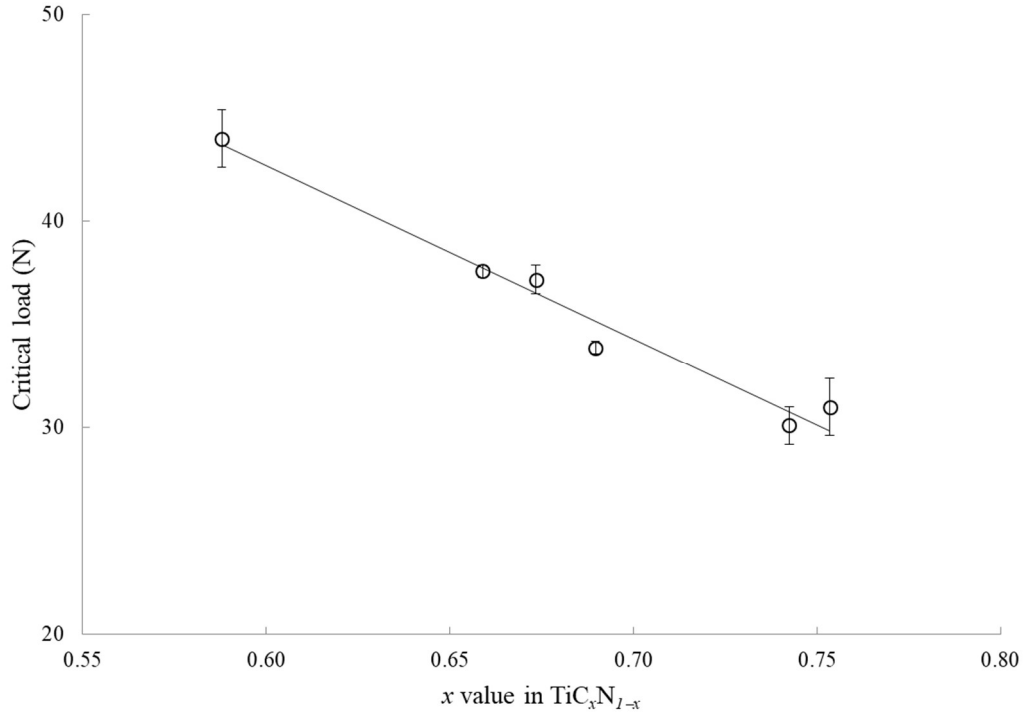

Fig. 2.10 Change in the adhesion of TiC_xN_{1-x} coatings as a function of the x value

2.3.3. Cutting performance

Fig. 2.11 shows the results for a longitude turning operation test using ductile cast iron (AISI:100-70-03), which was employed to evaluate the cutting performance of the TiC_xN_{1-x}(10 μm)/Al_2O_3(5 μm) coatings as a function of the *x* value (*x* = 0.59 to 0.74). The TiC_xN_{1-x} coatings with *x* values varying from 0.66 to 0.69 (Fig. 2.11(B)–(D)) exhibited better wear resistance than that of a commercially available *x* = 0.59 coating (Fig. 2.11(A)) and the coating with a high *x* value of 0.74 (Fig. 2.11(E)). After 20 min of the cutting test, the coatings with *x* ranging from 0.66 to 0.69 also exhibited flank wear that were approximately 36% and 53% less than the coatings with *x* = 0.59 and 0.74, respectively. Table 2.4 summarizes the mechanical properties and cutting performance results for the TiC_xN_{1-x} coatings.

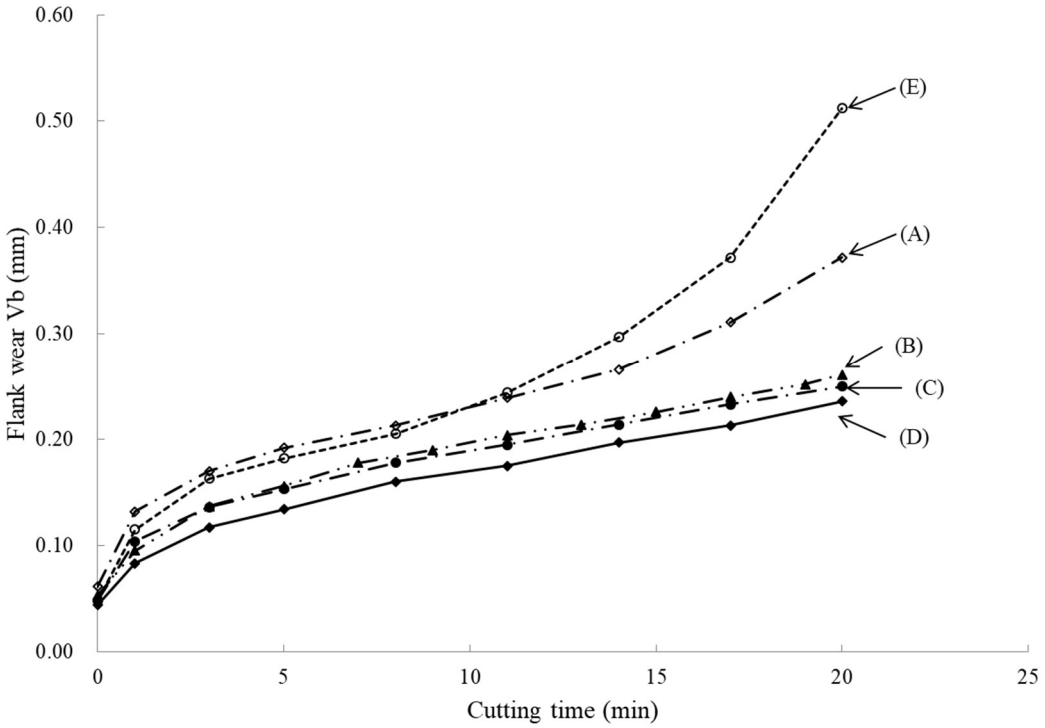

Fig. 2.11 Influence of the x value of TiC_xN_{1-x} (10μm)/α-Al_2O_3(5μm) coatings on their wear resistance during longitude turning on ductile cast iron (AISI:100-70-03): (A) x = 0.59, (B) x = 0.66, (C) x = 0.67, (D) x = 0.69, and (E) x = 0.74

Table 2.4 Experimentally determined mechanical properties and cutting performance of the TiC_xN_{1-x} coatings

C_2H_4/CH_3CN molar ratio	*x* value in TiC_xN_{1-x}	Lattice parameter (°A)	Crystallite size $D_{(422)}$ (nm)	Indentation hardness (GPa)	Coating adhesion (N)	Flank wear at 20 min (mm)
0	0.59 ± 0.03	4.288	49 ± 3	26.3 ± 0.6	44.0 ± 1.4	0.37
7	0.66 ± 0.02	4.295	41 ± 4	28.1 ± 0.9	37.6 ± 0.3	0.26
11	0.67 ± 0.02	4.298	39 ± 2	28.5 ± 0.5	37.2 ± 0.7	0.25
14	0.69 ± 0.03	4.301	39 ± 2	28.6 ± 0.8	33.9 ± 0.3	0.24
19	0.74 ± 0.01	4.305	43 ± 1	27.2 ± 0.4	30.1 ± 0.9	0.51
30	0.75 ± 0.02	4.306	43 ± 2	27.3 ± 0.4	31.0 ± 1.4	N/A

2.4. Discussion

2.4.1. Deposition of the TiC_xN_{1-x} coatings

In this study, TiC_xN_{1-x} coatings with various *x* values (*x* = 0.59 to 0.75) were investigated in terms of their microstructure, hardness, adhesion, and cutting performance. The increase in the *x* value of the TiC_xN_{1-x} coatings was achieved by adding C_2H_4 gas to a conventional MT-CVD process using a $TiCl_4$–CH_3CN–H_2 precursor system [1]. Given the relatively high

chemical activation of C_2H_4 gas at moderate temperature (800–900°C), increasing the C_2H_4/CH_3CN molar ratio resulted in an increase in the carbon concentration in the TiC_xN_{1-x} coatings (Fig. 2.2(A)–(F)) and Table 2.3). The maximum solubility of the carbon atoms in the TiC_xN_{1-x} coatings at 840°C and 9 kPa was determined to be C = 37 at.%, with a corresponding *x* value calculated from the C/(C+N) atomic concentration ratio of 0.75. The increasing incorporation of carbon atoms into the TiC_xN_{1-x} coatings was confirmed by the changes in the lattice parameters of the TiC_xN_{1-x} coatings. The lattice constant should increase as more carbon atoms are incorporated into the coating because of the nature of TiN–TiC solid solution systems. This result was also supported by the shift to lower values of the (422) diffraction peaks observed in the XRD patterns (Fig. 2.3). The maximum *x* value in the TiC_xN_{1-x} coatings deposited in this study was determined to be 0.75 as a result of saturation when the C_2H_4/CH_3CN molar ratio was >19 (Fig. 2.4). A further increase in the C_2H_4/CH_3CN molar ratio did not influence the chemical compositions or lattice parameters of the coatings. These results indicated that all the carbon atoms were incorporated as carbide compounds, which were also clearly confirmed by the presence of the $Ti2p_{3/2}$, $Ti2p_{1/2}$, and C1s peaks observed in the XPS spectra (Fig. 2.1(A) and (B)). The increase in the *x* value in the TiC_xN_{1-x} coatings prepared via MT-CVD using C_2H_4 gas can possibly be explained by the following reactions:

$$6TiCl_4(g) + 2CH_3CN(g) + 9H_2(g) \rightarrow 4TiC(s) + 2TiN(s) + 24HCl(g) \quad Eq.(2.2)$$

$$4TiCl_4(g) + 2CH_3CN(g) + 9H_2(g) \rightarrow 2TiC(s) + 2TiN(s) + 2CH_4(g) + 16HCl(g) \quad Eq.(2.3)$$

where (s) indicates the solid phase and (g) indicates the gas phase. At temperatures of approximately 850°C, the overall reaction reported by Bonetti et al. [1] was assumed to be that in Eq(2.2), for which the *x* value in the TiC_xN_{1-x} coating was reported to be 0.63. At lower temperature (780°C), a different reaction assumed to be Eq. (2.3) was favored and resulted in a higher N content, and thus the *x* value was reported to be 0.54. More recent studies of MT-CVD reported by A. Larsson et al. [8] and I. Dreiling et al. [9] revealed that at a deposition temperature of 850°C, the *x* value was approximately 0.61. In the present study, without C_2H_4 in the feed gas at 840°C, the *x* value of the generated TiC_xN_{1-x} coating was determined

to be 0.59 ± 0.03, which is in good agreement with the previously reported results [8, 9]. Feeding C_2H_4 gas to $TiCl_4$–CH_3CN–H_2 during the MT-CVD process at a temperature of 840°C thus leads to an increase in the *x* value of the TiC_xN_{1-x} coatings, which likely occurs via the reaction presented in Eq. (2.4):

$$8TiCl_4(g) + 2CH_3CN(g) + C_2H_4(g) + 11H_2(g) \rightarrow 6TiC(s) + 2TiN(s) + 32HCl(g) \quad Eq.(2.4)$$

According to Eq. (2.4), a complete reaction in the equilibrium state with 8 vol% $TiCl_4$, 2 vol% CH_3CN, and 1 vol% C_2H_4 should result in a TiC_xN_{1-x} coating with $x = 0.75$. In this study, an excess of $TiCl_4$ and C_2H_4 was used to obtain TiC_xN_{1-x} coatings with *x* values > 0.75. However, the maximum *x* value observed in this study was 0.75 (Fig. 2.4). This result is considered to be due to the low chemical reactivity and short residence time of the C_2H_4 gas during CVD at 840°C and 9 kPa. Thus, increasing the deposition temperature is considered to be an effective method for increasing the *x* value in the TiC_xN_{1-x} coatings. Recently, C. Czettl et al. [12] used C_2H_6 gas for the low-pressure CVD of $TiC_xN_yB_{1-(x+y)}$ hard coatings from a $TiCl_4$–C_2H_6–H_2–N_2–BCl_3 precursor system. The C_2H_6 gas was used to decrease the deposition temperature and avoid the formation of a brittle W–Co–B-like η-phase. At a deposition temperature of 920°C and 16 kPa, the *x* value of the $TiC_xN_yB_{1-(x+y)}$ coatings varied from 0.80 to 0.91 depending on the incorporated B content. These results [18] suggest that increasing the deposition temperature and pressure during fabrication of the TiC_xN_{1-x} coatings using a $TiCl_4$–CH_3CN–C_2H_4–H_2 precursor system may be an effective method for increasing the *x* value. A higher deposition temperature and pressure may increase the chemical reactivity of the C_2H_4 and should also influence the mechanical properties of the TiC_xN_{1-x} coatings.

2.4.2. Microstructure, mechanical properties, and cutting performance

2.4.2.1. Microstructure

The effect of the *x* value of the TiC_xN_{1-x} coatings on the microstructure was investigated. As the *x* value increased, the crystallite size of the TiC_xN_{1-x} coatings decreased (Fig. 2.5).

The minimum crystallite size $D_{(422)}$ was 39 nm for *x* values ranging from 0.66 to 0.69, and fine grains (<0.5 μm) with some aggregate grains were observed for these coatings (Fig. 2.6(B) and (C)). The decrease in the crystallite size with the *x* value is considered to result from an increase in the deposition rate of the TiC_xN_{1-x} coatings, which results in more rapid and denser nucleation. The deposition rate of the TiC_xN_{1-x} coatings, which was calculated from the thicknesses of polished cross sections, was found to be 2.2 μm/h when *x* ranged from 0.66 to 0.69, and was 15% higher than that when *x* = 0.55, 0.74, and 0.75 (approximately 2.0 μm/h). Because the deposition rate of the TiC_xN_{1-x} coatings and its effect on their microstructure are strongly influenced by the deposition parameters, it was concluded that C_2H_4/CH_3CN molar ratio from 7 to 14 is preferred for the deposition of TiC_xN_{1-x} coatings via CVD at 840°C and 9 kPa using a $TiCl_4$–CH_3CN–C_2H_4–H_2 precursor system. The effect of the *x* value on the indentation hardness of the TiC_xN_{1-x} coatings was also studied (Fig. 2.8).

2.4.4.2. Hardness

The hardness increased with *x* and reached a maximum value of 28.6 GPa at approximately *x* = 0.69. The indentation hardness of the TiC_xN_{1-x} coatings is considered to be influenced more by the microstructure than the chemical composition or the lattice strain. The plot of the hardness as a function of the crystallite size calculated from the FWHMs of the (422) diffraction peaks according to Scherrer's equation exhibits a good linear relationship (Fig. 2.9); this behavior is attributed to the crystallite refinement effect. An effort to measure the size–strain relationship using the Williamson–Hall method was undertaken; however, the strain was sufficiently small and could be ignored. This result explains the similar proportional change in the lattice parameters with the *x* value and C_2H_4/CH_3CN molar ratio (Fig. 2.4). Hyakutake et al. [17] reported an increase in the micro-hardness with *x* for TiC_xN_{1-x} mixed crystal films prepared via RF magnetron sputtering. According to the report, this increase in hardness with the *x* value was considered to be due to changes in the microstructure, rather than the lattice strain.

2.4.5. Adhesion

The adhesion of the TiC_xN_{1-x} coatings to carbide substrates decreased as the *x* value increased (Fig. 2.10). Notably, TiC_xN_{1-x} coatings readily exfoliated when $x > 0.74$. This result is considered to be due to the increase in the discontinuous interphase between the $TiC_{0.59}N_{0.41}$ bonding layer and the TiC_xN_{1-x} coatings as the *x* value increased, which was observed in the optical micrographs of mirror-polished and chemically etched cross sections of the TiC_xN_{1-x} coatings (Fig. 2.7). With respect to the etching characteristics of the Murakami reagent, the discontinuous interphase is assumed to form as a result of the diffusion of Co metal from the WC–Co substrate. The diffusion of Co to TiC_xN_{1-x} coatings is known to occur during low-pressure CVD processes [18]. Given that a change in the morphology from a columnar to a granular-like structure occurred as the *x* value increased (Fig. 2.7(D)–(F)), it is reasonable to assume that the morphology affected the diffusion path and capillary attraction of Co to the TiC_xN_{1-x} coating. The presence of Co at the interphase of the $TiC_{0.59}N_{0.41}$ bonding layer and the TiC_xN_{1-x} coating possibly led to a decrease in the adhesion of the coating as the *x* value increased. Thus, the weak point is considered to be the $TiC_{0.59}N_{0.41}$/ TiC_xN_{1-x} interphase layer.

2.4.6. Cutting performance

The cutting performance of TiC_xN_{1-x} coatings with different *x* values ($x = 0.59$ to 0.74) was evaluated using TiC_xN_{1-x} (10 μm)/Al2O3 (5 μm)-coated inserts and a longitude turning operation on ductile cast iron (Fig. 2.11). A high performance tool for cast iron turning must have a coating with both high hardness and good adhesion to the substrate to overcome the cohesive and abrasive wear nature of this work material. Both cohesive wear and abrasive wear on the cutting edge of the insert were observed using a microscope. Notably, the TiC_xN_{1-x} /α-Al_2O_3 coatings with *x* ranging from 0.66 to 0.69 (Fig. 2.11(B)–(D)) exhibited less flank wear than a benchmark $TiC_{0.59}N_{0.41}$ ($x = 0.59$)/α-Al_2O_3 coating considered to have higher hardness (Fig. 2.8), and thus showed higher abrasive wear resistance. On the other hand, the flank wear rapidly increased for the TiC_xN_{1-x} coatings with $x > 0.74$ because of early exfoliation of the coatings. The observed exfoliation was possibly due to the low adhesion of the coatings (Fig. 2.10) as a result of the presence of a discontinuous interphase

containing diffused Co atoms between the TiC_xN_{1-x} ($x > 0.74$) coatings and the $TiC_{0.59}N_{0.41}$ bonding layer (Fig. 2.7(E)).

2.5. Summary

The deposition of TiC_xN_{1-x} coatings with varied x values was conducted by introducing C_2H_4 gas to a $TiCl_4$–CH_3CN–H_2 precursor system during moderate temperature low-pressure CVD. The microstructure, mechanical properties, and cutting performance of TiC_xN_{1-x}-coated carbide inserts as a function of the x value were evaluated. XPS analyses confirmed an increase in the incorporated carbon content in the TiC_xN_{1-x} coatings as the C_2H_4/CH_3CN molar ratio increased, with a maximum x value reaching 0.75 because of saturation, as determined from the lattice parameters and chemical composition analyses. The indentation hardness of the TiC_xN_{1-x} coatings increased as the crystallite size decreased and reached a maximum hardness of 28.5 GPa for x values ranging from 0.66 to 0.69. However, as the x value of the TiC_xN_{1-x} coatings increased, the morphology changed from a fine columnar structure to a coarse granular-like structure. These changes in the microstructure, which were accompanied by the formation of a discontinuous interphase containing diffused Co atoms between the TiC_xN_{1-x} coatings and the $TiC_{0.59}N_{0.41}$ bonding layer, influenced the adhesion of the coatings. A longitude turning operation test on ductile cast iron (AISI: 100-70-03) was performed using TiC_xN_{1-x} (10 μm)/Al_2O_3 (5 μm)-coated carbide inserts with x ranging from 0.59 to 0.74. The TiC_xN_{1-x} coatings with x values ranging from 0.66 to 0.69 exhibited a significant increase in tool life compared with a commercially available coated carbide tool. Thus, variation in the feed gas system offers the possibility of depositing higher performance TiC_xN_{1-x} coatings at low temperature with high incorporated carbon concentrations and high hardness due to microstructure refinement. However, further improvements in the adhesion of these coatings to carbide substrates require avoidance of the formation of a discontinuous interphase due to a change in the chemical composition and microstructure. Control of the chemical compositions of the TiN base and TiCN bonding layers and the TiC_xN_{1-x} coatings using optimized deposition pressures and temperatures should be an effective approach.

References in chapter 2

[1] R.S. Bonetti, H. Wiprächtiger, E. Mohn, Met. Powder Rep. 45 (1990) 837–840.

[2] E. Kübel, Surf. Coat. Technol. 49 (1991) 268–274.

[3] A.T. Santhanam, D.T. Quinto, G.P. Grab, Int. J. Refract. Met. Hard Mater. 14 (1996) 31–40.

[4] H.G. Prengel,W.R. Pfouts, A.T. Santhanam, Surf. Coat. Technol. 102 (1998) 183–190.

[5] S.J. Bull, D.G. Bhat, M.H. Staia, Surf. Coat. Technol. 163–164 (2003) 499–506.

[6] S.J. Bull, D.G. Bhat, M.H. Staia, Surf. Coat. Technol. 163–164 (2003) 507–514.

[7] S. Kudapa, K. Narasimhan, P. Boppana, W.C. Russell, Surf. Coat. Technol. 120–121(1999) 259–264.

[8] A. Larsson, S. Ruppi, Thin Solid Films 402 (2002) 203–210.

[9] I. Dreiling, A. Haug, H. Holzschuh, T. Chassé, Surf. Coat. Technol. 204 (2009) 1008–1012.

[10] J. Garcia, R. Pitonak, R. Weissenbacher, A. Köpf, Surf. Coat. Technol. 205 (2010) 2322–2327.

[11] C. Czettl, C. Mitterer, U. Mühle, D. Rafaja, S. Puchner, H. Hutter, M. Penoy, C. Michotte, M. Kathrein, Surf. Coat. Technol. 206 (2011) 1691–1697.

[12] C. Czettl, C. Mitterer, M. Penoy, C. Michotte, M. Kathrein, Surf. Coat. Technol. 215 (2013) 127–132.

[13] S. Vepřek, M. Haussmann, S. Reiprich, L. Shizhi, J. Dian, Surf. Coat. Technol. 86–87(Part 1) (1996) 394–401.

[14] L. Karlsson, L. Hultman, M.P. Johansson, J.E. Sundgren, H. Ljungcrantz, Surf. Coat. Technol. 126 (2000) 1–14.

[15] Y.H. Cheng, T. Browne, B. Heckerman, E.I. Meletis, Surf. Coat. Technol. 205 (2011) 4024–4029.

[16] J. Watanabe, Y. Sone, US Patent No. US7906230 (2011).

[17] H. Hyakutake, Y. Imada, F. Honda, K. Nakajima, J. Phys. Condens. Matter 10 (1998) 111–121.

[18] T. Tetsuya, Japan Patent No. JP13826494 (1995).

Chapter 3. Improvement of mechanical properties and cutting performance of modified MT-TiC_xN_{1-x} coating by moderate temperature chemical vapour deposition

3.1. Introduction

To meet the demands of metal cutting applications, the hard protective coatings used on cutting tools must be very resistant to abrasive wear, very tough, and chemically stable at elevated temperatures. Hard coatings such as TiN, TiC, TiCN, TiAlN, and Al2O3 deposited by physical vapour deposition (PVD) or chemical vapour deposition (CVD) [1, 2] onto cemented carbide substrate tools serve to enhance the cutting performance and cost efficiency of these tools. In particular, Al_2O_3 and TiC_xN_{1-x} CVD multilayer coatings are widely used in turning applications because of their excellent wear resistance and good adherence to substrates.

In the cutting tool industry, CVD of TiC_xN_{1-x} coatings is done by one of two processes. The first involves a high-temperature titanium carbon nitride coating process that uses the $TiCl_4$–H_2–N_2–CH_4 CVD precursor system [3, 4]. This process is performed at a high temperature of 950–1050°C [5, 6], which results in the formation of the undesired brittle η-phase at the substrate–coating interface [7–9]. The second is a moderate temperature CVD (MT-CVD) process wherein the $TiCl_4$–CH_3CN–H_2–N_2 precursor system is processed at 700 to 900°C and at a low pressure of $<10 \times 10^3$ Pa [10, 11]. Due to the lower deposition temperature, TiC_xN_{1-x} coatings by MT-CVD (MT-TiC_xN_{1-x}) have lower tensile thermal stress and do not form the brittle η-phase. These facts improve the toughness of the cutting tool and lead to extensive applications of MT-TiC_xN_{1-x} in metal cutting recently [12]. However, the cutting tool industry has recently been required to reduce its energy consumption and machining costs, which translates into a demand for greater cutting speeds and the use of materials that are hard to cut, which shorten tool life. Thus, coatings with higher wear resistance are strongly required by the industry. Considerable effort has been devoted to improve the cutting performance of MT-TiC_xN_{1-x} coatings by adding $ZrCl_4$ [13], BCl_3 [14] and CO [15, 16] to refine the structure, increase hardness, and improve the surface morphology. However, the mechanical properties of TiC_xN_{1-x} coatings are influenced by its carbon content. Watanabe

et al. [17] proposed a method for increasing the x value in TiC_xN_{1-x} coatings up to 0.9 and improving their wear resistance based on a process involving a mixture of reactive hydrocarbon gases and CH_3CN. Paseuth et al. [18] introduced a method to increase the carbon content in TiC_xN_{1-x} coatings and decrease crystallite size by adding C_2H_4 gas to the $TiCl_4$–CH_3CN–H_2 precursors system in low-pressure CVD. The effect of carbon fraction *x* on the microstructure, hardness, and cutting performance using a ductile cast iron (AISI: 100-70-03) was also previously reported. However, the adhesion of TiC_xN_{1-x} coatings by low-pressure CVD onto carbide substrates decreases with increasing *x* ($x \geq 0.65$) because of the formation of a discontinuous bonding interphase. To clarify this issue, the adhesion strength of the MT-TiC_xN_{1-x} coating to carbide substrate was increased while maintaining the fine microstructure, high hardness, and highly abrasive wear resistance by optimizing *x* (x=0.63) on the TiN base layer.

Here, a detailed report is presented of the grain structure, micro-orientation, and mechanical properties including the friction coefficients of modified MT-$TiC_{0.63}N_{0.37}$ coatings and the results are compared with those of a conventional MT-TiC_xN_{1-x} coating. In addition, the cutting performance obtained by longitudinal continuous turning of carbon steel, alloyed steel, and stainless steel and by intermittent turning tests with four-groove alloyed steel on as-deposited modified and conventional MT-TiC_xN_{1-x} coatings was investigated.

3.2. Experimental procedures

3.2.1. Coating deposition

Coating deposition tests were performed using a commercially available hot-wall low-pressure CVD system (SCT600 TH; SuCoTec AG). The modified MT-$TiC_{0.63}N_{0.37}$ coating was deposited using a $TiCl_4$–CH_3CN–C_2H_4–H_2 precursor system. For comparison, a conventional MT-TiC_xN_{1-x} coating was also deposited using a $TiCl_4$–CH_3CN–N_2–H_2 precursor system. The deposition parameters are listed in Table 3.1. WC–5wt%Co substrates (Sumitomo Electric Hardmetal Corp., SNMA120408) with mirror-polished surfaces and WC–8wt%Co–2wt%TiC–4wt%TaC cemented carbide inserts (P20 grade, CNMG120408-NGU-type geometry, Sumitomo Electric Hardmetal Corp.) were used to analyze the physical properties and perform the cutting tests, respectively. The samples

were loaded on the half-radius positions of the tray, as described previously [18]. A 0.5-µm-thick TiN base layer and an approximately 4-µm-thickMT-TiC_xN_{1-x} coating was then deposited. Precoating tests were conducted to verify proper deposition rates of both modified and conventional MT-TiC_xN_{1-x} coatings, and the coating thicknesses were adjusted by varying the deposition time.

Table 3.1 Deposition parameters used for preparation of coatings investigated.

	Modified MT-TiC_xN_{1-x} layer	MT-TiC_xN_{1-x} layer	TiN base layer
Temperature (°C)	850	850	900
Pressure (kPa)	6.0	6.0	16
Deposition Time (min)	200	220	60
Total gas flow (L/min)	77	90	60
$TiCl_4$ (vol%)	2.5	1.5	1.2
CH_3CN (vol%)	0.4	0.6	-
C_2H_4 (vol%)	0.6	-	-
N_2 (vol%)	-	8.9	25.1
H_2 (vol%)	Balance	Balance	Balance

3.2.2. Coating characterization

The chemical composition, microstructure, residual stress, hardness, friction coefficient (at room temperature and at 600°C), and adhesion of MT-TiC_xN_{1-x} coatings were investigated. The chemical compositions and depth profiles were evaluated using a glow-discharge optical emission spectroscope (GD-OES; GD-Profiler 2™, HORIBA Scientific). The calibration was performed on Al_2O_3, Ti, W, and Co (high purity reference material; Rare Metallic Co., Ltd.) and on 11XHPC3 and 13XNSC4 (MBH Analytical Ltd.) to allow a semi-quantitative analysis of O, Ti, W, Co, C, and N composition. The fractions *x* were determined from the average for the C/(C+N) atomic ratio calculated from sputtering times of 50–100 s at the coating surface. Structure and phase analyses were conducted by X-ray diffraction (XRD; RIGAKU, SmartLab, operated at 45 kV and 200 mA) with CuKα radiation and a Ni filter. The lattice parameters, coherently diffracting domain size and microstrain, for the TiC_xN_{1-x} coatings were obtained by applying whole powder pattern fitting [19] and Williamson–Hall analysis, respectively [20–21]. Residual in-plane stress was determined

using sin2ψ with 2θ = 61°, which corresponds to the (220) peak of TiC_xN_{1-x}. The residual stress was obtained by analyzing the gradient of 2θ−sin2ψ by applying an elastic modulus of 388GPa and a Poisson ratio of 0.19 [16]. The texture coefficients [TC(hkl)], reflecting preferential growth directions, were calculated using [22].

$$\mathrm{TC(hkl)} = \frac{I(hkl)}{I_0(hkl)}\left\{\frac{1}{n}\sum\frac{I(hkl)}{I_0(hkl)}\right\}^{-1} \quad \text{Eq. (3.1)}$$

where I(hkl) are measured intensities, I_0(hkl) is the powder diffraction intensities from JCPDF #01-071-6059, and n is the number of peaks investigated: (111), (200), (220), (311), (331), (420), (422), and (511) were calculated.

The surface and cross-sectional morphologies were evaluated using a scanning electron microscope (SEM, Hitachi High-Tech SU6600). The detailed microtextures were analyzed using inverse pole figure (IPF) maps, and the crystallite size distribution along the growth direction was evaluated from the linear intercepts using electron backscatter diffraction (EBSD; Zeiss Supra35VP, Carl Zeiss). Prior to EBSD measurements, the TiC_xN_{1-x} coating cross sections were fist polished with progressively finer wet abrasive papers, followed by 6 h polishing with Ar^+ beam milling (SM09010; JEOL) with an accelerating voltage of 6 kV.

Coating hardness was measured using an indentation technique (Elionix, ENT-1100a) implemented with a Berkovich shaped diamond tip indenter with 30mNload. Before the hardness measurement, the indented surface area was locally smoothed with a Calotest instrument (CSM Instruments, Switzerland). The indentation hardness was measured at 10 locations over the smoothed surface. Data were analyzed by applying the Oliver–Pharr method [23], and the average value was taken as the coating hardness. The coating adhesion was determined from a scratch test (Revestest, CSM Instruments, Switzerland). A Rockwell C diamond tip with a 120° conical angle and a 200 μm tip radius was used as a scratch indenter. The adhesion strength was defined as the average result of the scratch tests, which were repeated twice at a constant scratching speed of 10mm/min and a loading rate of 100 N/min with the load varying from0 to 100 N.

The friction coefficients of the coatings were measured using a high-temperature tribometer

(CSM Instruments, Switzerland) in the ball-on-disk configuration. The ball-on-disk tests were performed with AISI:52100 and AISI: 316 balls (6 mm φ), a sliding velocity of 25 cm/s, a sliding radius of 5 mm, an applied load of 1 N at room temperature (25°C) and 600°C, 25% humidity, and in ambient air. To suppress the formation of the oxide tribofilm between the contact interface of the ball and friction coatings, the total sliding time was reduced to 1 min, which corresponds to a sliding distance of 15m(approximately 480 laps) [24]. The surface roughness and wear tracks on the coatings were investigated by a 3D laser microscope (VK-8710, KEYENCE) and an electron probe microanalyzer (EPMA), respectively.

3.2.3. Cutting performance

Wear resistance of as-deposited MT-TiC_xN_{1-x} coatings were evaluated using longitudinal continuous turning on alloyed steel (AISI: 4137), carbon steel (AISI: 1055), and stainless steel (AISI: 316). The wear morphology and average width of flank wear (Vb) were observed and measured with an optical microscope. To suppress crater wear and cutting edge deformation due to the lack of an alumina top layer, the criterion for tool lifetime was defined as the maximum cutting distance at an average flank wear (Vb) = 0.10 mm. Furthermore, the failure resistance of TiC_xN_{1-x} coatings was determined by the average number of impacts endured by a tool with a given coating during intermittent turning of four-groove AISI: 4137 for four different cutting edges. To verify the improvement in the failure resistance of the modified coating, TiC_xN_{1-x} with x = 0.69 [18] was chosen as a reference. The cutting conditions are listed in Table 3.2.

Table 3.2 Cutting conditions.

Work material	AISI: 4137	AISI: 1055	AISI: 316	Four-groove AISI: 4137
Tool geometry	CNMG120408-NGU	CNMG120408-NGU	CNMG120408-NGU	CNMG120408-NGU
Edge radius (μm)	45	45	45	45
Rake angle (°)	7	7	7	7
Cutting method	Longitudinal Continuous turning	Longitudinal Continuous turning	Longitudinal Continuous turning	Longitudinal Intermittent turning
Cutting speed (m/min)	150	200	150	300
Feed rate (mm/rev)	0.25	0.25	0.25	0.15
Depth of cut (mm)	2.0	2.0	0.5	1.5
Environment	Wet	Wet	Wet	Wet
Criteria for tool life	Cutting distance at V_b = 0.1	Cutting distance at V_b = 0.1	Cutting distance at V_b = 0.1	Average impact number (N = 4)

3.3. Results

3.3.1. Microstructure analysis

Fig. 3.1 shows semi-quantitative depth profiles of TiC_xN_{1-x} coatings deposited on cemented carbide substrates, as determined by GD-OES. The average chemical composition was calculated from the average C/(C+N) atomic concentration ratios, and the corresponding fraction *x* for the TiC_xN_{1-x} coatings are listed in Table 3.3. The fractions of N and C with respect to Ti are slightly larger than the stoichiometric ratio. Comparison of Fig. 3.1(A) and (B) shows that the carbon content in the modified MT-TiC_xN_{1-x} coating increases due to C_2H_4 addition during CVD, with fraction *x* increasing from 0.45 to 0.63 from the conventional to modified MT-TiC_xN_{1-x} coating.

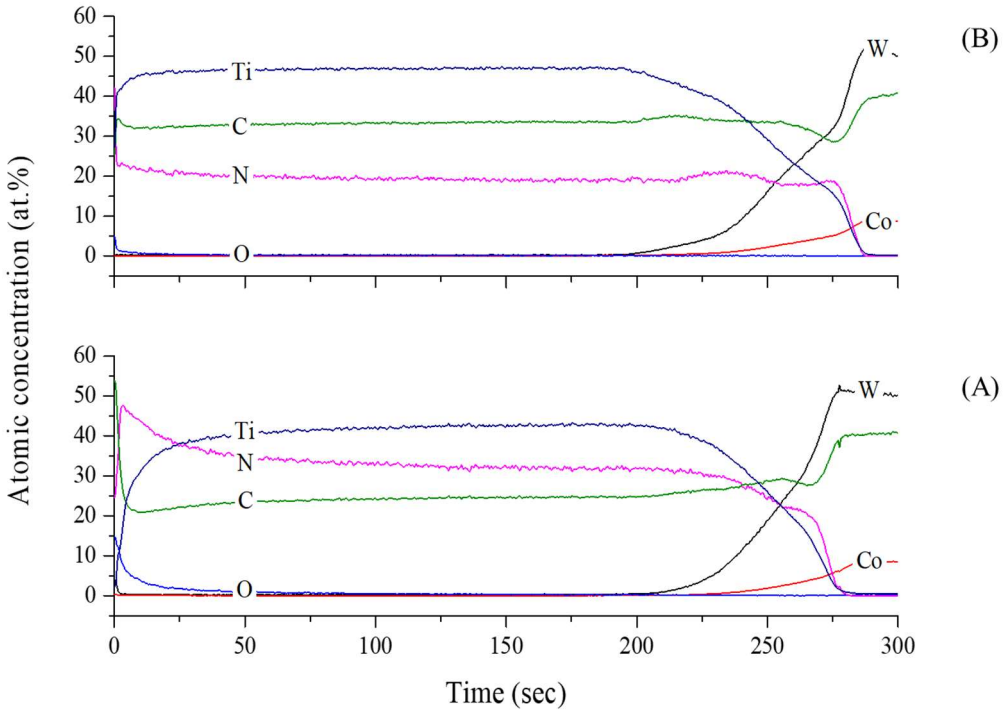

Fig. 3.1. Depth profiles of the chemical compositions of MT-TiC_xN_{1-x} coatings using a glow discharge optical emission spectroscope (GD-OES); (A) Conventional MT-TiC_xN_{1-x} and (B) Modified MT-TiC_xN_{1-x}.

Table 3.3 Semi-quantitative analysis for chemical composition of coatings by GD-OES.

at%	Modified MT-TiC_xN_{1-x} layer	MT-TiC_xN_{1-x} layer
O	0.16 ± 0.05	0.24 ± 0.04
N	19.4 ± 0.28	30.5 ± 0.67
C	33.2 ± 0.15	24.9 ± 0.35
Ti	46.9 ± 0.16	44.0 ± 0.45
Co	0.03 ± 0.01	0.03 ± 0.01
W	0.27 ± 0.03	0.26 ± 0.01
N/Ti	0.41 ± 0.01	0.69 ± 0.02
C/Ti	0.71 ± 0.01	0.57 ± 0.01
Fraction x in TiC_xN_{1-x}	0.63 ± 0.01	0.45 ± 0.01

Fig. 3.2 shows XRD patterns from MT-TiC_xN_{1-x} coatings deposited on cemented carbide substrates at 850°C and 6 kPa. The coating texture coefficients calculated using Eq. (3.1) are listed in Table 3.4. The (311) and (422) peak intensities are slightly high for the

conventional MT-TiC_xN_{1-x} coating [Fig. 3.2(A)], and the texture coefficients were 2.9 and 2.7, respectively. Fig. 3.2(B) shows an XRD pattern from the modified MT-TiC_xN_{1-x} coating, which has a very high (422) peak intensity. The texture coefficient of 6.9 indicates that (422) is the preferred orientation. Furthermore, enlarging the (422) peaks reveals a shift in the angle and a broadening of the peak for the modified MT-TiC_xN_{1-x} coating. The Williamson–Hall analysis revealed negligibly small strain ($\varepsilon < 0.03\%$) for both MT-TiC_xN_{1-x} coatings. The coherently diffracting domain size was calculated as 795 ± 348 and 562 ± 120 Å for the conventional and modified MT-TiC_xN_{1-x} coating, respectively. The residual stress measurement resulted in a tensile stress that slightly increased from 710±37 MPa in the conventional to 840 ± 46 MPa in the modified MT-TiC_xN_{1-x} coating. The lattice constant increases from 4.289 to 4.292 Å, which reflects the increase of *x* from 0.45 to 0.63 in going from the conventional to the modified MT-TiC_xN_{1-x} coating.

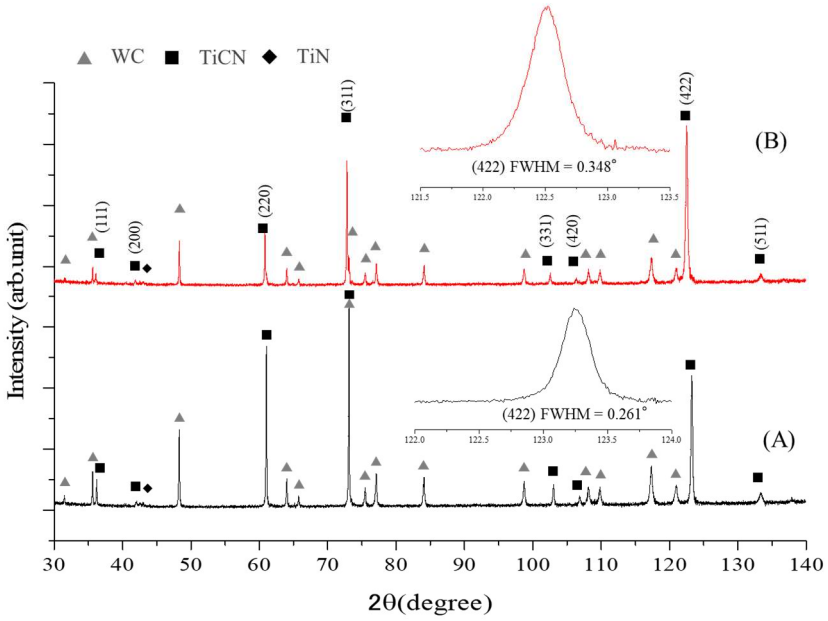

Fig. 3.2. XRD patterns and enlarged views of the (422) diffraction for MT-TiC_xN_{1-x} coatings on carbide substrates; (A) Conventional MT-TiC_xN_{1-x} and (B) Modified MT-TiC_xN_{1-x}.

Table 3.4 Texture coefficients for measured coatings.

	TC (111)	TC (200)	TC (220)	TC (311)	TC (331)	TC (420)	TC (422)	TC (511)
Modified MT-TiC_xN_{1-x}	0.2	0.0	0.1	0.6	0.1	0.0	6.9	0.0
MT-TiC_xN_{1-x}	0.1	0.0	1.2	2.9	0.8	0.1	2.7	0.1

Fig. 3.3 presents SEM images of the surfaces and cross sections of the TiC_xN_{1-x} coatings. The MT-TiC_xN_{1-x} coating prepared by conventional MT-CVD [Fig. 3.3(A)] has a coarse grain and a rough surface. The columnar crystallite sizes increase with increasing thickness. However, doping the MT-CVD process with C_2H_4 gas results in a remarkable decrease in crystallite size and surface roughness, resulting in equalization of the columnar grain morphology seen in Fig. 3.3(B).

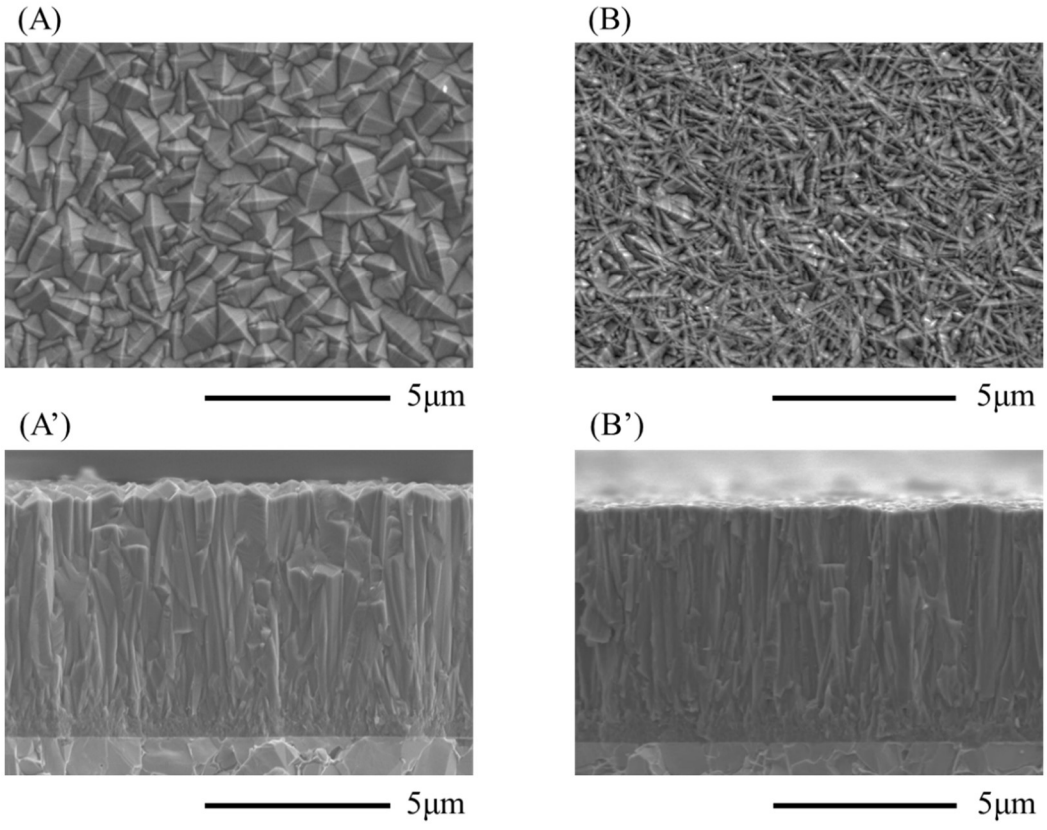

Fig. 3.3. SEM images of the surface and cross sections of MT-TiC_xN_{1-x} coatings on carbide substrates; (A) Conventional MT-TiC_xN_{1-x} and (B) Modified MT-TiC_xN_{1-x}.

Fig. 3.4 shows the detailed grain microtexture and size distribution for the TiC_xN_{1-x} coatings obtained from EBSD. The IPF map in the normal direction of the TiC_xN_{1-x} coatings shows that the growth direction is horizontal (i.e., in the plane of the figure). The dominance of purple and pink colors in Fig. 3.4 indicates that the (422) plane is aligned along the growth direction. The crystallite in the modified MT-TiC_xN_{1-x} coating [Fig. 3.4(B)] revealed as by the IPF map (containing many twin boundaries) is very dense and the aspect ratio is greater than that of the conventional MT-TiC_xN_{1-x} coating [Fig. 3.4(A)]. The TiC_xN_{1-x} crystallite size distributions evaluated from the linear intercept obtained by EBSD show a sharper distribution in the modified MT-TiC_xN_{1-x} coating, indicating a maximum crystallite size of <0.5 μm, with crystallite 0.2 μm or less accounting for 70% of the crystallite. The conventional MT-TiC_xN_{1-x} coating has a broader crystallite size distribution and the maximum crystallite size is 0.9 μm. The average crystallite size is calculated to be 0.17 ± 0.06 and 0.25 ± 0.15 μm for the modified and conventional MT-TiC_xN_{1-x} coatings, respectively.

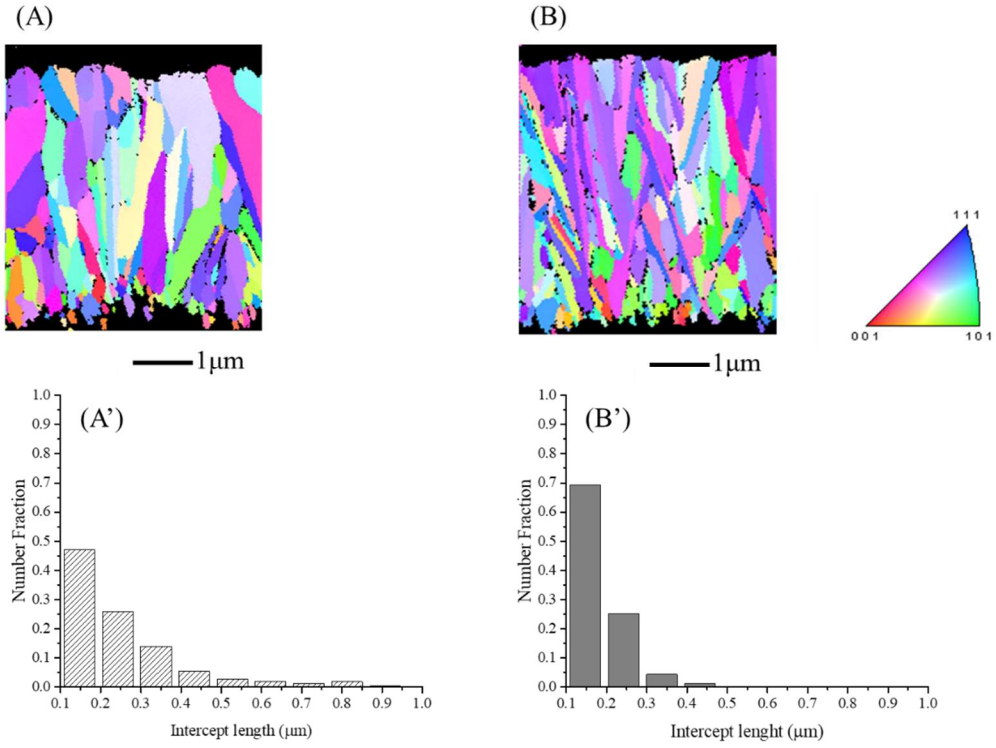

Fig. 3.4. Electron backscatter diffraction orientation map of a normal section of MT-TiC_xN_{1-x} coatings and grain size distribution; (A) Conventional MT-TiC_xN_{1-x} and (B) Modified MT-TiC_xN_{1-x}.

3.3.2. Mechanical properties

The average hardness for modified and conventional MT-TiC_xN_{1-x} coatings, as measured by the nano-indentation technique, is 33.1 ± 1.25 and 31.4 ± 3.05 GPa, respectively. Using the scratch technique, the coatings are found to have good adhesion strength of 44.5 ± 0.7 and 39.5 ± 6.4 N for modified and conventional TiC_xN_{1-x} coatings, respectively. The spatial distribution in hardness and adhesion strength for the modified MT-TiC_xN_{1-x} coating is small because of the fine, homogeneous structure of the grain.

Fig. 3.5 shows the friction coefficient obtained by the pin-on-disk test at room temperature and 600 °C for the MT-TiC_xN_{1-x} coatings when used on AISI: 52100 (Fig. 3.5.1) and AISI: 316 (Fig. 3.5.2). The friction coefficients decrease at elevated temperature for both types of MT-TiC_xN_{1-x} coatings and are independent of the ball material. The friction coefficient decreases from 0.71 ± 0.07 for the conventional MT-TiC_xN_{1-x} coating to 0.57 ± 0.04 for the modified MT-TiC_xN_{1-x} coating when used on AISI: 52100 and decreases from 0.75 ± 0.12 to 0.58 ± 0.09 when used on AISI: 316 at room temperature, which reveals the effect of surface roughness of 107 ± 6 and 67 ± 12 nm for the conventional and modified MT-TiC_xN_{1-x} coatings, respectively. At 600°C, the decrease in friction coefficient is quite significant, which results from TiO_x ($x \approx 2$) formation (Table 3.5). The modified (conventional) MT-TiC_xN_{1-x} coating has a friction coefficient of 0.36 ± 0.04 (0.62 ± 0.03) when used on AISI: 52100 and 0.40 ± 0.05 (0.52 ± 0.03) when used on AISI: 316.

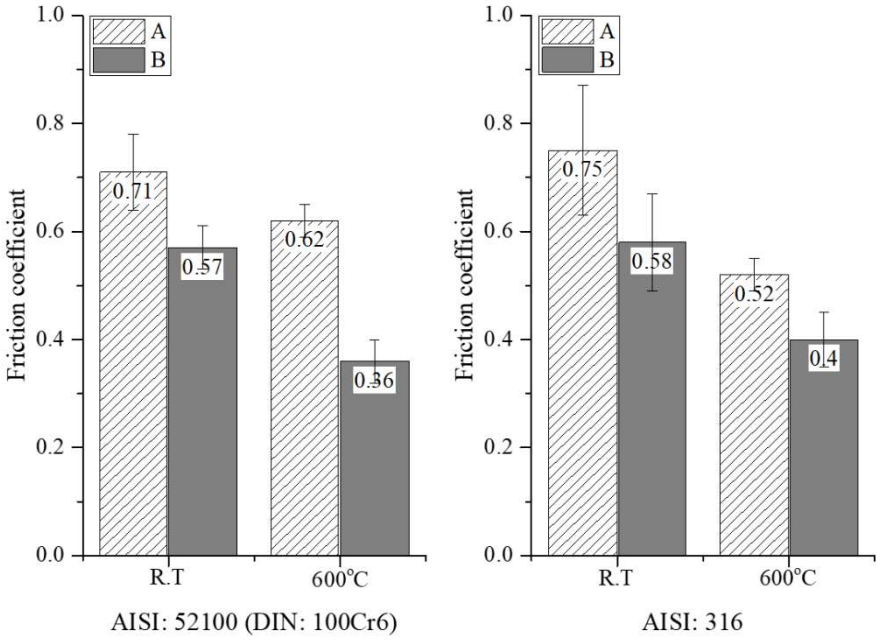

Fig. 3.5. Room and elevated tribological properties of MT-TiC$_x$N$_{1-x}$ coatings by pin-on-disk test sliding against (1) AISI: 52100 and (2) AISI: 316; (A) Conventional MT-TiC$_x$N$_{1-x}$ and (B) Modified MT-TiC$_x$N$_{1-x}$.

Table 3.5. Chemical composition analysis on the surface of wear tracks at the elevated tribological test

Area	Coating	Ball	Chemical composition (at.%)						
			C	N	O	Ti	Cr	Fe	Ni
A_{S1}	Conventional MT-TiCxN1-x	AISI: 52100 (DIN: 100Cr6)	0.0	0.0	71.7	26.6	0.0	1.7	0.0
B_{S1}	Modified MT-TiCxN1-x		3.4	0.0	64.2	32.3	0.0	0.1	0.0
A_{S2}	Conventional MT-TiCxN1-x	AISI: 316	3.4	0.0	63.9	31.9	0.3	0.4	0.2
B_{S2}	Modified MT-TiCxN1-x		3.3	0.3	62.8	33.4	0.0	0.2	0.0

Figs. 3.6.1 and 3.6.2 show SEM images of wear tracks on the surface of the MT-TiC$_x$N$_{1-x}$ coating after the 600°C pin-on-disk test with AISI:52100 and AISI: 316, respectively. The white arrows on the SEM images indicate the sliding direction. Significant destruction [Fig.

3.6.1(A)] and plastic deformations [Fig. 3.6.2(A)] occurred on the grain surface of the conventional MT-TiC_xN_{1-x} coating. However, a trace amount of microexfoliation and clean wear tracks appear on the surface of the modified MT-TiC_xN_{1-x} coating during sliding on AISI: 52100 [Fig. 3.6.1(B)] and AISI: 316 [Fig. 3.6.2(B)]. These results indicate that the modified MT-TiC_xN_{1-x} coating with its finer grain structure is superior in terms of resistance to deformation at elevated temperatures. Table 3.5 summarizes the results of the surface-area EPMA analysis of the wear tracks of the coatings and of the ball material trace amounts of the ball material; however, no statistically significant difference occurs between the two MT-TiC_xN_{1-x} coatings. These results indicate that the decrease in friction coefficient is strongly influenced by the more refined microstructure in the modified MT-TiC_xN_{1-x} coating. Table 3.6 summarizes the measured physical properties of the modified and conventional MT-TiC_xN_{1-x} coatings.

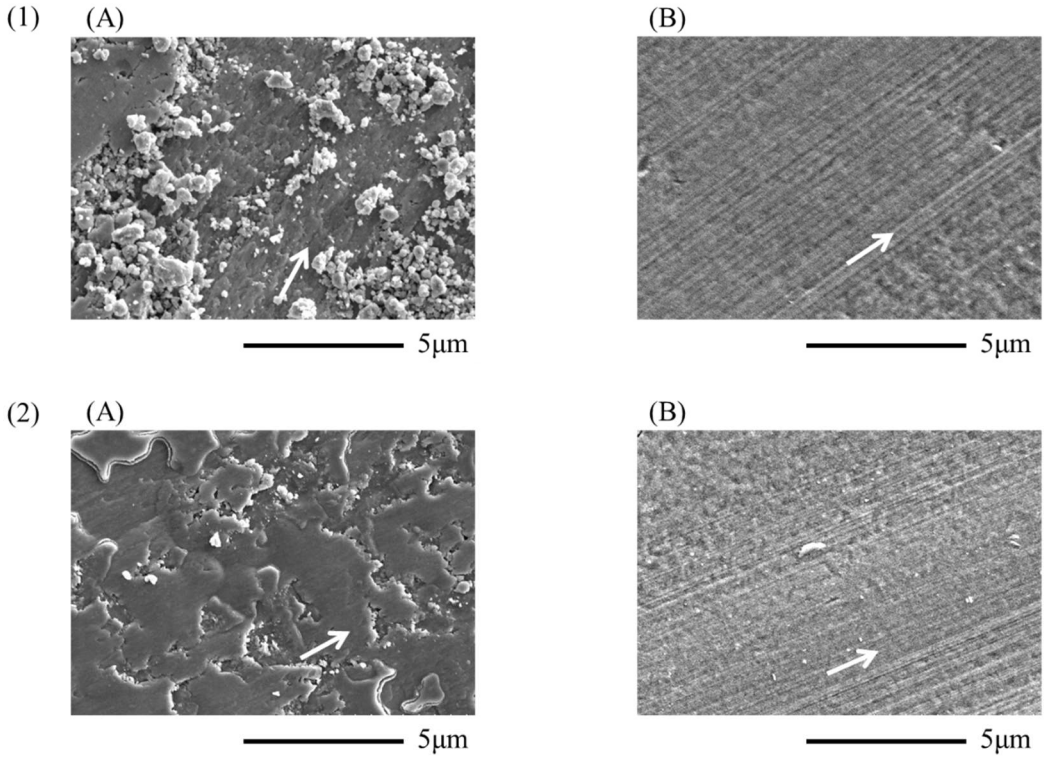

Fig. 3.6. SEM image of the sliding surface MT-TiC_xN_{1-x} coatings at the elevated tribological test against (1) AISI: 52100, (2) AISI: 316; (A) Conventional MT-TiC_xN_{1-x} and (B) Modified MT-TiC_xN_{1-x}.

Table 3.6.Physical properties of coatings.

	Modified MT-TiC_xN_{1-x} layer	MT-TiC_xN_{1-x} layer
Lattice constant (Å)	4.292 ± 0.001	4.289 ± 0.001
Crystallite size (µm)	0.17 ± 0.06	0.25 ± 0.15
Residual stress (MPa)	840 ±46	710 ±37
Hardness (GPa)	33.1 ± 1.25	31.4 ± 3.05
Friction coefficient to AISI: 52100 (DIN: 100Cr6)		
Room temperature	0.57±0.04	0.71±0.07
600 (°C)	0.36±0.04	0.62±0.03
Friction coefficient to AISI: 316 (N)		
Room temperature	0.58±0.09	0.75±0.12
600 (°C)	0.40±0.05	0.52±0.03
Coating adhesion (N)	44.5 ± 0.7	39.5 ± 6.4

3.3.3. Cutting performance

Fig. 3.7 shows the cutting results for as-deposited MT-TiC_xN_{1-x} coatings. The wear resistance of the coatings is defined as the maximum cutting distance for an average flank wear (Vb) of 0.10 mm. The wear resistance was evaluated by longitudinal continuous turning of carbon steel AISI: 1055 (Fig. 3.7.1), alloyed steel AISI: 4137 (Fig. 3.7.2), and stainless steel AISI: 316 (Fig. 3.7.3). The cutting distance increases by approximately 30% for AISI: 1055 and AISI: 4137 and remarkably by 60% for AISI: 316. The failure resistance of the modified MT-TiC_xN_{1-x} coating, as determined by the average number of impacts when used for intermittent turning of four-groove AISI: 4137, gives 4073 impacts, an improvement of approximately 30% compared with the conventional MT-TiC_xN_{1-x} coating (3101 impacts (Fig. 3.7.4)) and 50% compared with the MT-$TiC_{0.69}N_{0.31}$ reference sample (2771 impacts) [18].

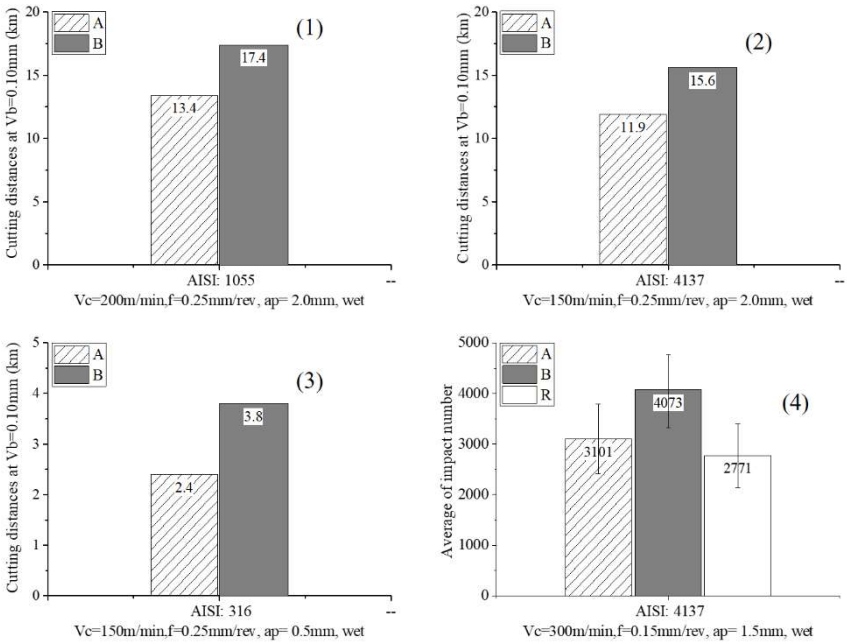

Fig. 3.7. Cutting performance of the as-deposited MT-TiC_xN_{1-x} coatings by continuous turning of (1) AISI: 1055, (2) AISI: 3147, and (3) AISI: 316 and intermittent turning of a four grooved AISI: 4137; (A) Conventional MT-TiC_xN_{1-x}, (B) Modified MT-TiC_xN_{1-x} and (R) MT-$TiC_{0.69}N_{0.31}N$.

3.4. Discussion

3.4.1. Mechanical properties

This study demonstrates a MT-TiC_xN_{1-x} coating with a very fine grain structure, improved hardness, surface roughness, superior tribological properties, and good adhesion strength to cemented carbide substrates. This coating was fabricated by introducing C_2H_4 to the $TiCl_4$–CH_3CN–H_2 precursor system in the low-pressure CVD process. The improvement in adhesion strength compared with the previous work [18] is attributed to the increase in deposition temperature at the TiN base layer, which enhances the chemical diffusion of W and Co from the substrate (Fig. 3.1 and Table 3.3) and optimizes fraction *x* in the modified MT-TiC_xN_{1-x} coating. Akiyama et al. [25] reported that the high temperature deposition of the TiN base coating layer can enhance the adhesion of the TiC_xN_{1-x} coating due to the diffusion of W and Co from the cemented carbide substrate. Increasing of the *x* value in MT-TiC_xN_{1-x}

coating refines the microstructure, which improves the hardness but decreases the adhesion to carbide substrates because of the formation of a discontinuous bonding interphase when $x \geq 0.65$ [18]. Therefore, the maximum fraction x that allows both the fine grain structure and adhesion strength to be maintained is 0.65. Because of the different microstructure and mechanical properties of the modified and conventional MT-TiC_xN_{1-x} coatings, accurately determining the increment in adhesion strength by the scratch test is difficult, so a better measurement technique [26] is required.

The increase in carbon content in modified MT-$TiC_{0.63}N_{0.37}$ results in a more refined grain structure with more twining boundaries and facetted morphology, as observed in Fig. 3.3, which shows modified MT-TiC_xN_{1-x} [with highly preferred orientation in the (422) plane (Figs. 3.2 and 3.4 and Table 3.4)]. The microstructure and preferred orientation of the deposited MT-TiC_xN_{1-x} coating affects by coating temperature and partial pressure. Deposition temperature of around 850°C with a relatively high $TiCl_4/CH_3CN$ volume ratio in the precursor system exhibits facetted grain with (422) preferred orientation [22], whereas a high deposition temperature results in equiaxied grain with (220) preferred orientation [16].Larsson and Ruppi [22] used the growth model to investigate Ti(C,N) coated by MT-CVD. They suggested that the predominant adhesion of polar reaction products (CN−) to highly polar {111} surfaces promotes fast growth of nonpolar {200}, which results in the (422) preferred orientation and facetted grain morphology. The situation is assumed to be similar to the constitution of π-conjugated bond in C_2H_4 and results in the increase of the incorporated carbon content x in the MT-TiC_xN_{1-x} coating, increasing the growth rate of {200}, which results in a greater preference for (422) orientation. Furthermore, the incorporated carbon is considered to affect the strain in crystallite growth; thus, higher twining boundaries in the dense and fine facetted columnar grain structures are observed (Fig. 3.4(B). The aforementioned MT-TiC_xN_{1-x} coatings are fabricated according to the following reactions.

$$4TiCl_4(g) + 2CH_3CN(g) + 9H_2(g) \rightarrow 2TiC(s) + 2TiN(s) + 16HCl(g) \quad Eq.(3.2.1)$$

$$2TiCl_4(g) + 2C_2H_4(g) + 2H_2(g) \rightarrow 2TiC(s) + 8HCl(g) \quad Eq.(3.2.2)$$

$$6TiCl_4(g) + 2CH_3CN(g) + C_2H_4(g) + 11H_2(g) \rightarrow 6TiC_xN_y(s) + 2CH_4(g) + 24HCl(g) \quad Eq.(3.2)$$

Eqs. (3.2.1) and (3.2.2) are considered to be substantially simultaneous as a result of Eq. (3.2). TiC(s) and TiN(s) form a continuous series that is completely soluble under equilibrium conditions. In this study, the x value is calculated to be 0.45 and 0.63 for the conventional and modified MT-TiC_xN_{1-x} coatings, respectively. Increase in the incorporated carbon content in the modified MT-TiC_xN_{1-x} and tensile residual stress result in a peak shift (Fig. 3.2). An increase in the residual tensile stress in modified the MT-TiC_xN_{1-x} coating is estimated from the increase of defects caused by the incorporated carbon, which promotes greater twining and decreases the crystallite size [27], as observed in Fig. 3.4(B), and the broadening of the full width at half maximum in Fig. 3.2(B). The effect of crystallite size and microstrain on full width at half maximum, as evaluated by the Williamson–Hall analysis, indicated that main effect is crystallite size refinement, which is inevitable in CVD coating [15].

The increase in indentation hardness in the modified MT-TiC_xN_{1-x} coating compared with that in the conventional coating is attributed to the increase in defects due to the increased incorporated carbon content and consequent crystallite size refinement with higher twining boundaries. This also leads to a decrease in surface roughness and improves the resistance to deformation at elevated temperatures. The decrement of surface roughness is considered to improve the tribological properties of the modified MT-TiC_xN_{1-x} coating both at room temperature and at elevated temperature (Fig. 3.5). The decrease in friction coefficient for both MT-TiC_xN_{1-x} coatings at elevated temperature (Fig. 3.5 and Table 3.6) is attributed to the formation of TiO_x ($x \approx 2$) [28]. Furthermore, because no prominent change appears in the chemical composition of ball materials on the wear track (Table 3.5), the chemical composition of the MT-TiC_xN_{1-x} coating is considered to have a negligible effect on the friction coefficient.

3.4.2. Cutting performance

The wear properties of tools used to cut metal is influenced by the working material and the cutting conditions. Tool wear as a function of cutting temperature may be divided into abrasive, cohesive, and diffusion wear [29]. Diffusion wear, including interdiffusion of chemical components and oxidation of the coating resulting from crater wear, is caused by

high temperatures and pressures during high-speed and high-feed-rate cutting operations. It can be hindered by introducing a state-of-the-art Al_2O_3 [30] layer deposited over the TiC_xN_{1-x} coating and by optional post-treatment [31–33], both of which are widely used in industrial applications.

This study focuses on improving the overall cutting performance with MT-CVD coatings by improving the abrasive and cohesive wear resistance of as-deposited MT-TiC_xN_{1-x} coatings. Reducing the crystallite size by grain-boundary engineering is an attractive technique to increase the abrasive wear of the hard coating. This effect is due to not only the Hall–Pecth relationship but also other mechanisms associated with the grain boundary effect, such as dislocation movement, strain hardening, or crack resistance [34]. The modified MT-TiC_xN_{1-x} coating having a fine grain structure with a high twinning boundary (Fig. 3.4) and increased hardness is therefore expected to outperform the conventional MT-TiC_xN_{1-x} coating; this has led to the increased cutting distance from AISI: 1055 (Fig. 3.7.1) to AISI: 4137 (Fig. 3.7.2) when using the modified MT-TiC_xN_{1-x} coating.

Cohesive wear when cutting stainless steel is caused by the build-up at the edge of accelerated exfoliates of the coating. The effect should be reduced by reducing the friction coefficient between work material and coating. The increment in cutting distance of up to 60% (Fig. 3.7.3) obtained with the modified MT-TiC_xN_{1-x} coating with respect to the conventional MT-TiC_xN_{1-x} coating can be explained by the smooth surface morphology (Fig. 3.3), lower friction coefficient (Fig. 3.5), and resistance to plastic deformation at elevated temperatures (Fig. 3.6).

Finally, the failure mechanism in four-groove intermittent cutting of AISI: 4137 is considered to be constant stress fatigue. Damage accumulated in the coatings by repeated impact results in fatigue, as determined by the hysteresis area in the stress–strain curves. The size of this area is supposed to be inversely proportional to the strength or hardness of the material, and hardness increases with decreasing crystallite size [35]. Therefore, an average increase in the number of impacts by up to 30% for the modified MT-TiC_xN_{1-x} coating is considered to result from the refinement in grain structure (Fig. 3.4).

3.5. Summary

By introducing C_2H_4 gas to the $TiCl_4$–CH_3CN–H_2 precursor system on a TiN base layer during moderate temperature low-pressure CVD, a modified MT-$TiC_{0.63}N$ coating that adheres well to carbide substrates was developed. The microstructure, mechanical properties, and cutting performance were evaluated by comparing with a conventional MT-TiC_xN_{1-x} coating. GD-OES and XRD analyses reveal an increase in incorporated carbon, and EBSD reveals a highly preferred orientation of (422) columnar grains with a very narrow crystallite size distribution. This grain refinement not only increases the indentation hardness and the resistance to plastic deformation but also reduces the friction coefficient of the modified MT-TiC_xN_{1-x} coating when used to cut AISI:52100 and AISI: 316 both at room temperature and 600°C.

The wear resistance of the modified MT-TiC_xN_{1-x} coating was determined by continuous cutting of AISI: 1055, AISI: 4137, and AISI: 316. The results reveal an increase in cutting distance of up to 30%–60% compared with the conventional MT-TiC_xN_{1-x} coating. The failure resistance of the modified MT-TiC_xN_{1-x} coating was determined by applying it to four-groove intermittent cutting of AISI: 4137. The results indicate an increase by up to 30% in the average number of impacts.

Overall, the mechanical properties of the modified MT-TiC_xN_{1-x} coating deposited via the $TiCl_4$–CH_3CN–C_2H_4–H_2 precursor system in low-pressure CVD contribute to improving the cutting performance of metal cutting machine tools used in the industry.

References in chapter 3

[1] H.G. Prengel,W.R. Pfouts, A.T. Santhanam, Surf. Coat. Technol. 102 (1998) 183–190.

[2] D.T. Quinto, Int. J. Refract. Met. Hard Mater. 14 (1996) 7–20.

[3] G. Wakefield, C. Yaws, J. Bloom, Proc. 4th Int. Conf. on Chemical Vapour Deposition, Princeton, USA (1973) pp. 577–583.

[4] S. Eroglu, B. Gallois, Surf. Coat. Technol. 49 (1991) 275–278.

[5] W. Schintlmeister, O. Pacher,Metal 28 (1974) 690–695.

[6] D.J. Cheng,W.P. Sun,M.H. Hon, Thin Solid Films 146 (1987) 45–53.

[7] V. Sarin, J. Lindstrom, J. Electrochem. Soc. 126 (1979) 1281–1287.

[8] J. Skogsmo, H. Norden, Int. J. Refract. Met. Hard Mater. 11 (1992) 49–61.

[9] S. Vuorinen, R. Hoel, Thin Solid Films 232 (1993) 73–82.

[10] M. Bonetti-Lang, R. Bonetti, H.E. Hintermann, D. Lormann, Proc. 8th Int. Conf. on Chemical Vapour Deposition, Princeton, USA (1981) pp. 606–616.

[11] R.S. Bonetti, H.Wiprächtiger, E. Mohn, Met. Powder Rep. 45 (1990) 837–840.

[12] S. Ruppi, J. Phys. IV 11 (2001) Pr3-847–Pr843-859.

[13] S. Kudapa, K. Narasimhan, P. Boppana, W.C. Russell, Surf. Coat. Technol. 120–121 (1999) 259–264.

[14] H. Holzschuh, Int. J. Refract. Met. Hard Mater. 20 (2002) 143–149.

[15] S. Ruppi, A. Larsson, J. Vac. Sci. Technol., A 21 (2003) 66–75.

[16] C. Czettl, C. Mitterer, U. Mühle, D. Rafaja, S. Puchner, H. Hutter, M. Penoy, C. Michotte, M. Kathrein, Surf. Coat. Technol. 206 (2011) 1691–1697.

[17] J. Watanabe, Y. Sone, US Patent No. US7906230 (2011).

[18] A. Paseuth, H. Fukui, S. Okuno, H. Kanaoka, Y. Okada, Surf. Coat. Technol. 260 (2014) 139–147.

[19] H. Toraya, Rigaku J. 6 (1989) 28–34.

[20] G.K. Williamson,W.H. Hall, Acta Metall. 1 (1953) 22–31.

[21] E.J. Mittemeijer, U. Welzel, Z. Krist. 223 (2008) 552–560.

[22] A. Larsson, S. Ruppi, Thin Solid Films 402 (2002) 203–210.

[23] W.C. Oliver, G.M. Pharr, J. Mater. Res. 19 (2004) 3–20.

[24] S. Imamura, H. Fukui, A. Shibata, N. Omori, M. Setoyama, Surf. Coat. Technol. 202

(2007) 820–825.

[25] K. Akiyama, E. Nakamura, I. Suzuki, T. Oshika, A. Nishiyama, Y. Sawada, Surf. Coat. Technol. 94–95 (1997) 328–332.

[26] K.D. Bouzakis, A. Asimakopoulos, G. Skordaris, E. Pavlidou, G. Erkens, Wear 262 (2007) 1471–1478.

[27] E. Chason, Thin Solid Films 526 (2012) 1–14.

[28] M. Bao, X. Xu, H. Zhang, X. Liu, L. Tian, Z. Zeng, Y. Song, Thin Solid Films 520 (2011) 833–836.

[29] A.E. Focke, F.E. Westermann, J. Kemphaus, W.T. Shih, M. Hoch, Wear 46 (1978) 65–79.

[30] S. Ruppi, Surf. Coat. Technol. 202 (2008) 4257–4269.

[31] M. Klaus, C. Genzel, H. Holzschuh, Thin Solid Films 517 (2008) 1172–1176.

[32] K.D. Bouzakis, G. Skordaris, E. Bouzakis, A. Tsouknidas, S. Makrimallakis, S. Gerardis, G. Katirtzoglou, CIRP Ann. Manuf. Technol. 60 (2011) 587–590.

[33] K.D. Bouzakis, N. Michailidis, G. Skordaris, E. Bouzakis, D. Biermann, R. M'Saoubi, CIRP Ann.Manuf. Technol. 61 (2012) 703–723.

[34] S. Ruppi, US Patent No. US7927663 (2011).

[35] P.H. Mayrhofer, C. Mitterer, L. Hultman, H. Clemens, Prog. Mater. Sci. 51 (2006) 1032–1114.

Chapter 4. Deposition and analysis of Al-Rich c-$Al_xTi_{1-x}N$ coating with preferred orientation

4.1. Introduction

Further enhancement of the performance of state-of-the-art coated tools used in the metal cutting industry is required for dry cutting and to achieve higher cutting speeds to meet the demands for lower cost and environmental impact reduction. Metastable cubic (c-) $Al_xT_{1-x}N$ coatings fabricated via physical vapour deposition (PVD) [1] are well established in the tools industry due to their high oxidation resistance compared to TiN [2–4] and their age hardening effect during metal cutting [5]. Efforts to improve the thermal properties of c-$Al_xT_{1-x}N$ coatings include increasing the Al content [6, 7], alloying with Cr [8], Zr [9], Ta [10], and Y [8, 11], and modulating the multilayer structure, leading to increased hardness and toughness (eg, TiN/AlN [12], TiAlN/AlTiN [13], and so on). For cutting tool applications, c-$Al_xT_{1-x}N$ prepared by PVD methods is metastable at a composition of approximately $x < 0.67$, whereas higher x values generate a mixture of cubic and hexagonal phases [14, 15], which deteriorates the mechanical properties [16].

c-$Al_xT_{1-x}N$ [17] coating with a considerably high Al content of $x > 0.7$ has been successfully deposited on the laboratory scale via low-pressure chemical vapour deposition (LP-CVD) by using highly chemically reactive NH_3 gas and the $TiCl_4$–$AlCl_3$–H_2 precursor system. Recently, coatings of single-phase c-$Al_xT_{1-x}N$ (x=0.8) [18,19] and a mixture of hexagonal and cubic phase $Al_xT_{1-x}N$ (x = 0.95) [20, 21] with a self-organized nanolamellae microstructure were synthesized. Deposition of single cubic phase c-$Al_xT_{1-x}N$ with a higher aluminum content on the industrial scale via LPCVD has received increasing attention.

We previously reported modification in the mechanical properties and cutting performance of a TiC_xN_{1-x} coating on cutting tools by moderate-temperature chemical vapour deposition [22, 23]. Recently, we disclosed a method of forming cubic TiN and hexagonal AlN (c-TiN/h-AlN) nanolamellae [24] and c-Ti(Al)N/c-Al(Ti)N nanolamellae [25] using an industrial-scale CVD reactor. The mechanical properties of hard coatings are affected by the microstructure, and one key approach is to control the preferred orientation in the coatings. Ruppi suggested that the service life of an α-Al_2O_3 coating with (001)-preferred orientation was twofold higher

than that of the congener with random orientation [26]. Thus, controlling the preferred orientations in c-$Al_xT_{1-x}N$ coatings and clarifying the mechanical properties of these coatings can facilitate delineation of the guidelines for developing high-performance tools. However, there are few or even no published reports on crystal orientation-controlled Al-rich single-phase c-$Al_xT_{1-x}N$ coatings deposited via LP-CVD.

This study describes an Al-rich single-phase c-$Al_xT_{1-x}N$ coating with preferred crystal orientation. c-$Al_xT_{1-x}N$ coatings with (100)- and (111)-preferred orientations were fabricated via industrial-plant LP-CVD using an $AlCl_3$–$TiCl_4$–NH_3–Ar–H_2 precursor system. The microstructure and chemical composition of (100)- and (111)-oriented c-$Al_xT_{1-x}N$ (with average *x* values of 0.82 and 0.73, respectively) were evaluated using electron microscopy. These species comprised c-Al(Ti)N/c-Ti(Al)N nanolamellae with average compositions of c-$Al_{0.9}Ti_{0.1}N$/c-$Al_{0.6}Ti_{0.4}N$ and c-$Al_{0.80}Ti_{0.20}N$/c-$Al_{0.50}Ti_{0.50}N$ and average lamellar periods of 7.7 and 4.5 nm, respectively. The phase stability at high temperature (RT to 1000°C) was investigated, revealing stability even at 1000°C. The mechanical properties of c-$Al_xT_{1-x}N$ coatings fabricated via LP-CVD were investigated and compared with those of commercially available arc-evaporated c-$Al_xT_{1-x}N$ (x = 0.6).

4.2. Experimental procedures

4.2.1. Coating deposition

Single-phase c-$Al_xT_{1-x}N$ (x=0.82 and 0.73) coatings with (100)- and (111)-preferred orientations were deposited using a commercially available hot-wall low-pressure CVD system (reactor scale: 1450 mm height x 450 mm diameter; full-loaded capacity=10.000 pieces of SNMA120408 type inserts) by using an $AlCl_3$–$TiCl_4$–NH_3–Ar–H_2 precursor system. $AlCl_3$ was generated by the reaction between HCl gas and aluminum chips (purity: 99.99%). $TiCl_4$ vapour was provided by feeding $TiCl_4$ (purity: 99.9%) liquid through a vaporizer. Metal chlorides and NH_3 gas were introduced into the CVD reactor via separate gas inlets to avoid complex formation, and finally mixed by rotating the gas feeding pipe in the CVD reactor based on a patent published by Paseuth et al [24, 25]. The deposition parameters are listed in Table 1. WC-5wt%Co substrates (SNMA120408; Sumitomo Electric Hardmetal Corp., Hyogo, Japan) with mirror-polished surfaces were used for physical property evaluations.

Samples were centrally loaded in the batch on the half-radius positions of the tray, as described in related work [22,23]. A 0.5-μm-thick TiN base layer and a 2.0-μm-thick TiC_xN_{1-x} bonding layer were deposited to guarantee adhesion between the coatings and carbide substrate, and an approximately 2.5-μm-thick c-$Al_xT_{1-x}N$ coating was then deposited. Precoating tests were conducted to verify a proper deposition rate of the c-$Al_xT_{1-x}N$ coatings, and the coating thickness was adjusted by varying the deposition time.

4.2.2. Coating characterization

The surface and cross-sectional morphologies of the (100)-and (111)-oriented c-$Al_xT_{1-x}N$ coatings were evaluated via scanning electron microscopy (SEM; Hitachi High-Tech SU6600, Tokyo, Japan). The detailed microtextures were analyzed by using electron backscatter diffraction (EBSD; Zeiss Supra35VP, Carl Zeiss, Jena, Germany). The distribution of crystal orientations along the growth direction of the coating was evaluated using inverse pole figure (IPF) analysis, and the degree of preferred orientation was quantified by the multiples of random distributions (MRD) value. The MRD values were defined as a comparison of the actual distribution with the distribution expected for the case when the orientations are completely random (MRD=1); thus, the degree of preferred orientation is indexed by a multiple of the MRD [27]. Before electron backscatter diffraction (EBSD) measurements, the cross-section of the c-$Al_xTi_{1-x}N$ coatings was polished with progressively finer wet abrasive papers, followed by 6 h polishing via Ar^+ beam milling (SM09010; JEOL; accelerating voltage: 6 kV).

The nanostructure and chemical composition of the c-$Al_xTi_{1-x}N$ coatings were evaluated via transmission electron microscopy (TEM; JEM-2100F; JEOL) with energy dispersive X-ray (EDX; JED-2300; JEOL). The *x* value for the c-$Al_xTi_{1-x}N$ coatings was determined as the average of the Al/(Al+Ti) atomic ratio for 40 points along the thickness direction. TEM samples were prepared by using a focused ion beam (FIB; JIB-4501; JEOL) with Ga^+ beam milling (accelerating voltage: 30 kV).

Structural and thermal stability analyses were conducted at room temperature (RT) and at 400–1000°C in steps of 100°C, using in-situ high-temperature X-ray diffraction (HT-XRD; RIGAKU, SmartLab; 45 kV, 200 mA, Cu-Kα radiation) with a high-temperature apparatus

(Aton-Parr DSH1100; Aton-Parr GmbH, Austria). Samples were heated (10°C/min) under vacuum (holding time: 30 min) before every measurement. XRD measurements were performed in grazing incidence geometry (incidence angle: 2°); the X-ray penetration depth ($\tau_{1/e}$) was approximated as 2.3 µm as follows:

$$\tau_{1/e} = \frac{sin\alpha}{\mu} \quad Eq.(4.1)$$

where, $\tau_{1/e}$ is the penetration depth (µm) assuming that the X-ray beam intensity is attenuated to 1/*e* (36.7%) of its initial value, α = 2° is the angle of incidence, and µ (calculated as 0.0155 μm^{-1}) is the linear absorption coefficient of c-AlN [28] for Cu-Kα radiation. The thermal stability of the c-$Al_xTi_{1-x}N$ coatings was compared with that of a commercially available arc-evaporated 5 µm thick $Al_xTi_{1-x}N$-coated cement carbide substrate (Sumitomo Electric Hardmetal Corp., AC510U).

The residual stress of the c-$Al_xTi_{1-x}N$ coatings in the as-deposited state was determined by the $sin^2\psi$ method, assuming a bi-axial stress state as follows:

$$\sigma = -\frac{E}{2(1+\nu)} cot\theta_0 \frac{\pi}{180} \frac{\delta(2\theta)}{\delta(sin^2\psi)} \quad Eq.(4.2)$$

here, $\delta(2\theta)/\delta(sin^2\psi)$ is the gradient of the $2\theta - sin^2\psi$ plot , E is Young's modulus, v is the Poisson ratio, θ_0 is the standard Bragg angle, and ψ is the angle between the diffracting lattice plane and the sample surface. The values of E and v applied in this study are E_{200} = 386 GPa, v_{200} = 0.25, and E_{111} = 489GPa, v_{111} = 0.18 according to stress measurement using the (200) and (111) peaks of the (100) and (111) oriented c-$Al_xTi_{1-x}N$ coatings, respectively [29]. The stress-free lattice parameters were analytically determined using the $2\theta - sin^2\psi$ plot [30] as follows:

$$sin^2\psi_0 = \frac{2C_{11} + 4C_{12} - 4C_{44}}{3(C_{11} + 2C_{12})} \quad Eq.(4.3)$$

where, ψ_0 is the angle between the diffracting stress-free lattice plane $d_0(hkl)$; C_{11}, C_{12}, and C_{44} are compositionally-dependent values of the elastic constants of $Al_xTi_{1-x}N$ obtained by first principles calculation [31].

The hardness of the as-deposited c-$Al_xTi_{1-x}N$ coatings was measured using a nano-indentation tester (Elionix; ENT-1100a), and implemented with a Berkovich-shaped diamond tip indenter. The indentation test was performed at 10 locations over the smoothed surface with a load of 30 mN. The data were analyzed by the Oliver–Pharr method [32]; the average was taken as the coating hardness.

Table 4.1 Deposition parameters for preparation of the coatings

	(100) oriented c–$Al_xTi_{1-x}N$	(111) oriented c–$Al_xTi_{1-x}N$	TiCN bonding layer	TiN base layer
Temperature (°C)	750	800	880	900
Pressure (kPa)	3.5	2.0	6.5	7.0
Deposition time (min)	210	225	100	30
Total gas flow (L/min)	75.0	60.0	70.0	90.0
$TiCl_4$ (vol%)	0.14	0.21	1.80	0.86
$AlCl_3$ (vol%)	0.78	0.55	–	–
$AlCl_3/(AlCl_3+TiCl_4)$ volume ratio	0.85	0.72	–	–
NH_3 (vol%)	1.5	2.5	–	–
Ar (vol%)	30.0	35.0	–	–
CH_3CN (vol%)	–	–	0.50	–
N_2 (vol%)	–	–	42.0	40.0
H_2 (vol%)	Balance	Balance	Balance	Balance

4.3. Results

4.3.1. Deposition rate of Al-rich single-phase c-$Al_xTi_{1-x}N$ coatings

The deposition conditions for the c-$Al_xTi_{1-x}N$ coatings with (100)- and (111)-preferred orientations are summarized in Table 4.1. Deposition times of 210 and 225 minute were used to achieve an average thickness of 2.5 μm for the (100)- and (111)-oriented c-$Al_xTi_{1-x}N$ coatings, respectively. Thus, the deposition rate was estimated to be 0.70 μm/h for both coatings.

4.3.2. Deposition rate of Al-rich single-phase c-$Al_xTi_{1-x}N$ coatings

Figure 4.1 shows SEM images of the surfaces and cross-sections of the c-$Al_xTi_{1-x}N$ coatings. The surface morphologies of the (100)- and (111)-oriented c-$Al_xTi_{1-x}N$ coatings are shown in Figure 4.1.1A, 4.1.2A, respectively, indicating the octahedral and tetrahedral facets, which represent simple face center cubic faceted (100) and (111) type morphologies, respectively. The cross-sectional SEM images of the c-$Al_xTi_{1-x}N$ coatings show dense columnar structures; the columnar grain size increases along the thickness direction. The average grain sizes calculated from the average grain intercepts method were approximately 0.31 ± 0.05 μm (Figure 4.1.1B) and 0.24 ± 0.05 μm (Figure 4.1.2B) for the (100)- and (111)-oriented c-$Al_xTi_{1-x}N$ coatings, respectively.

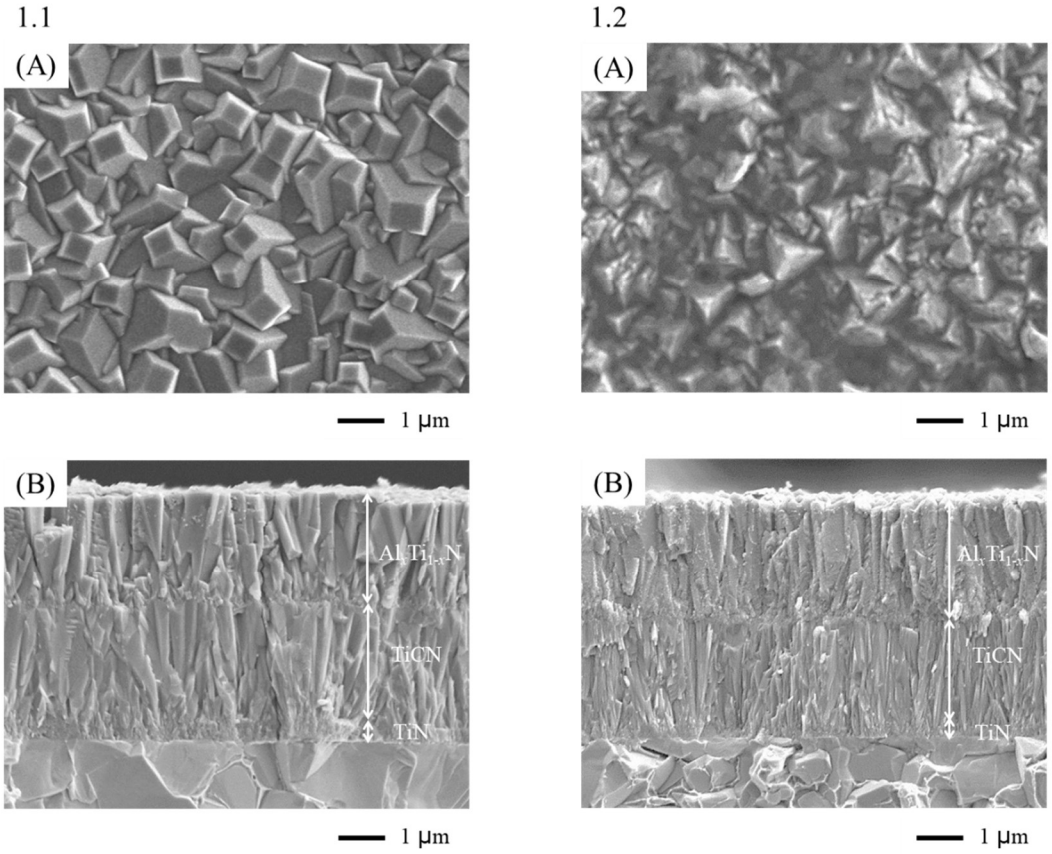

FIGURE 4.1 SEM images of the surface and cross-section of c-$Al_xTi_{1-x}N$ coatings on carbide substrates: 4.1.1(A) and 4.1.1(B) surface and cross-section of (100) c- $Al_xTi_{1-x}N$ (x=0.82); 4.1.2(A) and 4.1.2(B) surface and cross-section of (111) c-$Al_xTi_{1-x}N$ (x=0.73)

IPF mapping (Figure 4.2) of the grain microtextures shows the distribution of crystal orientations along the growth direction of (100)-oriented c-$Al_xTi_{1-x}N$ (Figure 4.2.1) and (111)-oriented c-$Al_xTi_{1-x}N$ (Figure 4.2.2). The dominance of red regions in Figure 4.2.1A and blue regions in Figure 4.2.2A indicates the preferred orientations aligned along the [100] and [111] axes with an increase in the coating thickness. Figure 4.2.1B, 4.2.2B present the degree of preference for the <100> and <111> directions in the c-$Al_xTi_{1-x}N$ coatings; the maximum MRD values were 4.5 and 7.4 for the (100)- and (111)-oriented c-$Al_xTi_{1-x}N$ coatings, respectively.

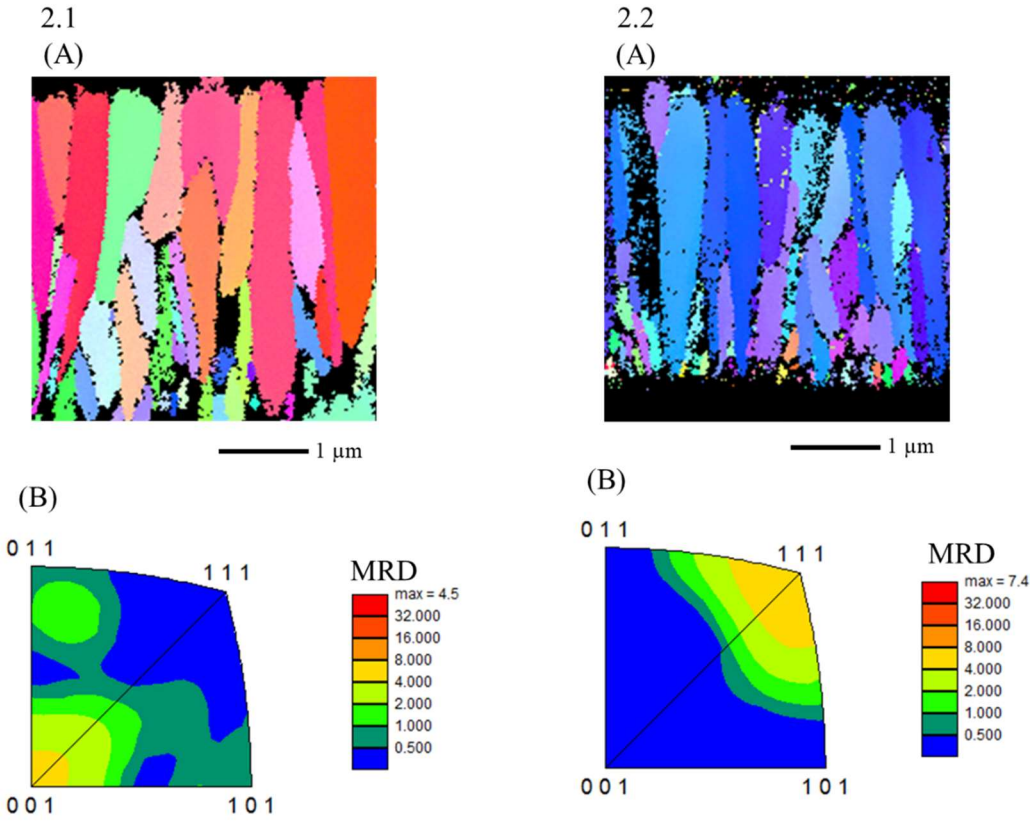

FIGURE 4.2 Electron backscatter diffraction orientation map of normal section of c-$Al_xTi_{1-x}N$ coatings and inverse pole figure with quantified multiples of random distribution values: 4.2.1(A) and 4.2.1(B) EBSD and IPF images of (100) c- $Al_xTi_{1-x}N$ (x=0.82); 2.2(A) and 2.2(B) EBSD and IPF images of (111) c-$Al_xTi_{1-x}N$ (x=0.73)

4.3.3. Nanostructure and chemical composition of Al-rich single-phase c-$Al_xTi_{1-x}N$ coatings

Figure 4.3 shows the high-angle annular dark-field scanning transmission electron microscope (HAADF-STEM) images for the (100)-oriented (Figure 4.3.1) and (111)-oriented (Figure 4.3.2) c-$Al_xTi_{1-x}N$ coatings. The difference in contrast in the images represents the difference in the atomic weight of the elements constituting the coatings. Heavy elements (Ti-rich phase) appear bright and light elements (Al-rich phase) appear dark (Figure 4.3.1A, 4.3.2A). The initial growth stage (<50 nm from the TiC_xN_{1-x} interface) for both c-$Al_xTi_{1-x}N$ coatings was composed of very fine and equiaxial grains with an average grain size of around 50 nm or less. As the coating thickness increased, the equiaxial grains were enveloped by the columnar grains. The (100)- and (111)-oriented c-$Al_xTi_{1-x}N$ grains comprised relatively high Al content [Al(Ti)N] and relatively low Al content [Ti(Al)N] lamellae with a face centered structure (NaCl type). The average periods of the lamellae, determined from the (100)- and (111)-oriented c-$Al_xTi_{1-x}N$ grains, were ~7.7 ± 0.80 and 4.5 ± 0.70 nm, respectively. Figures 4.3.1B, 4.3.2B present high-magnification HAADF-TEM images of the enclosed regions in Figure 4.3.1A, 4.3.2A, respectively. The c-Al(Ti)N and c-Ti(Al)N nanolamellae in (100)- and (111)-oriented c-$Al_xTi_{1-x}N$ were modulated along the <100> direction, as confirmed by Fast Fourier transform in Figure 4.3.1C, 4.3.2C, respectively.

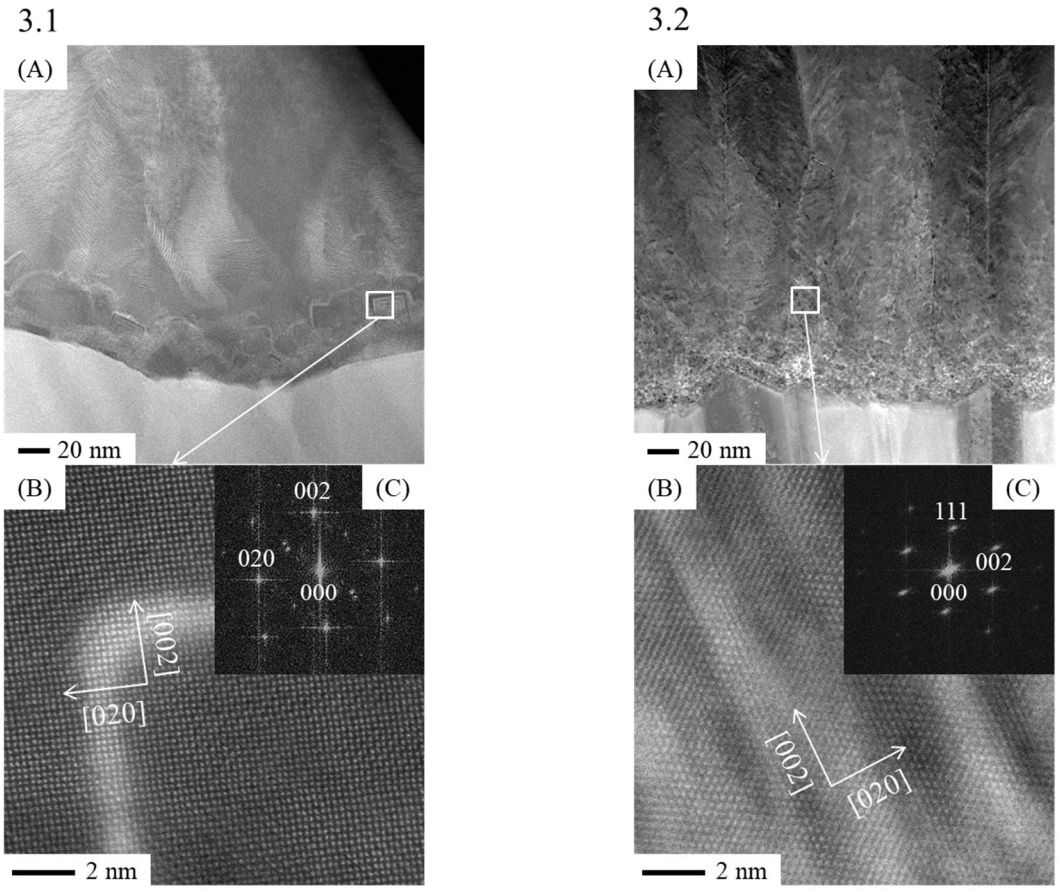

FIGURE 4.3 Cross-sectional scanning transmission electron microscope images of c-$Al_xTi_{1-x}N$ coatings: 4.3.1(A), 4.3.1(B), and 4.3.1(C) HAADF-TEM, HRTEM, and FFT image of (100) c-$Al_xTi_{1-x}N$ (x=0.82); 4.3.2(A), 4.3.2(B), and 4.3.3(C) HAADF-TEM, HR-TEM, and FFT images of (111) c-$Al_xTi_{1-x}N$ (x=0.73)

Chemical composition analyses, performed perpendicular to the modulation direction of the nanolamellae in the (100)- and (111)-oriented c-$Al_xTi_{1-x}N$ coatings, are summarized in Figure 4.4.1 and 4.4.2, respectively. Chlorine was detected at trace levels (<0.1 at.%) in the c-$Al_xTi_{1-x}N$ coatings, and can be ignored. Semi-quantitative chemical composition analyses of the oxygen content in the (100)- and (111)-oriented c-$Al_xTi_{1-x}N$ coatings were statically indifferent (O=4 at.%). The Al/(Al+Ti) atomic ratio in the nanolamellae fluctuated from 0.60 to 0.90 and 0.50 to 0.80 along the <100> direction for the (100)- and (111)-oriented c-$Al_xTi_{1-x}N$ coatings, respectively. The average chemical compositions and corresponding *x* values for the (100)- and (111)-oriented c-$Al_xTi_{1-x}N$ are listed in Table 4.2.

4. 1

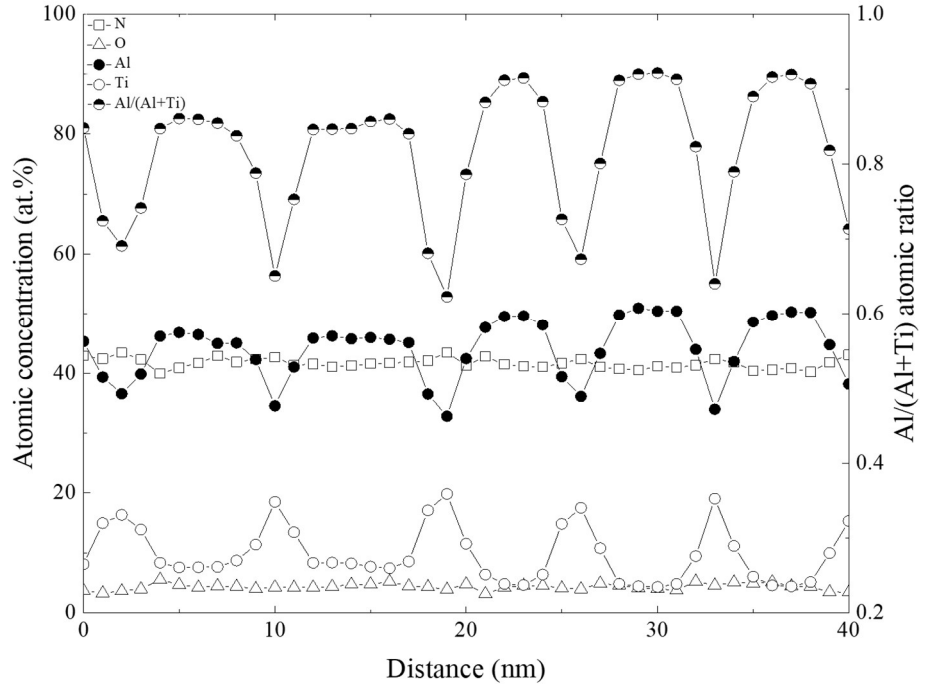

4. 2

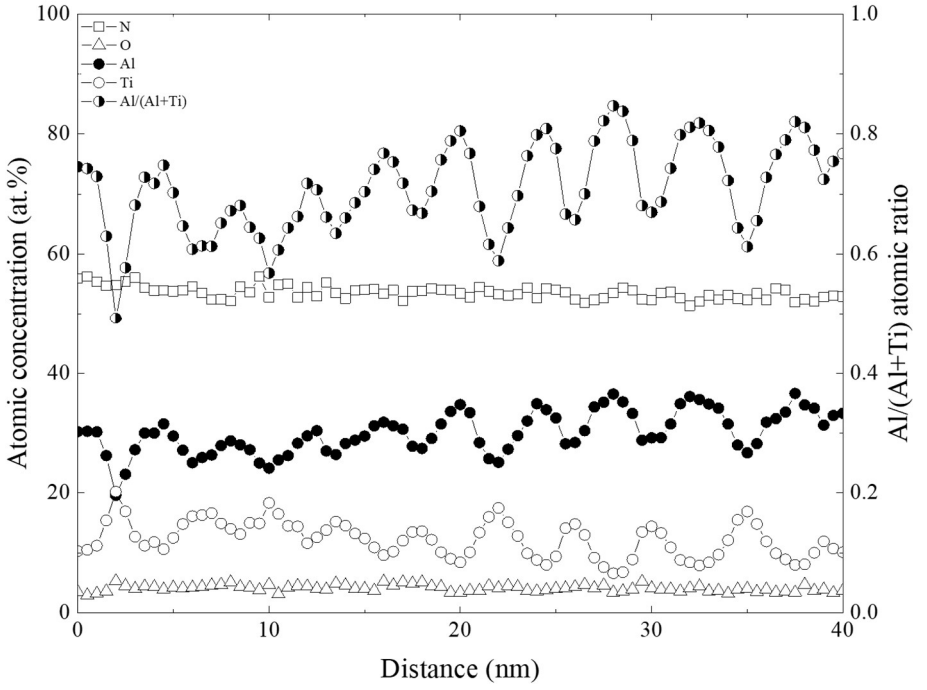

FIGURE 4.4 Chemical compositions of nanolamellae in c-$Al_xTi_{1-x}N$ coatings semi-quantitatively determined by TEM-EDX: 4.4.1 EDX analysis perpendicular to lamella direction in (100) c-$Al_xTi_{1-x}N$ (x=0.82); 4.4.2 EDX analysis perpendicular to lamella direction in (111) c-$Al_xTi_{1-x}N$ (x=0.73)

TABLE 4.2 Semi-quantitative analysis for chemical composition of coatings by EDX

At.%	(100) oriented c–$Al_xTi_{1-x}N$	(111) oriented c–$Al_xTi_{1-x}N$
Al	44.4 ± 5.2	31.2 ± 4.1
Ti	9.7 ± 4.8	11.5 ± 3.3
N	41.6 ± 0.8	53.3 ± 1.2
O	4.3 ± 0.5	4.0 ± 0.6
Fraction x in $Al_xTi_{1-x}N$	0.82 ± 0.09	0.73 ± 0.08

4.3.4. Thermal stability and mechanical properties of Al-rich single-phase c-$Al_xTi_{1-x}N$ coatings

The thermal stability of the as-deposited c-$Al_xTi_{1-x}N$ coatings was determined via HT-XRD analyses (Figure 4.5) from RT to 1000°C. The cubic phase in the (100)- and (111)-oriented c-$Al_xTi_{1-x}N$ coatings remained stable up to 1000°C (Figure 4.5A, B). Formation of κ-Al_2O_3 and rutile type TiO_2 was observed in the (111)-oriented c-$Al_xTi_{1-x}N$ coating at 1000°C due to leakage of an air trace during the measurement; however, transformation of the cubic phase to the hexagonal phase did not occur (Figure 4.5B). Arc-evaporated c-$Al_xTi_{1-x}N$ (reference sample) was stable up to 800°C (Figure 4.5C); above 900°C, the phase determination was invalid due to exudation of the Co binder from the cemented carbide substrate to the coating surface.

The average hardness of the as-deposited (100)- and (111)-oriented c-$Al_xTi_{1-x}N$ and arc-evaporated c-$Al_xTi_{1-x}N$ coatings (33, 36, and 38 GPa, respectively) was measured via nanoindentation. Residual stress measurements indicated high tensile stress values of 1.8 and 4.6 GPa for the (100)- and (111)-oriented c-$Al_xTi_{1-x}N$ coatings. The stress in the arc-evaporated c-$Al_xTi_{1-x}N$ was compressive (3.6 GPa). The stress-free lattice parameter increased from 4.098 through 4.135 to 4.150 (Å) with a decrease in the Al content for the (100)- and (111)-oriented c-$Al_xTi_{1-x}N$ with x = 0.82 and 0.73 and the arc-evaporated c-$Al_xTi_{1-x}N$ (x=0.6), respectively, as summarized in Table 4.3.

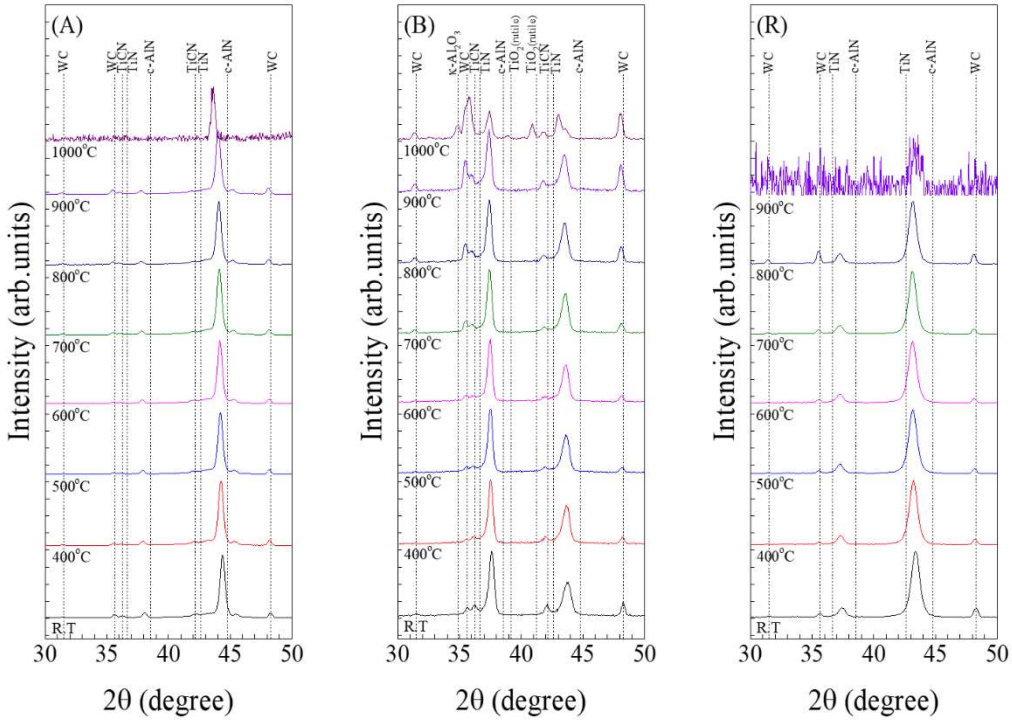

FIGURE 4.5 In situ X-ray diffraction patterns of c-$Al_xTi_{1-x}N$ coatings from room temperature to 1000°C: (A) CVD (100) c-$Al_xTi_{1-x}N$ (x=0.82); (B) CVD (111) c-$Al_xTi_{1-x}N$ (x=0.73); and (C) arc-evaporated c-$Al_xTi_{1-x}N$ (x=0.60)

Table 4.3 Some physical properties of deposited c- $Al_xTi_{1-x}N$ coatings

	(100) oriented c–$Al_xTi_{1-x}N$(x=0.82)	(111) oriented c–$Al_xTi_{1-x}N$(x=0.73)	Arc-evaporated $Al_xTi_{1-x}N$(x=0.6) [Ref.]
Stress-free lattice constant (Å)	4.098	4.135	4.150
c–Al(Ti)N/c–Ti(Al)N Nanolamellae period (nm)	7.7 ± 0.8	4.5 ± 0.7	–
Indentation Hardness (GPa)	32.5 ± 2.2	36.3 ± 2.7	38.0 ± 2.3
Residual Stress (GPa)	1.8 ± 0.2 (Tensile)	4.6 ± 0.3 (Tensile)	3.6 ± 0.1 (Compressive)

4.4 Discussion

4.4.1 Microstructural evolution

The data in Figures 4.1-4.3 generally indicate the typical structure for evolutionary selection growth [33]. The evolutionary selection growth is related to the growth rate anisotropy in gas-solid surface diffusivities and adatom potential energies. A low temperature (750°C),

low vacuum (3.5 kPa), and a high $AlCl_3/(AlCl_3+TiCl_4)$ volume ratio equal to 0.85 produced c-$Al_xTi_{1-x}N$ (x = 0.82) with the (100)-preferred orientation. A plausible reason is the difference in the probability of sticking between the growth species on the (100) and (111) plane. The plane with the highest sticking probability has the highest growth rate and tends to become the preferred orientation. Yumoto et al. proposed an extended periodic bond chain model to dictate the highest sticking probability plane in sputtered AlN [34]. According to this model, if the coating is composed of AB [eg, TiN or (TiAl)N] and the growth species are A-B, then the components A and B will have a higher sticking probability. In the region where the precursor is an atom, the (111) plane has the highest sticking probability for the face centered cubic structure. Conversely, if the precursor is a dimer (Ti–N or Al–N) the highest sticking plane becomes the (100) plane because this plane has both metals (Ti or Al) and N on the topmost surface [35]. The criteria for estimating whether the precursor is an atom or dimer are the space distance L (herein, L is considered as the thickness of the carbon tray=25 mm) and the mean free path of the precursors. If the mean free path is longer than L, the precursor is considered as an atom. At 750°C and 3.5 kPa, the first approximation of the mean free path is calculated as 1.0 μm for $TiCl_4$ and 2.4 μm for $AlCl_3$; thus, the precursors are considered as dimers, and the highest sticking plane becomes the (200) plane and the preferred orientation is the <100> direction. At a higher deposition temperature and under higher vacuum conditions, the surface diffusivities of the adatoms are considered to increase. In this case, the highest surface energy plane becomes the preferred orientation. A plausible reason is that surface diffusion occurs to minimize the surface energy of the grain; thus, the highest surface energy plane receives a greater flux of adatoms and has a higher growth rate. Consequently, the grain normal to the substrate, with highest surface energy, becomes the dominant orientation and envelops the other grain by the evolutionary selection process. The surface with the highest potential energy for c-AlN [36] and c-TiN [37] was determined to be the (111) plane; therefore, at 800°C and 20 kPa, the preferred orientation is (111).

4.4.2 Nanolamellae formation

The structure of the c-$Al_xTi_{1-x}N$ coating comprises orderly modulated c-Al(Ti)N/c-Ti(Al)N nanolamellae and the Al/(Al+Ti) atomic ratio fluctuated along the <100> direction (Figure 4.3). The maximum solubility of Al in c-$Al_xTi_{1-x}N$ solid solution is considered as *x* below 0.7 [3,14,15]. Increasing the *x* value in c-$Al_xTi_{1-x}N$ leads to increased formation energy [38,39], possible cubic-to-hexagonal phase transformation, and deteriorated mechanical properties [16]. The template effect can be exploited to stabilize c-$Al_xTi_{1-x}N$ cubic phases with high *x* values. Setoyama et al. deposited a c-AlN/c-TiN superlattice via arc evaporation [12]. The critical superlattice period to maintain the c-AlN phase was less than 3 nm. Chawla et al. suggested that c-AlN could be stable above 10 nm in the AlN/$Al_xTi_{1-x}N$ superlattice, depending on the *x* value and substrate, using the Finite Element Method and Density Functional Theory calculation.31 Herein, the (100)- and (111)-oriented c-$Al_xTi_{1-x}N$ coatings comprised c-$Al_{0.9}Ti_{0.1}N$/c-$Al_{0.6}Ti_{0.4}N$ and c-$Al_{0.80}Ti_{0.20}N$/c-$Al_{0.50}Ti_{0.50}N$ nanolamellar structures, respectively. Thus, the lattice misfit at the interface of the above-mentioned nanolamellae is considered small, the cubic structure can be stabilized, and the average *x* value in c-$Al_xTi_{1-x}N$ can remain high. The another question is how the c-Al(Ti)N/c-Ti(Al)N nanolamellae are formed in c-$Al_xTi_{1-x}N$ by LP-CVD. Told et al. [19] reported self-organized nanolamellae in c-$Al_{0.8}Ti_{0.2}N$ for a $TiCl_4$–$AlCl_3$–NH_3–N_2–H_2 precursor system using industrial-plant LP-CVD. Nanolamellae formation was attributed to film growth kinetics because the growth rate of the c-$Al_{0.8}Ti_{0.2}N$ coating is high (~5 µm/h). Herein, c-Al(Ti)N/c-Ti(Al)N nanolamellae were formed despite the low growth rate of 0.7 µm/h. Therefore, the hypothesized formation of self-organized nanolamellae in c-$Al_xTi_{1-x}N$ by LP-CVD due to kinetic growth control is inadequate. We propose that the self-organized nanolamellae in c-$Al_xTi_{1-x}N$ formed by LP-CVD arise via a spinodal decomposition process [40]. The Ti–Al–N system reportedly undergoes spinodal decomposition around 700°C–800°C depending on the Al content in c-$Al_xTi_{1-x}N$.[5] This is equivalent to the deposition temperature herein and in prior work [19]. Detailed explanations of the thermodynamic and kinetic spinodal decomposition of c-$Al_xTi_{1-x}N$ are given by Mayrhofer et al [41]. and Alling et al [42]. Microstructure formation is governed by minimizing the total free energy as follows:

$$G_{sys} = G_{chem} + E_{surf} + E_{str} \quad Eq.(4.4)$$

(G_{chem}: chemical energy, E_{surf}: interfacial energy; E_{str}: elastic strain energy [43]). The driving force is G_{chem} (>0), whereas E_{surf} and E_{str} retard microstructure formation. Phase separation occurs spontaneously to minimize G_{sys}. G_{sys} is most effectively reduced by minimizing E_{surf} and E_{str}. Spinodal decomposition occurs without nucleation, facilitating G_{sys} minimization. Spinodal decomposition is influenced by the elastic anisotropy of the matrix and precipitate, thus elastically soft directions become preferred modulation directions as E_{str} is minimized.

E_{str} is expressed as follows:

$$E_{str} = \eta^2 Y_{<hkl>}(c - c_0)^2 \quad Eq.(4.5)$$

[$(c - c_0)$: concentration fluctuation, g: lattice misfit, and Y(hkl): Young's modulus for the <hkl> direction]. We assume $(c-c_0)$ as the differential in the Al/(Al+Ti) atomic ratio, and g is the lattice misfit in Al-rich c-Al(Ti)N and Ti-rich c-Ti(Al)N, respectively. To minimize E_{str}, Y(hkl) must be at a minimum, accounting for why spinodal decomposition results in periodic and highly oriented modulation of two coherent phases with concentration fluctuation along the elastically soft directions [40]. In a cubic system, the elastically soft directions can be correlated with Zerner's anisotropy factor A as follows [44]:

$$A = \frac{2C_{44}}{(C_{11} - C_{12})} \quad Eq.(4.6)$$

where, C_{11}, C_{12}, and C_{44} are the compositionally dependent elastic constants of $Al_xTi_{1-x}N$. A<1 and A>1, respectively, predict that the Young's modulus is minimum along the <111> and <100> direction. The compositional-dependent value of the elastic constant of $Al_xTi_{1-x}N$ obtained by first principles calculation45 gives an anisotropy factor of A≥1, and hence predicts concentration fluctuation along the <100> direction. These predictions support our hypothesis that the self-organized nanolamellae in c-$Al_xTi_{1-x}N$ formed by LP-CVD occur via coherent spinodal decomposition.

4.4.3 Mechanical properties and phase stability

The stress-free lattice parameter for the (100)- and (111)-oriented c-$Al_xTi_{1-x}N$ formed by LP-CVD and c-$Al_xTi_{1-x}N$ from arc evaporation increased (4.098, 4.135, and 4.150 Å) with a decrease in the Al content in c-$Al_xTi_{1-x}N$ (x=0.82, 0.73, and 0.60) (Table 4.3). This trend is reasonable given that the lattice parameter of c-AlN (4.075 Å) is smaller than that of c-TiN (4.250 Å) [31]. The indentation hardness of the c-$Al_xTi_{1-x}N$ coatings formed by LP-CVD varied from 33 to 36 GPa, depending on the (100) or (111)-preferred orientation, consistent with the Al-rich c-$Al_{0.8}Ti_{0.2}N$ coating reported by Todt et al [19]. The hardness of the c-$Al_xTi_{1-x}N$ coatings in the as-deposited state is influenced by the chemical composition [17], microstructure [12], and residual stress [46]. The residual stress [$\sigma(T)$], the coating is composed of thermal stress and intrinsic stress, defined as follows [47]:

$$\sigma(T) = \sigma_i + \frac{E_f}{(1-v_f)}(\alpha_f - \alpha_s)(T_d - T) \quad Eq.(4.7)$$

(σ_i: intrinsic stress, $E_f/(1-\upsilon_f)$: biaxial elastic modulus, α_f and α_s: thermal expansion coefficient (TEC) of the coating and substrate, T_d and T: deposition and stress evaluation temperature). From theory [48] and experiment [49], the TEC of c-$Al_xTi_{1-x}N$ (x=0.6 to 1.0) varies from 9.5-8.1 x 10^{-6}/°C, which is larger than that of the WC-Co substrate (5.0-6.0 x 10^{-6}/°C) [50]; thus, thermal stress is a tensile state. The intrinsic stress in arc-evaporated c-$Al_xTi_{1-x}N$, which varies according to the process parameters (eg, arc current, bias voltage, and so on), is commonly compressive as highly energetic ions or particles impinge the surface of the substrate. First approximation of the thermal stress by applying the E_f and υ_f mentioned in Section II(2), along with α_f, α_s=8.1, 5.0 x 10^{-6}/°C, T_d=800°C, 750°C (Table 4.1), for the (100)- and (111)-oriented c-$Al_xTi_{1-x}N$ coating results in respective tensile stress values of about 1.0 and 1.4 GPa. These values are smaller than the measured value (Table 4.3). This implies that another tensile stress must be taken into account to explain the higher measured value. Another possible source of the tensile stress is coherent stress in the nanolamellae in c-$Al_xTi_{1-x}N$. Chawla et al. studied coherent stress in cubic TiN/AlN bilayers and multilayers using FEM [51], suggesting that tensile stress in c-AlN becomes as high as

8.19 GPa for TiN (1 nm)/AlN (10 nm) because the smaller lattice parameter of c-AlN must be coherent with the larger value of c-TiN. Herein, the difference in the Al/(Al+Ti) ratio of the c-Al(Ti)N and c-Ti(Al)N nanolamellae is about 0.30 for the (100)- and (111)-oriented c-$Al_xTi_{1-x}N$ coatings; thus, the tensile stress is considered lower than the c-TiN/c-AlN coherency stress, but should be tensile stress.

The thermal stability of the metastable c-$Al_xTi_{1-x}N$ coating reportedly declines with increasing *x*. Norrby et al. studied the cubic-to-hexagonal transformation in arc-evaporated c-$Al_xTi_{1-x}N$ with *x*=0.45 and 0.64 using in situ X-ray [52]; the cubic-to-hexagonal transformation occurred around 950°C, and the activation energy decreased from 350 to 320 kJ/mol when *x* increased from 0.45 to 0.64. Herein, the cubic phase was stable up to 1000°C, even for *x* as high as 0.73 and 0.82. The cubic-to-hexagonal transformation in c-$Al_xTi_{1-x}N$ occurs via cubic AlN-rich and cubic TiN-rich domain separation (spinodal decomposition); finally, metastable cubic AlN is transformed to thermodynamically stable wurtzite AlN (nucleation). The cubic-to-hexagonal transformation is affected by the composition and the Al distribution [39]. The present (100)- and (111)-oriented c-$Al_xTi_{1-x}N$ coatings were composed of c-Al(Ti)N and c-Ti(Al)N nanolamellae with periods of 7.7 ± 0.80 and 4.5 ± 0.70 nm, respectively. These nanolamellae probably act as a diffusion barrier and delay the nucleation of wurtzite AlN. However, the maximum allowable working temperature of HT-XRD limited the thermal stability evaluation above 1000°C. Further study is needed to derive the exact source of the thermal stability and quantitative kinetic evaluation is also important for providing information for practical use of the coatings in metal cutting.

4.5 Summary

The findings of this study can be summarized as follows:

1. Formation of the (100)- and (111)-oriented c-$Al_xTi_{1-x}N$ coating is governed by evolutionary selection growth. Low temperature, low vacuum, and a high $AlCl_3/(AlCl_3+TiCl_4)$ volume ratio resulted in (100)-preferred orientation. In contrast, higher deposition temperature, higher vacuum, and a lower $AlCl_3/(AlCl_3+TiCl_4)$ volume ratio promoted the (111)-preferred orientation.

2. The (100)- and (111)-oriented c-$Al_xTi_{1-x}N$ coating consisted of c-Al(Ti)N/c-Ti(Al)N

nanolamellae with respective average compositions of c-$Al_{0.9}Ti_{0.1}N$/c-$Al_{0.6}Ti_{0.4}N$ and c-$Al_{0.80}Ti_{0.20}N$/c-$Al_{0.50}Ti_{0.50}N$, and average lamellar periods of 7.7 ± 0.8 and 4.5 ± 0.7 nm. The c-Al(Ti)N/c-Ti(Al)N nanolamellae were modulated along the <100> direction, plausibly by spinodal decomposition in the as-deposited state.

3. The as-deposited c-$Al_xTi_{1-x}N$ coating has high hardness, varying from 33 to 36 GPa depending on the (100)- or (111)-preferred orientation. The c-$Al_xTi_{1-x}N$ (x=0.82 and 0.73) coating remained stable at 1000°C. Residual tensile stress is generated due to the difference between the TECs of the c-$Al_xTi_{1-x}N$ coating and carbide substrate, and coherency stress in the c-Al(Ti)N/c-Ti(Al)N nanolamellae. Residual tensile stress releasing is needed and cutting performance evaluations are underway.

References in chapter 4

[1] O. Knotek, J. Solid State Chem. 70 (1987) 318–322.

[2] W.D. Munz, J. Vac. Sci. Technol., A 4 (1986) 2717–2725.

[3] I. Tsutomu, S. Hiroshi, Thin Solid Films 195 (1991) 99–110.

[4] T. Leyendecker, O. Lemmer, S. Esser, J. Ebberink, Surf Coat Technol. 48 (1991)175–178.

[5] P.H. Mayrhofer, A. Horling, L. Karlsson, Appl. Phys. Lett. 83 (2003) 2049–2051.

[6] G. Erkens, R. Cremer, T. Hamoudi, Surf Coat Technol. 177-178 (2004) 727–734.

[7] K. Yamamoto, J Temp Soc. 33 (2007) 84–89.

[8] W.D. Munz, I. Smith, L. Donohue, Society of Vacuum Coaters 40th Annual Technical Conference. New Orleans, LA. (1997) 89–93.

[9] B. Yang, L. Chen, Y.X. Xu, Int J Refract Met Hard Mater. 38 (2013) 81–86.

[10] R. Rachbauer, D. Holec, P.H. Mayrhofer, Surf Coat Technol. 211 (2012) 98–103.

[11] H. Riedl, D. Holec, R. Rachbauer, Surf Coat Technol. 235 (2013) 174–180.

[12] M. Setoyama, A. Nakayama, M. Tanaka, N. Kitagawa, T. Nomura, Surf Coat Technol. 86-87 (1996) 225–230.

[13] L. Chen, Y.X. Xu, Y. Du, Y. Liu, Thin Solid Films 592 (2015) 207–214.

[14] Y. Makino, Mater. Jpn. 36 (1997) 996–1003.

[15] A. Kimura, H. Hasegawa, K. Yamada, T. Suzuki, Surf Coat Technol. 120-121 (1999) 438–441.

[16] A. Horling, L. Hultman, M. Oden, J. Sjolen, L. Karlsson, Surf Coat Technol. 191 (2005) 384–392.

[17] I. Endler, M. Hohn, M. Herrmann, Surf Coat Technol. 203 (2008) 530–533.

[18] A. Kopf, J. Keckes, J. Todt, R. Pitonak, R. Weissenbacher, Mater. Sci. Forum 825-826 (2015) 597–604.

[19] J. Todt, J. Zalesak, R. Daniel, Surf Coat Technol. 291 (2016) 89–93.

[20] J. Keckes, R. Daniel, C. Mitterer, Thin Solid Films 545 (2013) 29–32.

[21] J. Todt, R. Pitonak, A. Kopf, Surf Coat Technol. 258 (2014) 1119–1127.

[22] A. Paseuth, H. Fukui, S. Okuno, H. Kanaoka, Y. Okada, Surf Coat Technol. 260 (2014) 139–147.

[23] A. Paseuth, H. Fukui, K. Yamagata, Surf Coat Technol. 291 (2016) 54–61.

[24] A. Paseuth, K. Yamagata, S. Okuno, United States Patent No. US0345012 A1 (2015).

[25] A. Paseuth, K. Yamagata, S. Okuno, H. Kanaoka, H. Morimoto, M. Itoh, US Patent No. US0345013 (2015).

[26] S. Ruppi, Surf Coat Technol. 202 (2008) 4257–4269.

[27] G.S. Rohrer, Comprehensive Hard Materials. Oxford: Elsevier; (2014) 265–284.

[28] E. Prince, A.J.C. Wilson, T. Hahn, U. Shmueli, International Tables for Crystallography, Vol C. Dordrecht, the Netherlands: International Union of Crystallography; (1999) 213.

[29] N. Norrby, M.P. Johansson-Joesaar, M. Oden, Surf Coat Technol. 257 (2014) 102–107.

[30] Y. Asahi, S. Takayama, J. Jpn. Inst. Met. 72 (2008) 323–330.

[31] V. Chawla, D. Holec, P.H. Mayrhofer, Thin Solid Films 565 (2014) 94–100.

[32] W.C. Oliver, G.M. Pharr, J. Mater. Res. 19 (2004) 3–20.

[33] A. Van der Drift, Philips Res. Repts. 22 (1967) 267–288.

[34] H. Yumoto, M. Ishihara, T. Kaneko, J. Jpn. Assoc. Cryst. Growth 23 (1996) 382–388.

[35] Y. Kajikawa, S. Noda, H. Komiyama, J. Vac. Sci. Technol., A 21 (2003) 1943–1954.

[36] D. Holec, P.H. Mayrhofer, Scripta Mater. 67 (2012) 760–762.

[37] L. Hultman, J.E. Sundgren, J.E. Greene, J. Appl. Phys. 66 (1989) 536–544.

[38] M. Kawate, A. Kimura, T. Suzuki, J. Vac. Sci. Technol., A 20 (2002) 569–571.

[39] P.H. Mayrhofer, D. Music, J.M. Schneider, J. Appl. Phys. 100 (2006) 094906.

[40] J.W. Cahn, Acta Metall. 10 (1962) 179–183.

[41] P.H. Mayrhofer, F.D. Fischer, H.J. Bohm, C. Mitterer, J.M. Schneider, Acta Mater. 55 (2007) 1441–1446.

[42] B. Alling, A.V. Ruban, A. Karimi, Phys Rev B: Condens Matter. 75 (2007) 045123.

[43] T. Miyazaki. Mate. Jpn. 53 (2014) 363–369.

[44] C.M. Zener. Elasticity and Anelasticity of Metals. Chicago, IL: University of Chicago Press (1948).

[45] F. Tasnadi, I.A. Abrikosov, L. Rogstrom, J. Almer, M.P. Johansson, M. Oden, Appl. Phys. Lett. 97 (2010) 231902.

[46] K. Sato, N. Ichimiya, A. Kondo, Y. Tanaka, Surf Coat Technol. 163 (2003) 135–143.

[47] J.A. Thornton, D.W. Hoffman, Thin Solid Films 171 (1989) 5–31.

[48] M. Bartosik, M. Todt, D. Holec, Appl. Phys. Lett. 107 (2015) 071602.

[49] K. Yamamoto, T. Sato, E. Iwamura, J. Surf. Finish. Soc. Jpn. 50 (1999) 52–57.

[50] R. Kieffer, R. Benesovsky. Hartmetalle. Wien, NY: Springer Verlag; (1965) 157.

[51] V. Chawla, D. Holec, P.H. Mayrhofer, Comput. Mate.r Sci. 55 (2012) 211–276.

[52] N. Norrby, L. Rogstrom, M.P. Johansson-Joesaar, N. Schell, M. Oden, Acta Mater. 73 (2014) 205–214.

Chapter 5. Thermal stability of Al-rich $Al_xTi_{1-x}N$ coatings prepared by low-pressure chemical vapour deposition

5.1. Introduction

Cubic (c-) $Al_xTi_{1-x}N$ has been extensively studied in the cutting tool industry among hard coatings of transition-metal nitrides, owing to its high oxidation resistance compared to TiN [1, 2] and age hardening via spinodal decomposition [3]. Nevertheless, coated tools with better performance are needed for dry cutting and higher cutting speeds with lower cost and environmental impact. Efforts to improve the wear and thermal resistance of c-$Al_xTi_{1-x}N$ coatings include increasing the Al content [4,5] or modulation of the multi-layered structure [6,7], leading to increased hardness and toughness.

The traditional method for fabricating c-$Al_xTi_{1-x}N$ in the tool industry is physical vapour deposition (PVD) [8–10], and the maximum aluminium content *x* is limited to 0.67 to maintain the metastable cubic structure. Higher values of *x* result in a mixture of cubic and hexagonal (h-) AlN phases [11], which deteriorate the mechanical properties [12]. Recently, we reported that single-phase c-$Al_xTi_{1-x}N$ coatings with an average composition of x=0.7–0.8 comprising a c-Al(Ti)N/c-Ti(Al) self-organised nanolamellar microstructure could be successfully synthesised via low-pressure chemical vapour deposition (LP-CVD) in an industrial plant using the $AlCl_3$–$TiCl_4$–NH_3–Ar–H_2 precursor system [13]. However, the effects of the post-annealing temperature on the physical properties and microstructural evolution of Al-rich c-$Al_xTi_{1-x}N$ coatings have not been thoroughly investigated, even though they are important questions because the hard coating is exposed to high temperatures during the cutting operation [14].

Norrby et al. studied the phase stability of c-$Al_xTi_{1-x}N$ (x=0.45 and 0.64) prepared by arc-evaporated PVD, and suggested that a coating with a higher *x* has a significantly faster rate of h-AlN phase transformation [15]. Furthermore, Knutsson et al. suggested that the metastable c-$Al_xTi_{1-x}N$ coating transforms into the thermodynamically stable h-AlN and c-TiN phases. The transformation is correlated with the coarsening of c-AlN-rich domains at elevated temperatures, which is governed by the diffusion process [16]. Moreover,

Hollerweger et al. indicated that this phase transformation can be suppressed by decreasing the stored mixing energy [17]. Since Al-rich c-$Al_xTi_{1-x}N$ prepared by LP-CVD with a high value of x (≥0.7) comprises c-$Al_xTi_{1-x}N$ (x≈0.5)/c-$Al_xTi_{1-x}N$ (x≈0.9) with a narrow nanolamellar period (4–8 nm), the coarsening behaviour of the c-AlN-rich domain could be different in this case compared to the single-phase c-$Al_xTi_{1-x}N$ coating prepared via the conventional PVD process.

The purpose of this study is to investigate the thermal stability of c-$Al_xTi_{1-x}N$ (x = 0.7, 0.8) coatings prepared by LP-CVD, and to clarify the effect of the post-annealing temperature on the physical properties and microstructural evolution. c-$Al_xTi_{1-x}N$ coatings with an average aluminium content of x = 0.7 and 0.8 comprising c-Al(Ti)N/c-Ti(Al) nanolamellae were isothermally annealed at temperatures of 500 to 1200°C for 1 h. These coatings were analysed by transmission electron microscopy and X-ray diffraction to evaluate their phase stability. The mechanical properties of the post-annealed c-$Al_xTi_{1-x}N$ coatings were also investigated and compared with those of a commercially available arc-evaporated c-$Al_xTi_{1-x}N$ (x=0.6) coating. These results could help establish guidelines for future high-performance tools that are based on an Al-rich single layer or a bilayer coating consisting of a c-$Al_xTi_{1-x}N$ layer with a second layer (e.g. Al_2O_3) on top [18].

5.2. Experimental procedures

c-$Al_xTi_{1-x}N$ coatings having an average aluminium content of x=0.7 and 0.8 were deposited using a commercially available hot-wall LP-CVD reactor with an $AlCl_3$–$TiCl_4$–NH_3–Ar–H_2 precursor system. WC–5 wt%Co (SNMA120408; Sumitomo Electric Hardmetal Corp., Hyogo, Japan) with mirror-polished surfaces were used as substrate to evaluate the physical properties. The substrates were centrally loaded in a coating batch, as described in related work [19]. A TiN base layer with an average thickness of 0.5 µm and a 2.0-µm-thick TiC_xN_{1-x} bonding layer were deposited to guarantee adhesion between the coatings and the carbide substrates. The c-$Al_xTi_{1-x}N$ coatings with an average thickness of 2.0 µm were then individually deposited, and the deposition conditions are listed in Table 5.1. A more detailed description can be found in Ref. [13].

Table 5.1. Deposition parameters of the $Al_xTi_{1-x}N$ coatings

	$Al_{0.8}Ti_{0.2}N$ (LP-CVD)	$Al_{0.7}Ti_{0.3}N$ (LP-CVD)	$Al_{0.6}Ti_{0.4}N$ (PVD)
Temperature (°C)	750	800	500
Pressure (kPa)	3.5	2.0	2.6×10^{-3}
$AlCl_3$ (vol%)	0.78	0.55	-
$TiCl_4$ (vol%)	0.14	0.21	-
NH_3 (vol%)	1.5	2.5	-
Ar (vol%)	30	35	-
H_2 (vol%)	Balance	Balance	-
Target composition (at%)	-	-	Al60Ti40
N_2 flow (L/min)	-	-	1.0
Arc curent (A)	-	-	150
Bias voltage (V)	-	-	-40
Thickness (μm)	2.0	2.0	3.0

Isothermal post-annealing at temperatures between 500°C and 1200°C in steps of 100°C was carried out in a protective argon atmosphere at ambient pressure using heat-treatment furnaces (PHSG; Shimadzu Mectem, Inc., Shiga, Japan). The samples were heated at the rate of 10 °C/min and kept for 1 h at the desired temperature. After annealing, the samples were cooled down to room temperature with a cooling rate of ca. 40 °C/min. The thermal stability of the CVD c-$Al_xTi_{1-x}N$ coatings was compared with that of a 3-μm-thick arc-evaporated PVD c-$Al_xTi_{1-x}N$ (x=0.6) coated on a cement carbide substrate (AC1030U; Sumitomo Electric Hardmetal Corp., Hyogo, Japan).

Structural and phase analyses were conducted by X-ray diffraction (XRD; RIGAKU, Tokyo, Japan, SmartLab; 45 kV, 200 mA, Cu-Kα radiation). The XRD measurements were performed in the grazing incidence geometry (angle of incidence: 2°).

The microstructure of the post-annealed coatings was evaluated using high-resolution transmission electron microscopy (HRTEM; JEM-2100F, JEOL, Tokyo, Japan) with energy-dispersive X-ray spectroscopy (EDX; JED-2300, JEOL) to enable elemental analysis. Cross-sectional TEM samples were prepared by using a focused ion beam (FIB; JIB-4501; JEOL Tokyo, Japan) with Ga+ beam milling (accelerating voltage: 30 kV). Change in the nanostructure of the c-$Al_xTi_{1-x}N$ coatings (e.g. phase separation by spinodal decomposition, coarsening, grain growth, etc.) before and after the post-annealing were semi-quantitatively extracted by the linear intercepts using TEM images and the "ImageJ" image analysis software [20], assuming that the compositional wavelength (λ_m) is equivalent to the average

interval between the contrast peaks of the Al-rich domain. The interdiffusion coefficient ($\widetilde{D}$) was approximated by the increase in the compositional wavelength with the three-dimensional root-mean-square displacements [21]:

$$\widetilde{D} = \frac{(\lambda_m - \lambda_0)^2}{6t} \quad Eq.(5.1)$$

where λ_0 is the compositional wavelength in the as-deposited state, and t is the post-annealing time (fixed at 1 h).

The hardness of the as-deposited and post-annealed c-$Al_xTi_{1-x}N$ coatings were measured using a nanoindentation tester (ENT-1100a; Elionix, Tokyo, Japan) and a Berkovich diamond-shaped tip indenter. The indentation test was performed at 10 locations over the smoothed surface with a load of 30 mN. The indentation hardness was analysed using the Oliver and Pharr method [22], and the average and standard deviation were extracted to characterise the coating hardness.

5.3. Results

5.3.1. Phase stability and nanostructural evolution of the c-$Al_xTi_{1-x}N$ coatings

5.1 shows the XRD patterns of the as-deposited and post-annealed c-$Al_xTi_{1-x}N$ (x=0.8, 0.7, and 0.6) coatings heated at 500–1200°C for 1 h. The sample with x=0.8 (Fig. 5.1A) was metastable up to 900°C; while those with x=0.7 post-annealed at 900°C (Fig. 5.1B) and x=0.6 post-annealed at 800°C (Fig. 5.1C) exhibited a weak signal at about 2θ=33°, indicating the formation of the h-AlN phase. The peaks near 2θ=44° for the c-$Al_xTi_{1-x}N$ (x=0.8) coating (Fig. 5.1A, labelled by "*") were detected in both the as-deposited state and after heating at 900°C, suggesting the existence of a coherent layer aligned along the <100> direction. The peak broadening at 2θ≈44° for the c-$Al_xTi_{1-x}N$ coatings with x=0.8 and x=0.7 at 900°C (Fig. 5.1A and 5.1B, respectively) and x=0.6 at 800°C (Fig. 5.1C) indicated spinodal decomposition, as will be described later. The phase transition from c-AlN to h-AlN is complete for all coatings after post-annealing at 1100°C.

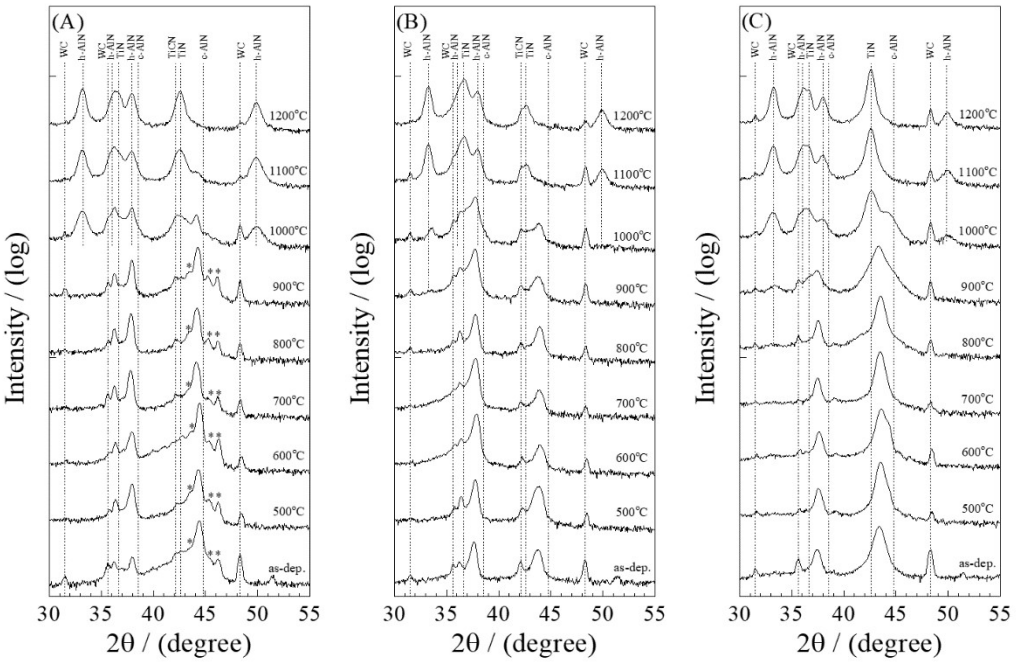

Fig. 5.1. XRD patterns of the $Al_xTi_{1-x}N$ coatings in the as-deposited state (as-dep.) and post-annealed at 500−1200 °C: (A) x=0.8, (B) x=0.7 and (C) x=0.6.

Figs. 5.2, 5.3, and 5.4 show the high-angle annular dark-field scanning transmission electron microscopy (HAADF-STEM) images of c-$Al_xTi_{1-x}N$ coatings with x=0.8, x=0.7, and x=0.6, respectively, in the as-deposited state (A) and after post-annealing at 900°C (B) and at 1000°C (C) for 1 h. The c-$Al_xTi_{1-x}N$ coatings with x=0.8 (Fig. 5.2A) and x=0.7 (Fig. 5.3A) prepared via LP-CVD were composed of c-Al(Ti)N/c-Ti(Al)N nanolamellae with the average compositions of c-$Al_{0.9}Ti_{0.1}N$/c-$Al_{0.6}Ti_{0.4}N$ and c-$Al_{0.8}Ti_{0.2}N$/c-$Al_{0.5}Ti_{0.5}N$, and had the average lamellar periods of 4.7 and 3.5 nm, respectively. The selected area electron diffraction (SAED) patterns in the insets of the HAADF-STEM images (Fig. 5.2A and Fig. 5.3A) revealed that the c-Al(Ti)N/c-Ti(Al)N nanolamellae were modulated along the <100> direction, implying coherent spinodal decomposition of c-$Al_xTi_{1-x}N$ in the as-deposited state. The c-$Al_xTi_{1-x}N$ (x=0.6) coating prepared by PVD possessed nanocolumnar grains with a relatively uniform composition (Fig. 5.4A).

Post-annealing the c-$Al_xTi_{1-x}N$ (x=0.6) coating at 900°C resulted in the precipitation of c-AlN and c-TiN domains (Fig. 5.4B). Furthermore, coarsening of the c-AlN domains and a subsequent transformation into h-AlN were observed at 1000°C (Fig. 5.4C). The c-Al(Ti)N/c-

Ti(Al)N nanolamellar structure remained in the CVD $Al_xTi_{1-x}N$ (x=0.8) coating at 900°C (Fig. 5.2B). However, the nanolamellae vanished at above 1000°C, and an h-AlN diffraction signal can be observed (Fig. 5.2C). On the other hand, the nanolamellar structure for the CVD $Al_xTi_{1-x}N$ (x=0.7) coating was diminished at 900°C (Fig. 5.3B), and the Al(Ti)N domains became coarsened at 1000°C (Fig. 5.3C).

λ_m (extracted by the linear intercepts along the <100> direction using TEM images) is plotted as a function of the post-annealing temperature in Fig. 5.5. λ_m exponentially increased with increasing post-annealing temperature. A linear fit of λ_m in a natural logarithm scale (broken lines) revealed that the slope for $Al_{0.6}Ti_{0.4}N$ is twofold higher than those for $Al_{0.8}Ti_{0.2}N$ and $Al_{0.7}Ti_{0.3}N$, suggesting that the evolution of microstructure in the single-phase c-$Al_xTi_{1-x}N$ (x=0.6) was more sensitive to the post-annealing temperature than in the self-organised nanolamellar-structure in c-$Al_xTi_{1-x}N$ (x=0.7 and 0.8) coatings. The values of λ_0 for the c-$Al_xTi_{1-x}N$ coatings were 0.6, 3.5, and 4.7 nm for x=0.6, 0.7, and 0.8, respectively.

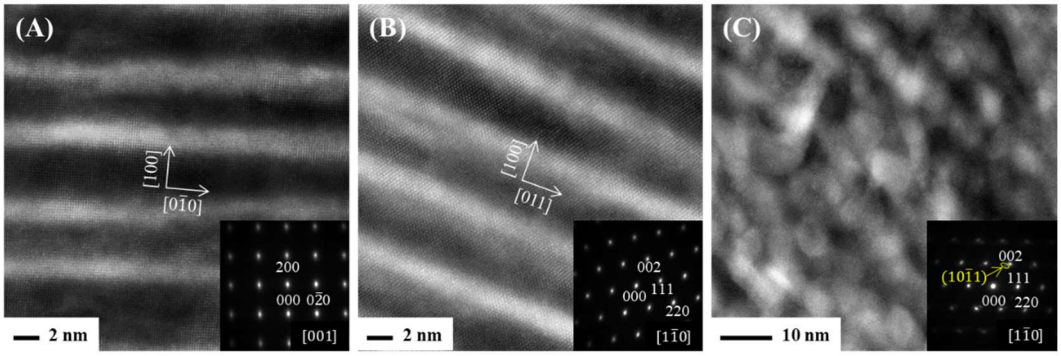

Fig. 5.2. HAADF-STEM images and SAED patterns of $Al_xTi_{1-x}N$ coatings for x=0.8 prepared via LP-CVD: (A) as-deposited, (B) post-annealed at 900℃, and (C) post-annealed at 1000℃.

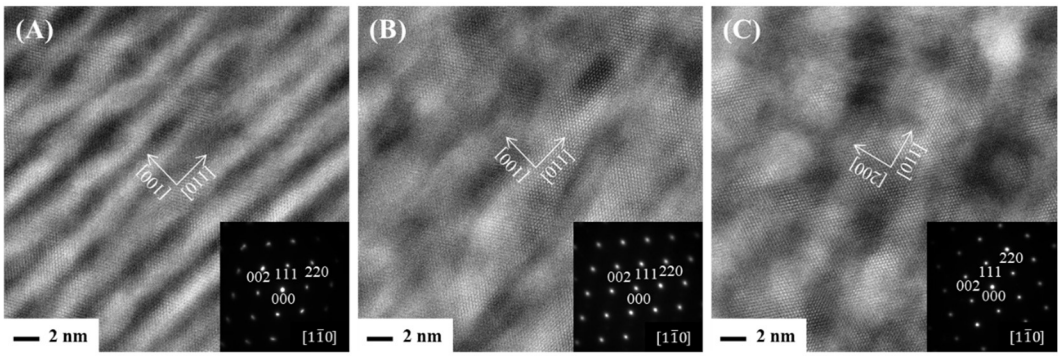

Fig. 5.3 HAADF-STEM images and SAED patterns of $Al_xTi_{1-x}N$ coatings for x=0.7 prepared via LP-CVD: (A) as-deposited, (B) post-annealed at 900℃, and (C) post-annealed at 1000℃.

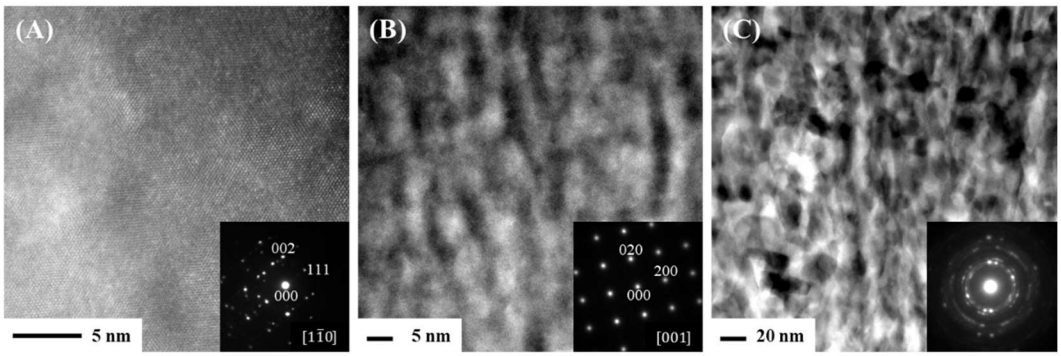

Fig. 5.4 HAADF-STEM images and SAED patterns of $Al_xTi_{1-x}N$ coatings for x=0.6 prepared via arc-evaporated PVD: (A) as-deposited, (B) post-annealed at 900℃ and (C) post-annealed at 1000℃.

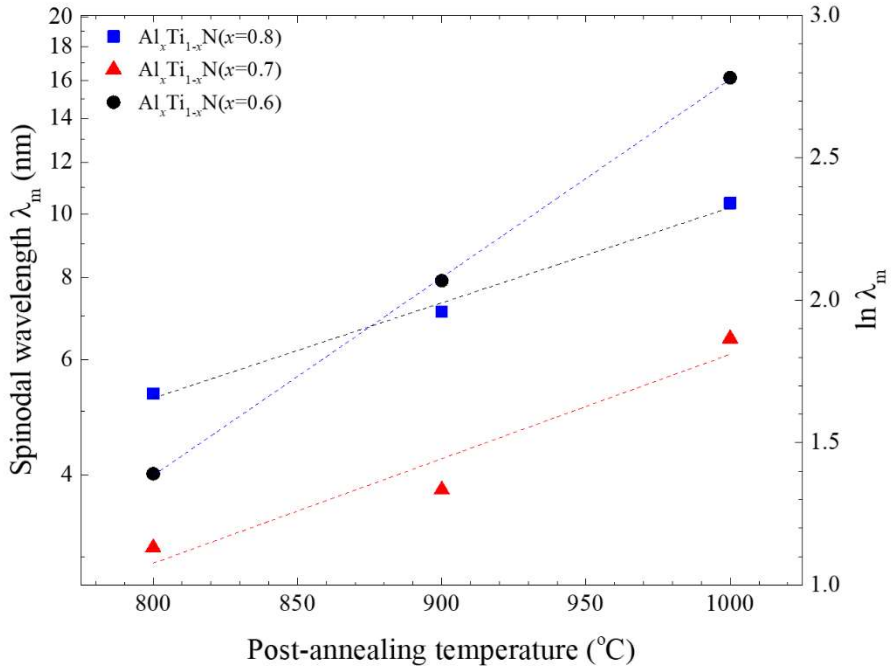

Fig. 5.5 Evolution of the compositional wavelength λ_m of the $Al_xTi_{1-x}N$ coatings as a function of the post-annealing temperature.

Table 5.2 summarises the evolution of λ_m and $\widetilde{D}$ for the coatings post-annealed at 800, 900, and 1000°C for 1 h.

Table 5.2. Summary of the compositional wavelength λ_m and interdiffusion coefficient $\widetilde{D}$ of the $Al_xTi_{1-x}N$ coatings as a function of the annealing temperature.

Temperature (°C)	Compositional wavelength λ_m (nm) / Interdiffusion coefficient $\widetilde{D}$ (m^2/sec)		
	$Al_{0.8}Ti_{0.2}N$	$Al_{0.7}Ti_{0.3}N$	$Al_{0.6}Ti_{0.4}N$
800	5.3 ± 0.9 / 3.7×10^{-23}	3.6 ± 0.3 / 1.2×10^{-23}	4.0 ± 0.7 / 5.0×10^{-22}
900	7.1 ± 0.6 / 1.5×10^{-22}	3.8 ± 0.7 / 2.3×10^{-23}	7.9 ± 0.6 / 2.4×10^{-21}
1000	10.0 ± 1.0 / 1.0×10^{-21}	6.5 ± 0.3 / 5.4×10^{-22}	16.2 ± 1.0 / 1.1×10^{-20}

5.3.2 Mechanical properties of the post-annealed c-$Al_xTi_{1-x}N$ coatings

Fig. 5.6 shows the indentation hardness of the c-$Al_xTi_{1-x}N$ (x=0.8, 0.7, and 0.6) coatings as a function of the post-annealing temperature. The hardness in the c-$Al_xTi_{1-x}N$ (x=0.6) coating increases with the temperature from 600°C onwards, which reveals an age-hardening effect

via spinodal decomposition. The peak hardness of this coating (reached at 800°C) was 39 GPa, which is 5 % higher than that in the as-deposited state, and the hardness rapidly decreased above 900°C. For the c-$Al_xTi_{1-x}N$ (x=0.8 and 0.7) coatings, the hardness started to increase at higher post-annealing temperatures compared to the case of x=0.6. The maximum hardness of 34 GPa was attained at 900°C for x=0.8, and that of 41 GPa was attained at 1000°C for x=0.7. These hardness values were approximately 13 % higher than those in the corresponding as-deposited states. After post-annealing at 1200°C, the hardness of all three $Al_xTi_{1-x}N$ (x=0.8, 0.7, and 0.6) coatings finally dropped to ca. 30 GPa.

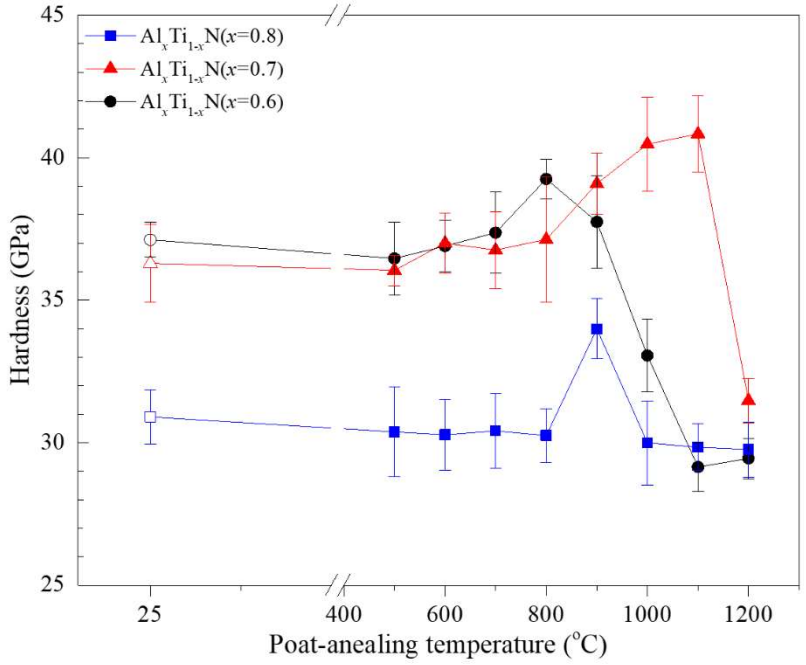

Fig. 5.6. Indentation hardness of $Al_xTi_{1-x}N$ coatings as a function of post-annealing temperature. Open symbol refers to as-deposited state.

5.4. Discussion

5.4.1 Effect of nanostructure on the phase stability in c-$Al_xTi_{1-x}N$ coatings

The c-$Al_xTi_{1-x}N$ coatings with x=0.7 and 0.8 prepared via LP-CVD using $AlCl_3$–$TiCl_4$–NH_3–Ar–H_2 precursor showed higher thermal stability than conventional arced PVD c-$Al_xTi_{1-x}N$ (x=0.6) coating (Fig. 5.1). The plausible reason for the different thermal stabilities is that the coatings with x=0.7 and 0.8 comprised coherent c-Al(Ti)N/c-Ti(Al)N nanolamellae with Al

concentration fluctuating along the <100> direction. This structure is considered to minimise the total free energy for microstructure formation [29] compared to the single-phase of c-$Al_xTi_{1-x}N$ (x=0.6) (Fig. 5.4). Previous reports [7, 23–24] also suggested that the multilayer c-AlTiN/c-TiAlN coating possesses higher thermal stability than single-phase c-AlTiN.

Recently, metastable c-$Al_xTi_{1-x}N$ coatings with x>0.66 have been prepared via LP-CVD in industrial plants using a precursor system based on $AlCl_3$–$TiCl_4$–NH_3–H_2 [13, 25–27]. The c-$Al_xTi_{1-x}N$ coatings with x=0.7–0.8 were found to be composed of spontaneously formed coherent c-Al(Ti)N/c-Ti(Al)N nanolamellae with Al concentration fluctuating along the <100> direction [13, 25]. These unique structures arise via a spinodal decomposition process [28]. The spinodal decomposition occurs without nucleation and facilitates the minimization of the total free energy (ΔG_{sys}), which can be written as follows:

$$\Delta G_{sys} = \Delta G_{chem} + E_{surf} + E_{str} \quad Eq.(5.2)$$

where ΔG_{chem} is the (positive) chemical energy that is the driving force for phase separation, E_{surf} is the interfacial energy, and E_{str} is the elastic strain energy [29].

Assuming the c-$Al_xTi_{1-x}N$ is a quasibinary c-TiN-c-AlN system, the ΔG_{chem} values extracted using first-principles calculations from 700 to 900°C are approximately 22, 20, and 18 kJ/mol for x=0.6, 0,7, and 0.8, respectively [30]. E_{surf} for a coherent interphase (x=0.7 and 0.8) is known to be only 1/10–1/3 the value of that for an incoherent interphase (x=0.6) [31]. The values of E_{str} for x=0.7 and 0.8 are also lower, owing to the compositional fluctuation along the elastically soft <100> direction [32]. Therefore, ΔG_{sys} of the self-organised nanolamellae structure in c-$Al_xTi_{1-x}N$ coating with x=0.8 (Fig. 5.2) and 0.7 (Fig. 5.3) is lower (i.e., thermodynamically more stable) than that of the single-phase c-$Al_xTi_{1-x}N$ coating with x=0.6 (Fig. 5.4). Furthermore, the transformation of AlTiN from the metastable cubic phase to the equilibrium two-phase (h-AlN and c-TiN) structure is correlated with the coarsening of the c-AlN domains [33]. Norrby et al. [15] studied the transformation of c-AlN to h-AlN in $Al_{0.64}Ti_{0.36}N$ and $Al_{0.45}Ti_{0.55}N$, suggesting that the transformation rate increases with the Al content. In a homogeneous c-$Al_xTi_{1-x}N$ system, an increase in x will indeed shorten the diffusion length to initiate the phase transformation. However, the temperature to initiate the cubic-to-

hexagonal phase transformation is ~100°C higher for the CVD $Al_{0.8}Ti_{0.2}N$ and $Al_{0.7}Ti_{0.3}N$ than for PVD $Al_{0.6}Ti_{0.4}N$ (Fig. 5.1). The plausible reason is that the Al-rich c-$Al_xTi_{1-x}N$ coatings prepared via CVD inherently have a lower density of defects than the arced PVD coating. The defect density can be estimated by the slope in λ_m with the post-annealing temperature (Fig. 5.5) and the magnitude of $\widetilde{D}$ in Table 5.2.

5.4.2 Age hardening in c-$Al_xTi_{1-x}N$ coatings

The compositional wavelength caused by spinodal decomposition is theoretically invariant with regard to the post-annealing time [28]. Indeed, changes in this wavelength with time were found to be extremely small for many alloys [31]. The hardening effect by spinodal decomposition is considered to be a result of the transformation of c-$Al_xTi_{1-x}N$ to c-AlN and c-TiN, increasing the elastic energy and gradient energy [34].

There have been several reports suggesting an increase in the hardness of c-AlTiN coatings via spinodal decomposition [3, 12]. The hardness increase compared to the as-deposited state is up to 7 %, which agrees with the value of 5 % found for the single-phase c-$Al_xTi_{1-x}N$ (x=0.6) coating (Fig. 5.6). On the other hand, the increase in hardness for the self-organised nanolamellae in c-$Al_xTi_{1-x}N$ (x=0.7 and 0.8) is as high as 13 %. One possible explanation is that the hardening effect is due to an increase in the coherent interfacial energy generated during nanolamellae decomposition (Fig. 5.3). A similar trend was reported by Todt et al., who observed an age-hardening effect of approximately 7 % in LP-CVD $Al_{0.95}Ti_{0.05}N$ with h-AlN/c-TiN nanolamellae structure when annealed at 800–900 °C [26].

5.5. Summary

The findings of this study are summarised as follows:

1. Al-rich c-$Al_xTi_{1-x}N$ (x=0.7 and 0.8) coatings prepared via LP-CVD comprising a self-organised nanolamellar structure were found to have good thermal stability comparable to the single-phase c-$Al_xTi_{1-x}N$ (x=0.6) coating prepared via PVD. The reason is that the coherent c-Al(Ti)N/c-Ti(Al)N nanolamellae generated via spinodal decomposition have a lower free energy (thermodynamically more stable) compared to the single-phase c-AlTiN coating. The value of $\widetilde{D}$ extracted from λ_m is lower for the c-$Al_xTi_{1-x}N$ (x=0.7 and 0.8)

coatings annealed at 800 to 1000°C than that of c-$Al_xTi_{1-x}N$ (x=0.6). The lower $\widetilde{D}$ results in a slower c-AlN to h-AlN transformation.

2. The age hardening effect appears at higher temperature for the c-$Al_xTi_{1-x}N$ (x=0.8 and 0.7) coatings than for the x=0.6 coating prepared by PVD, with the peak hardness located at 900, 1000, and 800°C, respectively. The shift of maximal hardness from 800 to 1000°C is attributed to the spinodal hardening and the increased coherent interfacial energy during nanolamellar decomposition.

3. The c-$Al_xTi_{1-x}N$ (x=0.8 and 0.7) coatings exhibit high thermal stability and hardness at elevated temperatures. This is expected to lead to better performance in dry cutting and at high cutting speeds. An evaluation of the cutting performance of these new coatings is under way, as well as the development of mass production process for milling applications.

References in chapter 5

[1] O. Knotek, T. Leyendecker, J. Solid State Chem. 70 (1987) 318−322.

[2] W.D. Münz, J. Vac. Sci. Technol., A 4 (1986) 2717−2725.

[3] P.H. Mayrhofer, A. Hörling, L. Karlsson, J. Sjölén, T. Larsson, C. Mitterer, L. Hultman, Appl. Phys. Lett. 83 (2003) 2049−2051.

[4] G. Erkens, R. Cremer, T. Hamoudi, K.-D. Bouzakis, I. Mirisidis, S. Hadjiyiannis, G. Skordaris, A. Asimakopoulos, S. Kombogiannis, J. Anastopoulos, K. Efstathiou, Surf. Coat. Technol. 177-178 (2004) 727−734.

[5] K. Yamamoto, J. High Temp. Soc. 33 (2007) 84−89.

[6] M. Setoyama, A. Nakayama, M. Tanaka, N. Kitagawa, T. Nomura, Surf. Coat. Technol. 86-87 (1996) 225−230.

[7] L. Chen, Y.X. Xu, Y. Du, Y. Liu, Thin Solid Films 592 (2015) 207−214.

[8] I. Tsutomu, S. Hiroshi, Thin Solid Films 195 (1991) 99−110.

[9] J. Vetter, Surf. Coat. Technol. 76 (1995) 719−724.

[10] K. Macák, V. Kouznetsov, J. Schneider, U. Helmersson, I. Petrov, J. Vac. Sci. Technol., A 18 (2000) 1533−1537.

[11] J.S.A. Horling, L. Karlsson, J. Vac. Sci. Technol., A 20 (2002) 1815−1823.

[12] A. Hörling, L. Hultman, M. Odén, J. Sjölén, L. Karlsson, Surf. Coat. Technol. 191 (2005) 384−392.

[13] A. Paseuth, K. Yamagata, A. Miura, M. Higuchi, K. Tadanaga, J. Am. Ceram. Soc. 100 (2016) 343−353.

[14] R. M'Saoubi, S. Ruppi, CIRP Ann. Manuf. Technol. 58 (2009) 57−60.

[15] N. Norrby, L. Rogström, M.P. Johansson-Jõesaar, N. Schell, M. Odén, Acta Mater. 73 (2014) 205−214.

[16] A. Knutsson, J. Ullbrand, L. Rogström, N. Norrby, L. Johnson, L. Hultman, J. Almer, M.J. Jöesaar, B. Jansson, M. Odén, J. Appl. Phys. 113 (2013) 2135181.

[17] R. Hollerweger, H. Riedl, J. Paulitsch, M. Arndt, R. Rachbauer, P. Polcik, S. Primig, P. Mayrhofer, Surf. Coat. Technol. 257 (2014) 78−86.

[18] I. Krajinović, W. Daves, M. Tkadletz, T. Teppernegg, T. Klünsner, N. Schalk, C. Mitterer, C. Tritremmel, W. Ecker, C. Czettl, Surf. Coat. Technol. 304 (2016) 134−141.

[19] A. Paseuth, H. Fukui, S. Okuno, H. Kanaoka, Y. Okada, Surf. Coat. Technol. 260 (2014) 139−147.

[20] C.A. Schneider, W.S. Rasband, K.W. Eliceiri, Nat. Methods 9 (2012) 671−675.

[21] A. Einstein, Ann. Phys. 17 (1905) 549−560.

[22] W.C. Oliver, G.M. Pharr, J. Mater. Res. 19 (2004) 3–20.

[23] M. Setoyama, M. Irie, H. Ohara, M. Tsujioka, Y. Takeda, T. Nomura, N. Kitagawa, Thin Solid Films 341 (1999) 126−131.

[24] A. Knutsson, M.P. Johansson, L. Karlsson, M. Odén, J. Appl. Phys. 108 (2010) 0443121.

[25] J. Zalesak, J. Todt, R. Pitonak, A. Kopf, R. Weissenbacher, B. Sartory, M. Burghammer, R. Daniel,J. Keckes, J. Appl. Crystallogr. 49 (2016) 2217−2225.

[26] J. Todt, J. Zalesak, R. Daniel, R. Pitonak, A. Köpf, R. Weißenbacher, B. Sartory, C. Mitterer, J. Keckes, Surf. Coat. Technol. 291 (2016) 89–93.

[27] A. Köpf, J. Keckes, J. Todt, R. Pitonak, R. Weissenbacher, Mater. Sci. Forum 62 (2015) 219−224.

[28] J.W. Cahn, Acta Metall. 10 (1962) 179−183.

[29] T. Miyazaki, Mater. Jpn. 53 (2014) 363−369.

[30] P.H. Mayrhofer, F.D. Fischer, H.J. Bohm, C. Mitterer, J. M. Schneider, Acta Mater. 55 (2007) 1441−1446.

[31] T. Miyazaki, Mate. Jpn. 53 (2014) 419−426.

[32] F. Tasnádi, I.A. Abrikosov, L. Rogström, J. Almer, M.P. Johansson, M. Odén, Appl. Phys. Lett. 97 (2010) 2319021.

[33] A. Hörling, L. Hultman, M. Odén, J. Sjölén, L. Karlsson, J. Vac. Sci. Technol., A 20 (2002) 1815−1823.

[34] L. Rogström, J. Ullbrand, J. Almer, L. Hultman, B. Jansson, M. Odén, Thin Solid Films 520 (2012) 5542−5549.

Chapter 6. Thermal durability and cutting performance of Al-rich $Al_xTi_{1-x}N$ coating prepared by low-pressure chemical vapour deposition

6.1. Introduction

Due to their outstanding elevated hardness and oxidation resistance, cubic (c-) $Al_xTi_{1-x}N$ coatings have been extensively studied among transition metal nitrides for wear protection in the cutting tool industry [1–3]. Further enhancements in the performance of hard coatings are very desirable for dry cutting and higher cutting speeds with a lower cost and reduced environmental impact. The standard industrial techniques for fabricating c-$Al_xTi_{1-x}N$ is physical vapour deposition (PVD) [4–6], and the maximum aluminium content (x) is limited to <0.67 to maintain a metastable cubic structure. Higher values of x result in a mixture of cubic and hexagonal (h-) AlN phases [7], which degrades the mechanical properties [8]. Recently, we successfully synthesised c-$Al_xTi_{1-x}N$ coatings with the average composition of x = 0.7–0.8 via low-pressure chemical vapour deposition (LP-CVD) in an industrial plant using the $AlCl_3$–$TiCl_4$–NH_3–Ar–H_2 precursor system [9]. Moreover, after a constant period of post-annealing, these coatings showed higher thermal stability compared to c-$Al_xTi_{1-x}N$ ($x \approx 0.6$) produced by PVD [10]. This outstanding thermal stability was attributed to the free energy minimisation via self-organised c-Al(Ti)N/c-Ti(Al)N nanolamellae structure formed in the as-deposited state. However, the effect of annealing time on the thermal and mechanical properties of this new coating has not been examined, even though hard coatings in tool applications are usually exposed to temperatures above 800°C for prolonged time during cutting operations [11–13].

In this study, we investigate the thermal stability of the Al-rich c-$Al_xTi_{1-x}N$ coating, and test its feasibility for use in high-speed and dry cutting applications. The c-$Al_xTi_{1-x}N$ coating with the average composition of $x \approx 0.8$ and a reference (c-$Al_xTi_{1-x}N$ coating with $x \approx 0.6$ produced via arc PVD) were first post-annealed at 800–1200°C for 1–10 h in Ar gas atmosphere. The phase stability of post-annealed sample coatings were analysed using X-ray diffraction (XRD), and their microstructural evolutions were observed by transmission electron microscopy. Furthermore, the hardness after different annealing times was measured, and

a cutting test using cast iron (JIS: FCD700) was conducted to evaluate the mechanical properties. Finally, tool inserts consisting of the Al-rich c-$Al_xTi_{1-x}N$ ($x \approx 0.8$) prepared by LP-CVD were tested for machining automotive components, and the performance was compared to that of commercially available CVD- and PVD-based coating inserts.

6.2. Experimental procedures

c-$Al_xTi_{1-x}N$ coating with an average aluminium content $x \approx 0.8$ and comprised of c-Al(Ti)N/c-Ti(Al)N nanolamellae (lamellar period ≈ 4 nm) was deposited using a commercially available hot-wall LP-CVD reactor with an $AlCl_3$–$TiCl_4$–NH_3–Ar–H_2 precursor system. WC–5wt% Co substrates (SNMA 120408; Sumitomo Electric Hardmetal Corp., Hyogo, Japan) with mirror-polished surfaces were used to analyse the physical properties of the coating. The substrates were centrally loaded in a coating batch, as described in related work [14]. A TiN base layer with an average thickness of 0.5 µm was deposited together with a 2.0-µm-thick TiC_xN_{1-x} bonding layer to guarantee adhesion between the coating and the carbide substrate. The CVD deposition conditions can be found in Ref. 9.

Post-annealing was carried out at 800°C to 1200°C in steps of 100°C and durations of 1, 5, and 10 h in a protective argon atmosphere at ambient pressure using heat-treatment furnaces (PHSG; Shimadzu Mectem, Inc., Shiga, Japan). The heating rate was fixed at 10°C/min, and the sample after heat treatment was rapidly cooled to room temperature in approximately 0.5 h. The thermal stability of the c-$Al_xTi_{1-x}N$ ($x \approx 0.8$) coating was compared with that of a 3-µm-thick arc-evaporated PVD c-$Al_xTi_{1-x}N$ ($x \approx 0.6$) coated on cement carbide substrate (Sumitomo Electric Hardmetal Corp., Hyogo, Japan).

The phase analysis was conducted by XRD (RIGAKU, Tokyo, Japan, SmartLab; 45 kV, 200 mA, Cu-Kα radiation) in the grazing incidence geometry (angle of incidence: 2°). The microstructures of the as-deposited and post-annealed samples were evaluated using high-resolution transmission electron microscopy (HRTEM; JEM-2100F, JEOL, Tokyo, Japan) with energy-dispersive X-ray spectroscopy (EDX; JED-2300, JEOL) for elemental analysis. Cross-sectional TEM samples were prepared by using a focused ion beam (FIB; JIB-4501; JEOL Tokyo, Japan) with Ga^+ beam milling (accelerating voltage: 30 kV).

The hardness was measured by a nanoindentation tester (ENT-1100a; Elionix, Tokyo,

Japan) using a Berkovich diamond-shaped tip indenter. The indentation test was performed at 10 locations over the smoothed surface with a load of 30 mN. The indentation hardness was analysed using the Oliver and Pharr method [15], and the average value and standard deviation were extracted to characterise the coating hardness. More details about the physical and chemical evaluations can be found in related works [9,10].

The wear resistance of the Al-rich c-$Al_xTi_{1-x}N$ ($x \approx 0.8$) coating prepared by LP-CVD was compared to that of arced PVD c-$Al_xTi_{1-x}N$ ($x \approx 0.6$) and moderated temperature (MT)- CVD TiCN/α-Al_2O_3 coatings for the dry milling operation of ductile cast iron blocks (JIS:FCD700). The progress of flank wear as a function of the metal removal amount (Q) was measured with an optical microscope, and the tool life was defined by an average flank wear (Vb) = 0.15 mm. In order to eliminate the effects of the carbide substrate, the insert's geometry, and cutting-edge preparation on the tool life, a WC−9wt% Co cemented carbide substrate and SEET13T3AGSN-G type geometry (Sumitomo Electric Hardmetal Corp., Hyogo, Japan) with an edge-honing amount of 30 μm were used for all cutting inserts. The detailed cutting conditions used in this study are provided in Table 6.1. Furthermore, the inserts coated with TiN (0.5 μm)/TiCN (2 μm)/c-$Al_{0.8}Ti_{0.2}N$ (3 μm) were used for machining automotive components, and the performance was compared to that of the commercially available TiN (0.5 μm)/TiCN (2 μm)/α-Al_2O_3 (3 μm) MT-CVD-coated inserts (ACK200; Sumitomo Electric Hardmetal Corp., Hyogo, Japan) and AlTiCrN (5 μm) PVD-coated inserts (ACK300; Sumitomo Electric Hardmetal Corp., Hyogo, Japan), with the detailed cutting conditions listed in Table 6.2.

Table 6.1 Conditions for cast iron blocks

Definitions	**Machining conditions**
Component	Block
work material	JIS:FCD700
Tool/Insert	WGC4160/SEET13T3AGSN-G
cutting speed Vc (m/min)	150
feed speed Vf (mm/min)	60
feed per tooth fz (mm/tooth)	0.2
number of tooth Z (tooth)	1
radial depth of cut ae (mm)	100
axial depth of cut ap (mm)	2
Environment	Dry cutting

Table 6.2 Cutting conditions for automotive components

Definitions	**Machining conditions**	
Component	Trailing arm	Cylinder block
work material	JIS:FCD450	JIS:FC250
Tool	DPG4000	WEX3000
Insert	SPG120408	AXMT170508PEER-G
cutting speed Vc (m/min)	500	200
feed speed Vf (mm/min)	2860	1400
feed per tooth fz (mm/tooth)	0.18	0.07
number of tooth Z (tooth)	6	5
radial depth of cut ae (mm)	40	50
axial depth of cut ap (mm)	2	0.5
Environment	Dry cutting	Wet cutting

6.3. Results

6.3.1. Thermal and microstructural evolutions

Fig. 6.1 shows the XRD patterns of c-$Al_xTi_{1-x}N$ coatings before and after post-annealing at 800–1200°C for 1–10 h (vertical axixes indicated in log scale). The coating with $x \approx 0.8$ (Fig. 6.1A) was completely stable up to 1000°C for 1 h. Post-annealing at 1000°C for 5 h revealed a weak signal at 2θ = 33°, indicating the beginning of transformation to the h-AlN phase. The c-AlN was converted to the h-AlN phase after heating at 1200°C for 1 h. On the other hand, for c-$Al_xTi_{1-x}N$ with $x \approx 0.6$ (Fig. 6.1B), the h-AlN phase first appeared after post-annealing at 900°C for 5 h, and the cubic-to-hexagonal AlN phase transition was almost complete at 1000°C after 1 h. Furthermore, peak broadening (2θ ≈ 44°) appeared in Figs. 6.1A and 6.1B after heating at 900°C and 800°C for 1 h, respectively. This indicated the spinodal decomposition in c-$Al_xTi_{1-x}N$ ($x \approx 0.8$ and 0.6) coatings.

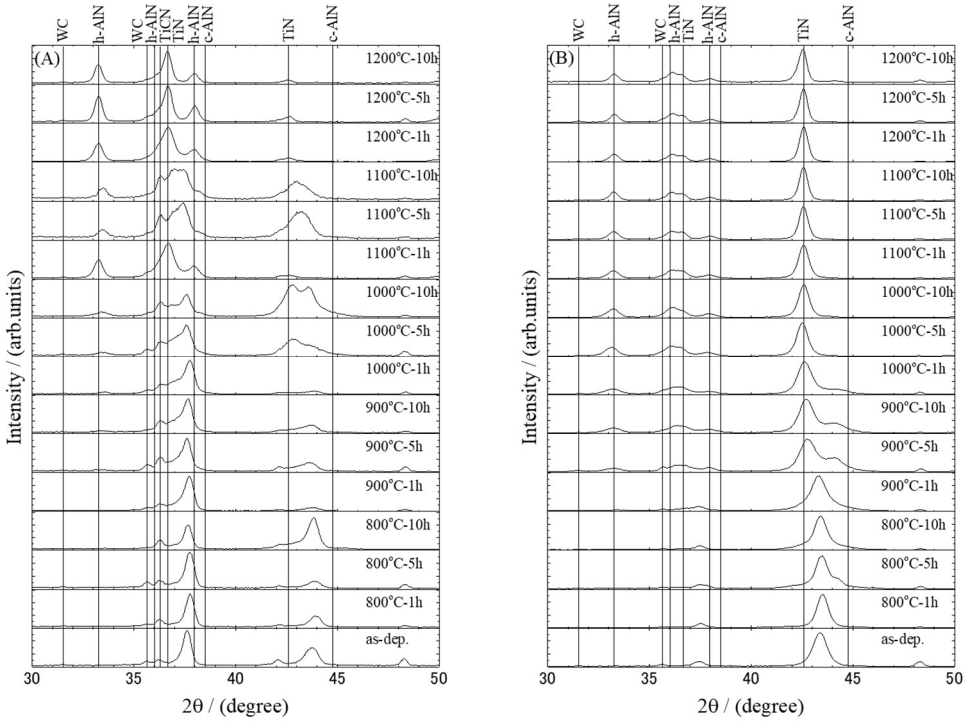

Fig. 6.1 XRD patterns of $Al_xTi_{1-x}N$ coatings post-annealed at 800 to 1200°C and for 1 to 10 h. (A) $Al_xTi_{1-x}N$ ($x \approx 0.8$) and (B) $Al_xTi_{1-x}N$ ($x \approx 0.6$).

Figs. 6.2–6.3 show the high-angle annular dark-field scanning transmission electron microscopy images for c-$Al_xTi_{1-x}N$ coatings with $x \approx 0.8$ (Fig. 6.2) and $x \approx 0.6$ (Fig. 6.3),

respectively. The difference in contrast represents the difference in the atomic weight of the elements constituting the coatings. Heavy elements (Ti-rich phase) appear bright and light elements (Al-rich phase) appear dark. Chemical composition analysis using EDX was performed perpendicular to the modulation direction of the nanolamellae in c-$Al_xTi_{1-x}N$ coating with $x \approx 0.8$ prepared by LP-CVD. The average composition of the nanolamellae was c-$Al_{0.9}Ti_{0.1}N$/c-$Al_{0.6}Ti_{0.4}N$ with the lamellar period ≈ 4 nm. The selected area electron diffraction (SAED) patterns in the insets of Figs. 6.2A−D revealed that the c-Al(Ti)N/c-Ti(Al)N nanolamellae were modulated along the <100> direction, implying the coherent spinodal decomposition in the as-deposited state. The nanolamellae interface slightly changed (interface boundary became ambiguous) after heating for 1 h (Fig. 6.2B). The coalescence of lamellae boundary appeared after 5 h of heating (Fig. 6.2C). Despite the annihilation of nanolamellae structures after 10 h of annealing, the SAED results confirmed that no h-AlN phase was formed in this temperature regime (Fig. 6.2D).

On the other hand, the monolithic c-$Al_xTi_{1-x}N$ with $x \approx 0.60$ (Fig.6.3) coating prepared by PVD is comprised of fine columnar grains with uniform aluminium concentration (Fig. 6.3A). Post-annealing at 800°C for 1 h resulted in the precipitation of c-AlN and c-TiN domains due to spinodal decomposition (Fig. 6.3B). Furthermore, coarsening of the c-AlN domains and a subsequent transformation into h-AlN were observed after 1 h (Fig. 6.3C) and 10 h (Fig. 6.3D) of 900°C heating, respectively.

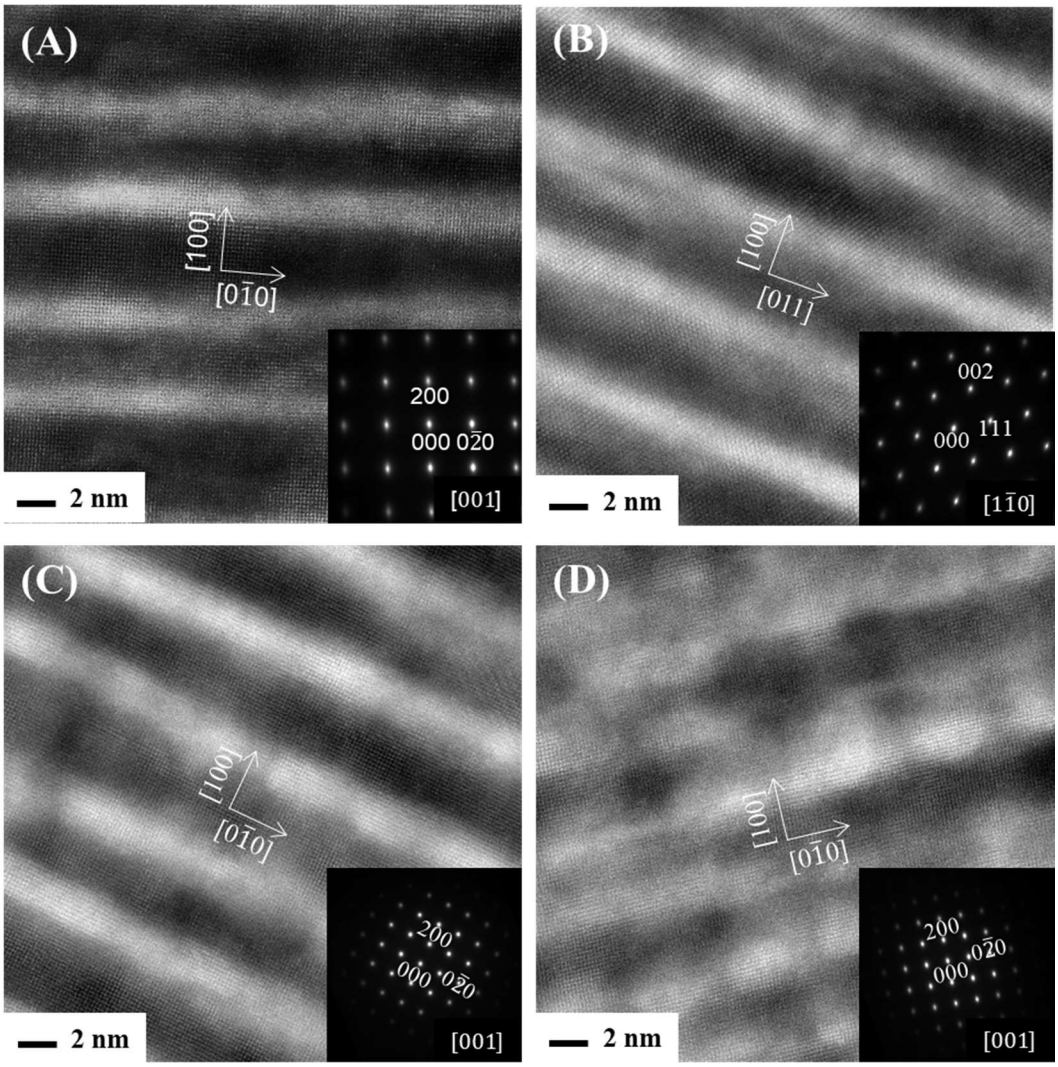

Fig. 6.2 TEM microscopic images and SAED patterns (insets) of $Al_xTi_{1-x}N$ ($x \approx 0.8$) samples prepared by LP-CVD. (A) as-deposited and (B) post-annealed at 900℃ for 1 h, (C) 5 h, and (D) 10 h.

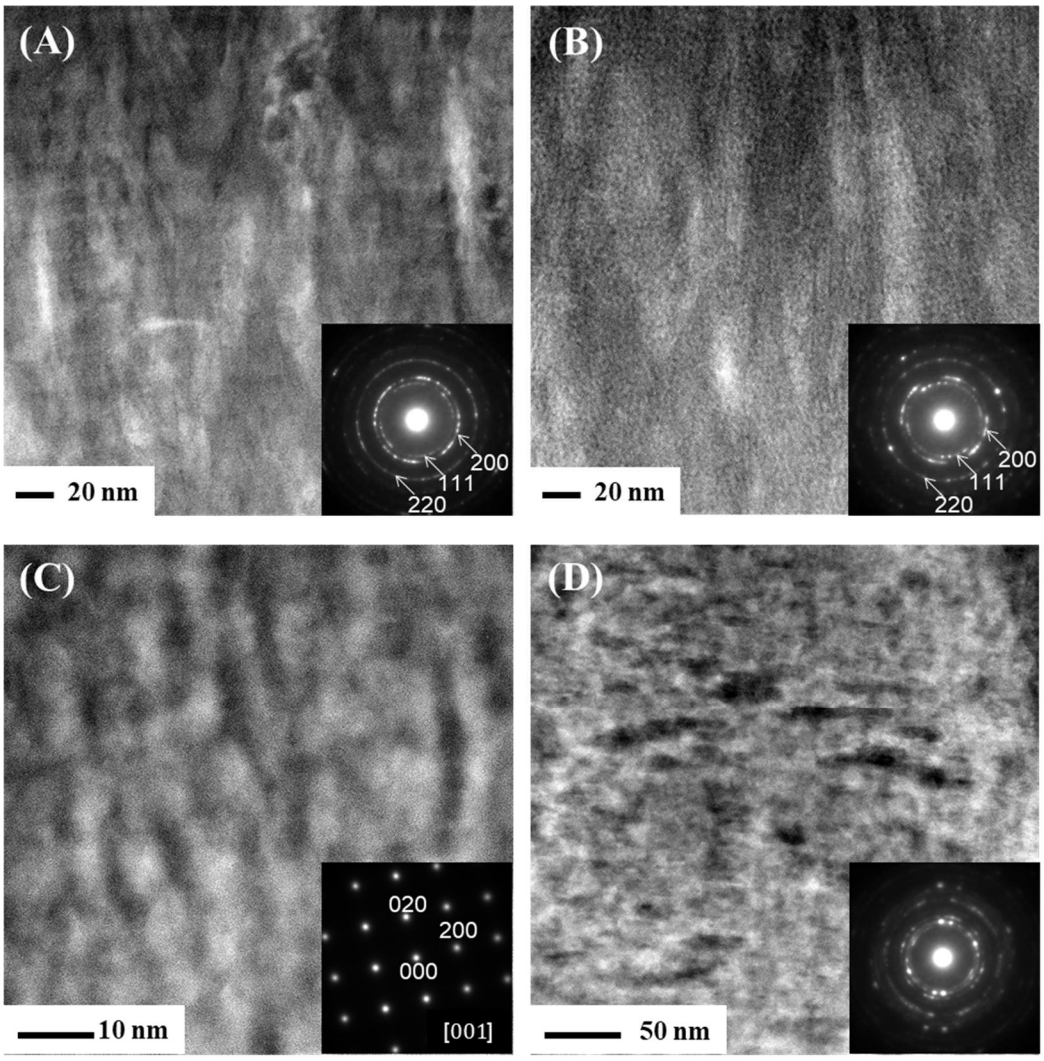

Fig. 6.3 TEM microscopic images and SAED patterns (insets) of $Al_xTi_{1-x}N$ ($x \approx 0.6$) samples prepared by arced PVD. (A) as-deposited and (B) post-annealed at 800℃ for 1 h, (C) post-annealed at 900℃ for 1 h, and (D) 10 h.

6.3.2. Mechanical properties and cutting performances

The indentation hardness of c-$Al_xTi_{1-x}N$ coatings with $x \approx 0.8$ and 0.6 are respectively shown in Figs. 6.4A and 6.4B, both before and after post-annealing between 800–1200°C for different times. The average hardness of the sample with $x \approx 0.6$ increased from 37 GPa in the as-deposited state to a peak value of 39 GPa after post-annealing at 800°C for 1 h, which is due to the age-hardening effect via spinodal decomposition (Fig. 6.4B). Increasing the annealing time gradually reduced the hardness, implying defect annihilation and coarsening of the Al-rich c-AlN domain. The hardness drastically decreased above 900°C due to the c-AlN-to-h-AlN phase transformation and releasing of compressive residual stress from as-deposited state. On the other hand, age hardening in the sample with $x \approx 0.8$ (Fig. 6.4A) after 1 h appeared at higher post-annealing temperatures (ca. 1000–1100°C) compared to that with $x \approx 0.6$. The maximum hardness was observed at 41 GPa after post-annealing the $x \approx 0.8$ sample at 1100°C for 1 h. Increasing the annealing time to 10 h lowered the hardness to 36 GPa, which is nevertheless still comparable to the as-deposited state.

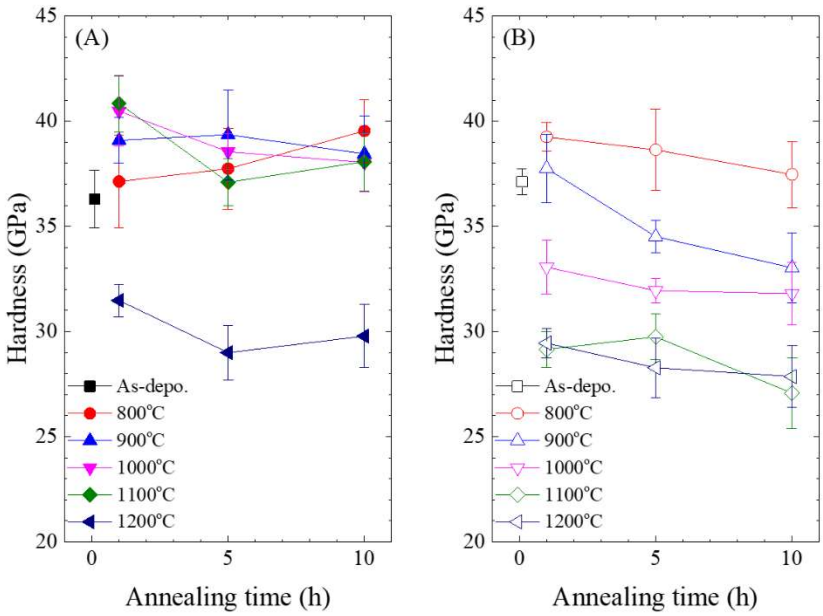

Fig. 6.4 Hardness evolution of $Al_xTi_{1-x}N$ coatings after post-annealed at 800–1200°C for 1–10 h. (A) $x \approx 0.8$ and (B) $x \approx 0.6$.

Fig. 6.5 shows the results of dry milling test, which used ductile cast iron block (JIS:FCD700) to evaluate the cutting performance of the Al-rich c-$Al_xTi_{1-x}N$ (x = 0.8, (A)) in comparison with arced PVD c-$Al_xTi_{1-x}N$ (x = 0.6, (B)) and MT-CVD TiCN/α-Al_2O_3 (C) coatings. The Al-rich c-$Al_xTi_{1-x}N$ ($x \approx 0.8$) coating exhibited superior wear resistance: the average flank wear (Vb) was suppressed; and the metal removal amount increased by factors of 3 and 2 compared to those of the PVD- and CVD-derived coatings, respectively. Fig. 6.6 shows the field cutting performance of c-$Al_xTi_{1-x}N$ (x = 0.8) coating inserts prepared via LP-CVD versus commercially available MT-CVD TiCN/α-Al_2O_3 (Fig. 6.6A) and arced PVD AlTiCrN (Fig. 6.6B) coatings. Even when dry milling ductile cast iron component (trailing arm; JIS: FCD450) at high cutting speed, it was possible to obtain a doubled tool life compared to conventional CVD coating with the new coating material. Moreover, wet milling using grey cast iron component (cylinder block; JIS: FC250) dramatically increased the tool life (by 10 times), indicating high thermal shock resistance of the new coating compared with state-of-the-art PVD coating.

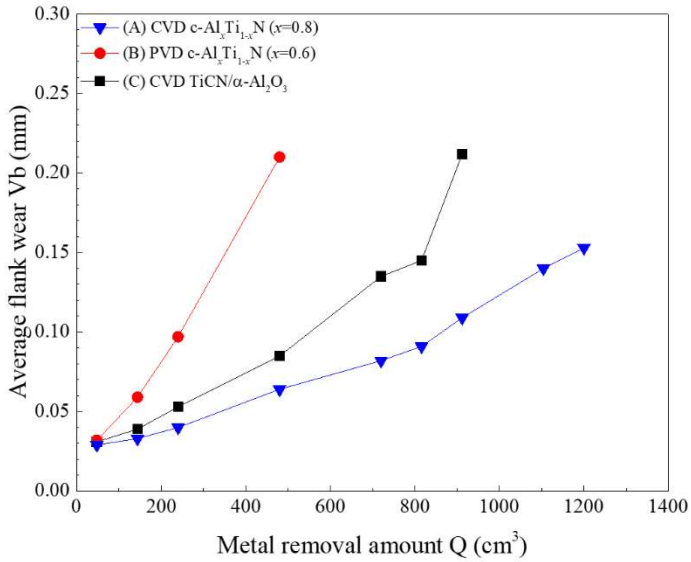

Fig. 6.5 Dry milling test using a ductile cast iron block (JIS:FCD700): (A) $Al_xTi_{1-x}N$ ($x \approx 0.8$) prepared by LP-CVD, (B) $Al_xTi_{1-x}N$ ($x \approx 0.6$) prepared by arced PVD, and (C) MT-CVD coated TiCN/α-Al_2O_3.

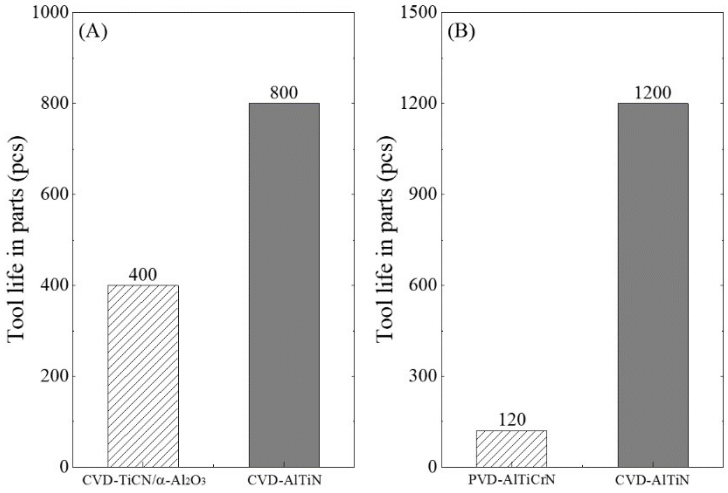

Fig. 6.6 Field test results of $Al_xTi_{1-x}N$ ($x \approx 0.8$) coating insert prepared by LP-CVD in comparison with: (A) CVD-coated TiCN/α-Al_2O_3 after high speed and dry milling of ductile cast iron (trailing arm; JIS:FCD450) and (B) PVD-coated AlTiCrN after wet milling of grey cast iron (cylinder block; JIS:FC250).

6.4. Discussion

6.4.1. Relation between phase stability and nanostructure of c-$Al_xTi_{1-x}N$ coatings

The Al-rich c-$Al_xTi_{1-x}N$ (average $x \approx 0.8$) coating prepared via LP-CVD using $AlCl_3$-$TiCl_4$-NH_3-Ar-H_2 precursor showed not only superior thermal stability (Fig. 6.1), but also a delaying microstructural evolution at elevated temperatures (Figs. 6.2−6.3). The likely cause of the improvement is the coherent c-Al(Ti)N/c-Ti(Al)N nanolamellae spontaneously formed along the <100> direction. This unique nanostructure is considered to arise via a spinodal decomposition process [16]. Such nanolamellae can minimise the system's free energy, leading to higher thermal stability than monolithic c-AlTiN [17]. This kind of template effect can be exploited to increase the structural and thermal stability of c-$Al_xTi_{1-x}N$ cubic phases with high x values. Setoyama et al. indicated that an arc-evaporated c-AlN/c-TiN superlattice coating, which had a superlattice period of below 3 nm, could remain metastable at 1000°C for 3.5 h [18]. Knutsson [19] also reported the delayed c-AlN-to-h-AlN phase transformation in c-$Ti_{0.34}Al_{0.66}N$/c-TiN multilayer coatings in comparison with monolithic c-$Ti_{0.34}Al_{0.66}N$ prepared via reactive cathodic arc evaporation. Moreover, the c-AlN-to-h-AlN phase transformation is correlated with the coarsening of the c-AlN domains, which is governed by

a diffusion process [7]. Using the change in inter-domain distance according to previous work [10], the estimated diffusion coefficient is 1–2 order lower in magnitude in LP-CVD c-$Al_xTi_{1-x}N$ ($x \approx 0.8$) coating compared to that of arced PVD c-$Al_xTi_{1-x}N$ ($x \approx 0.6$). This is also believed to increase the thermal stability of the former.

6.4.2. Mechanical property and cutting performance of c-$Al_xTi_{1-x}N$ coatings

It is well-accepted that heating c-$Al_xTi_{1-x}N$ coatings from the as-deposited state increases their hardness via spinodal decomposition [3, 8]. A higher x in metastable c-$Al_xTi_{1-x}N$ resulted in more increase in hardness (Fig. 6.4). One plausible reason is the increased micro-strain during c-AlN and c-TiN phase separation [20, 21]. The increasing rate of hardness between the as-deposited and post-anealed state in_c-$Al_xTi_{1-x}N$ ($x \approx 0.8$) was 13 % (from 36 to 41 GPa), higher than the increase rate in c-AlxTi1–xN (x ≈ 0.6) around 5 % (from 37 to 39 GPa). The reason for the higher increasing rate of hardness is considered not only due to age hardening effect by spinodal decomposition, but also the increase of strain generated during nanolamellar decomposition (Fig. 6.2). A similar trend was reported by Todt et al., who observed an age-hardening effect in w-AlN/c-TiN nanolamellar-structured $Al_{0.95}Ti_{0.05}N$ when annealing in the range of 800–900°C [22].

The cast iron block (JIS: FCD700) dry-milling results indicated significantly higher wear resistance of c-$Al_xTi_{1-x}N$ ($x \approx 0.8$) in comparison with the state-of-the-art PVD c-$Al_xTi_{1-x}N$ (x = 0.6) and CVD TiCN/α-Al_2O_3 coating inserts (Fig. 6.5). Since ductile cast iron is a high strength metal which consists abrasive hard particles (e.g. cementite (Fe3C) and spheroidal graphite), hard coatings having high thermal stability and low hardness degradation at elevated temperature are considered to benefit for dry cutting. Thus the superior wear resistance of c-$Al_xTi_{1-x}N$ ($x \approx 0.8$) is considered due to the improvement in thermal stability (Fig. 6.1). Furthermore, the increase of hardness above 900°C (Fig. 6.4) is supposed to suppress the hardness reduction during the cutting operation, at which temperature (>800°C) [11, 12, 13] α-Al_2O_3 is known to become softer [23]. Furthermore, the improvements in thermal stability and retained high hardness at elevated temperature significant increased the tool life by factors of 2 and 10, compared with conventional CVD and PVD coatings, respectively (Fig. 6.6). This study reveals that the Al-rich c- $Al_xTi_{1-x}N$ ($x \approx 0.8$) comprising

self-organised c-Al(Ti)N/c-Ti(Al)N nanolamellae microstructure can be used for practical dry and high-cutting-speed machining.

6.5. Summary

The findings of this study are summarised as follows:

1. c-$Al_xTi_{1-x}N$ ($x \approx 0.8$) coatings prepared via LP-CVD comprising a self-organised nanolamellar structure displayed higher thermal stability than monolithic c-$Al_xTi_{1-x}N$ ($x = 0.6$) coating prepared via PVD.

2. The significant increase of hardness at elevated temperature for c-$Al_xTi_{1-x}N$ ($x \approx 0.8$) coating compared to that with $x \approx 0.6$ is attributed to not only the spinodal hardening but also increased micro-strain during nanolamellar decomposition.

3. The c-$Al_xTi_{1-x}N$ ($x \approx 0.8$) coating with high thermal stability and hardness at elevated temperatures demonstrated a significant improvement in tool life by factors of 2 and 10, in comparison with conventional CVD- and PVD-coated inserts, respectively. The mass production of this new coating and development of related applications are currently underway.

References in chapter 6

[1] O. Knotek, T. Leyendecker, J. Solid State Chem. 70 (1987) 318–322.

[2] W. D. Münz, J. Vac. Sci. Technol., A 4 (1986) 2717–2725.

[3] P. H. Mayrhofer, A. Hörling, L. Karlsson, J. Sjölén, T. Larsson, Appl. Phys. Lett. 83 (2003) 2049–2051.

[4] I. Tsutomu, S. Hiroshi, Thin Solid Films 195 (1991) 99–110.

[5] J. Vetter, Surf. Coat. Technol. 76 (1995) 719–724.

[6] K. Macák, V. Kouznetsov, J. Schneider, U. Helmersson, I. Petrov, J. Vac. Sci. Technol., A 18 (2000) 1533–1537.

[7] A. Hörling, L. Hultman, M. Odén, J. Sjölén, L. Karlsson, J. Vac. Sci. Technol., A 20 (2002) 1815–1823.

[8] A. Hörling, L. Hultman, M. Odén, J. Sjölén, L. Karlsson, Surf. Coat. Technol. 191 (2005) 384–392.

[9] A. Paseuth, K. Yamagata, A. Miura, M. Higuchi, K. Tadanaga, J. Am. Ceram. Soc. 100 (2017) 343–353.

[10] A. Paseuth, K. Yamagata, A. Miura, K. Tadanaga, Proc. 19th Plansee Seminar, May 29-June 2, Reutte, Austria, (2017) p. HM49.

[11] R. M'Saoubi, S. Ruppi, CIRP Ann. Manuf. Technol. 58 (2009) 57–60.

[12] K. D. Bouzakis, E. Bouzakis, S. Kombogiannis, S. Makrimallakis, G. Skordaris, CIRP J. Manuf. Sci. Technol. 7 (2014) 264–73.

[13] W. Grzesik, Int. J. Mach. Tools Manuf. 39 (1999) 355–369.

[14] A. Paseuth, H. Fukui, S. Okuno, H. Kanaoka, Y. Okada, Surf. Coat. Technol. 260 (2014) 139–147.

[15] W. C. Oliver and G. M. Pharr, J. Mater. Res. 19 (2004) 3–20.

[16] J. W. Cahn, Acta Metall. 10 (1962)179–183.

[17] T. Miyazaki, Materia Japan. 53 (2014) 363–369.

[18] M. Setoyama, M. Irie, H. Ohara, M. Tsujioka, Y. Takeda, Thin Solid Films 341 (1999) 126–131.

[19] A. Knutsson, M. P. Johansson, L. Karlsson, M. Odén, J. Appl. Phys. 108 (2010) 044312.

[20] R. Rachbauer, S. Massl, E. Stergar, D. Holec, D. Kiener, J. Appl. Phys. 110 (2011)

023515.

[21] L. Rogström, J. Ullbrand, J. Almer, L. Hultman, B. Jansson, Thin Solid Films 520 (2012) 5542–5549.

[22] J. Todt, J. Zalesak, R. Daniel, R. Pitonak, A. Köpf, Surf. Coat. Technol. 291 (2016) 89–93.

[23] J. Wheeler and J. Michler, Rev. Sci. Instrum. 84 (2013) 101301.

Chapter 7. Conclusion and Future Outlook

7.1. Conclusion

The aim of this dissertation was to develop new ceramic hard coatings to enhance the performance of cemented carbide tools, so as to meet the demands for lower cost, lower environmental impact and resource conservation in industry. In order to achieve this goal, novel ceramic hard coatings, including TiC_xN_{1-x} and $Al_xTi_{1-x}N$ films, have been synthesised via a moderated and low-pressure CVD process. The results are summarized as follows.

In chapter 2, the MT-TiC_xN_{1-x} coatings with different x values were deposited using a $TiCl_4$–CH_3CN–C_2H_4–H_2 precursor system which allowed for an increase in the x value at 840°C by varying the C_2H_4/CH_3CN molar ratio. The effect of the x value on microstructure, crystallite size, indentation hardness, and adhesion of the MT-TiC_xN_{1-x} coatings were investigated. An increase in x resulted in an increase in hardness due to a decrease in crystallite size. The maximum hardness was 28.6 GPa for x values ranging from 0.66 to 0.69, which coincides with the minimum crystallite size of 39 nm. Contrarily, the adhesion of the TiC_xN_{1-x} coatings to carbide substrates decreased as the x value increased because of a change in the morphology and the formation of a discontinuous bonding interphase.

In chapter 3, the attempts to suppress the decrease in adhesion of TiC_xN_{1-x} coatings caused by differences in the chemical composition of the bonding layer and C-rich TiC_xN_{1-x} coatings which resulted in the formation of a discontinuous bonding interphase, led to the optimised x (x=0.63) value in the MT-TiC_xN_{1-x} coating. Considerable improvements in grain structure, micro-orientation, mechanical properties, and friction coefficients of modified MT-TiC_xN_{1-x} (x=0.63) coatings were obtained in comparison with those of a conventional MT-TiC_xN_{1-x} (x=0.45) coating. Moreover, the cutting performance obtained by longitudinal continuous turning of carbon, alloyed, and stainless steels and by intermittent turning tests with four-groove alloyed steel on as-deposited modified MT-TiC_xN_{1-x} (x=0.63) resulted in a significant increase in tool life, as high as 30%–60%, compared with the state-of-the-art MT-TiC_xN_{1-x} (x=0.45) coating; this is considered to be due to the increase in hardness and decrease in the friction coefficient between the coating and work materials. The modified MT-TiC_xN_{1-x} coating prepared via moderate temperature low-pressure chemical vapour

deposition using a $TiCl_4$–CH_3CN–C_2H_4–H_2 precursor system, has been applied in the tool industry, leading to a considerable increase in the service life of cemented carbide inserts in steels, cast irons, and stainless steels in turning applications. Based on this modified MT-TiC_xN_{1-x} coating, commercially available cemented carbide products, such as 'AC400K/AC4000K' [1-4] and 'AC6000M' [3,4], have entered the cutting tools market; the former material has a tendency towards high-speed cast iron turning, while the latter has a propensity for high performance hard-to-cut-materials cutting applications.

Because there is a constant demand for higher speeds and dry cutting, it is necessary to develop progressively advanced hard coatings with higher hardness and oxidation resistance. In chapter 4, synthesis of Al-rich cubic (c-) AlTiN coatings via low-pressure chemical vapour deposition (LP-CVD) in an industrial plant, using an $AlCl_3$–$TiCl_4$–NH_3–Ar–H_2 precursor system, was conducted in order to develop a higher performance hard coating and promote higher cutting speeds and dry cutting in milling applications. The c-$Al_xTi_{1-x}N$ coatings with (100) and (111) preferred orientations and average *x* values of 0.82 and 0.73, respectively, were deposited. These Al-rich c-$Al_xTi_{1-x}N$ coatings were comprised of c-Al(Ti)N/c-Ti(Al)N nano-lamellae with average lamellar periods of ca. 4.5–7.7 nm in an as-deposited state, and indicated that Al content fluctuates along the <100> direction. The unique and self-organised nano-structures were considered to occur via spinodal decomposition which decreases the free energy of formation of the system, leading to higher phase stability at elevated temperatures.

In chapter 5, the phase stabilities and mechanical properties of Al-rich c-$Al_xTi_{1-x}N$ coatings were investigated by comparison with a state-of-the-art arc PVD c-$Al_{0.6}Ti_{0.4}N$ coating, using annealing. The results demonstrated not only good thermal stability, but also superior hardness properties at elevated temperatures. The temperature of age hardening was shifted up by 100°C for the CVD c-$Al_xTi_{1-x}N$ (x=0.7, 0.8) coatings compared with the PVD c-$Al_{0.6}Ti_{0.4}N$.

In chapter 6, the effect of annealing temperatures and times on phase stability, microstructural evolutions and mechanical properties of CVD c-$Al_xTi_{1-x}N$ (x≈0.8) compared with PVD c-$Al_xTi_{1-x}N$ (x≈0.6) coatings were further investigated. A temperature of 1200°C for 1 h was necessary to eradicate the metastable c-AlN hard phase in c-$Al_xTi_{1-x}N$ (x=0.8), which

is approximately 200°C higher than that of the c-$Al_xTi_{1-x}N$ (x=0.6) coating. These considerable improvements in the thermal stability and mechanical properties of the Al-rich c-$Al_xTi_{1-x}N$ coating resulted in a significant increase in the cutting tool life, by factors of 2 and 10 compared with state-of-the-art CVD-TiCN/Al_2O_3 and PVD-AlTiCrN coated inserts, respectively, in cast iron milling operations. This novel Al-rich c-$Al_xTi_{1-x}N$ coating comprised of c-Al(Ti)N/c-Ti(Al)N nano-lamellae prepared via LP-CVD using an $AlCl_3$–$TiCl_4$–NH_3–Ar–H_2 precursor system [5] assures further enhancement in the cutting tool performance for dry and high-speed cutting applications.

7.2. Future outlook

It is constantly necessary to increase cutting speeds in the metal working industry to achieve higher productivity and lower production costs. The development of increasingly advanced hard coatings with super hardness, good thermal stability and high oxidation resistance are a necessity to realise the requirements of industry. In this dissertation, the wear resistance of an MT-TiCN/Al_2O_3 coating was suppressed by applying a c-rich TiC_xN_{1-x} (x=0.63) coating, which could be deposited by doping with C_2H_4 gas into a $TiCl_4$–CH_3CN–H_2 precursor system. Furthermore, the increase in elevated hardness and thermal stability, which is beneficial for high speed and dry cutting, was achieved by applying an Al-rich c-$Al_xTi_{1-x}N$ coating prepared by an $AlCl_3$–$TiCl_4$–NH_3–Ar–H_2 precursor system. The next development in this research will involve the deposition of Al-rich c-$Al_xTi_{1-x}N_yC_{1-y}$ coatings via LP-CVD using an $AlCl_3$–$TiCl_4$–NH_3–C_2H_4–Ar–H_2 [6] precursor system. Moreover, combining a c-$Al_xTi_{1-x}N$ coating with an Al_2O_3 over-layer is expected for further improvements in cutting performance. However, an Al_2O_3 coating via CVD is commonly conducted at a temperature of 1000°C to achieve good crystallinity and to be economical. This high temperature could trigger the phase transformation from c-$Al_xTi_{1-x}N$ to h-AlN and c-TiN phases which could deteriorate the mechanical properties during the CVD process. Thus, development of a lower temperature Al_2O_3 coating via the CVD process is an attractive future challenge.

References in Chapter 7

[1] S. OkunO, A. Paseuth, Y. Okada, A. Sakamoto, SEI. Tech. Rev.. 75 (2012) 8–12.

[2] S. OkunO, H. Kanaoka, S. Ono, S. Imamura, K. Hirose, H. Fukui, SEI. Tech. Rev. 191 (2017) 43–46.

[3] H, Takeshita, Y. Koyoshi, N. Matsuda, S. Okuno, K. Hirose, H. Fukui, SEI. Tech. Rev. 186 (2015) 85–91.

[4] H. Fukui, SEI. Tech. Rev. 82 (2016) 39–45.

[5] A. Paseuth, K. Yamagata, A. Miura, M. Higuchi, K. Tadanaga, J. Am. Ceram. Soc. 100 (2016) 343−353.

[6] I. Endler, M. Höhn, M. Herrmann, H. Holzschuh, R. Pitonak, S. Ruppi, H. van den Berg, H. Westphal, L. Wilde, Surf. Coat. Technol. 205 (2010) 1307−1312.

Acknowledgements

I would like to express my sincerest gratitude to Prof. Kiyoharu TADANAGA for his excellent support and guidance. His guidance helped me in all the time of research and writing of this thesis. I could not have imagined having a better advisor and mentor for my Ph.D. study.

Besides my advisor, I would like to thank the rest of my thesis committee: Prof. Toshihiro SHIMADA, Prof. Yukio HINATSU, and Assoc. prof. Mikio HIGUCHI, for their insightful comments and encouragement, but also for the hard question which incented me to widen my research from various perspectives.

My thanks also go to Dr. Akira MIURA, who provided me suggestions and countless discussions. Thanks to you, I was able to create fun memories.

I would like to express my sincere thanks to Emeritus Professor Shiro Shimada (Hokkaido University, Japan) for his encourages and proofreading my manuscripts. Thanks to you I learned how hard and sweet to publish a scientific paper.

I would like to thank Mr. Yoshikatsu MORI, Mr. Masuo CHUUDO and Mr. Kazuo YAMAGATA from Sumitomo Electric Hardmetal Corp. for their encourages and permission to carry out my thesis

I am deeply grateful to my mother in LAOS for her love and support.

Last but not least, I want to thank my family for their kind support. The most important person in my life, my wife “Yumiko”, and my lovely kids “Yuki, Daiki and Haruki”, who always encouraged and supported me.

Anongsack PASEUTH

Hokkaido, September 2018